AEDC-TR-70-291

FREE-FLIGHT MEASUREMENTS OF SPHERE DRAG AT SUBSONIC, TRANSONIC, SUPERSONIC, AND HYPERSONIC SPEEDS FOR CONTINUUM, TRANSITION, AND NEAR-FREE-MOLECULAR FLOW CONDITIONS

A. B. Bailey and J. Hiatt

ARO, Inc.

March 1971

1 5 1980

VON KÁRMÁN GAS DYNAMICS FACILITY
ARNOLD ENGINEERING DEVELOPMENT CENTER
AIR FORCE SYSTEMS COMMAND
ARNOLD AIR FORCE STATION, TENNESSEE

NOTICES

FREE-FLIGHT MEASUREMENTS OF SPHERE DRAG AT SUBSONIC, TRANSONIC, SUPERSONIC, AND HYPERSONIC SPEEDS FOR CONTINUUM, TRANSITION, AND NEAR-FREE-MOLECULAR FLOW CONDITIONS

A. B. Bailey and J. Hiatt

ARO, Inc.

FOREWORD

The work reported herein was sponsored by the Air Force Cambridge Research Laboratories (AFCRL), Office of Aerospace Research (OAR), Laurence G. Hanscom Field, Bedford, Massachusetts, under Program Element 65701F, Project 6682.

The results of tests presented were obtained by ARO, Inc. (a subsidiary of Sverdrup & Parcel and Associates, Inc.), contract operator of the Arnold Engineering Development Center (AEDC), Air Force Systems Command (AFSC), Arnold Air Force Station, Tennessee, under Contract F40600-71-C-0002. The tests were conducted from November 13, 1969, through June 19, 1970, under ARO Project No. VK0030, and the manuscript was submitted for publication on October 5, 1970.

This technical report has been reviewed and is approved.

Emmett A. Niblack, Jr.   Joseph R. Henry
Lt Colonel, USAF   Colonel, USAF
AF Representative, VKF   Director of Test
Directorate of Test

ABSTRACT

A comprehensive set of measurements has been made in a ballistic range which permits the sphere drag coefficient to be derived with an uncertainty of approximately ±2 percent in the flight regime $0.1 < M_\infty < 6.0$ and $2 \times 10^1 < Re_\infty < 10^5$ for $T_W/T_\infty \approx 1.0$. Sufficient information is also presented to predict the effect of wall temperature on sphere drag coefficient when $T_W/T_\infty \neq 1.0$ for $2 < M_\infty < 6$. This investigation represents the most comprehensive experimental program to date to define sphere drag in the velocity-altitude regime applicable to the falling sphere technique for defining upper air density.

CONTENTS

APPENDIXES

I. ILLUSTRATIONS

Figure

NOMENCLATURE

A	Frontal area of sphere, $\pi d^2/4$
a	Speed of sound
C_D	Drag coefficient
C_{DF}	Friction drag coefficient
C_{DPB}	Afterbody pressure drag coefficient
C_{DPF}	Forebody pressure drag coefficient
C_{DFM}	Free-molecular drag coefficient
D	Drag force
d	Diameter of sphere, $(d_{max} + d_{min})/2$
M	Mach number, V/a
m	Mass of sphere
p	Pressure
P_0'	Impact pressure
$P_0'{}_{inviscid}$	Ideal, inviscid impact pressure
R	Gas constant
Re	Reynolds number, $\rho V d/\mu$
T	Temperature
t	Time
V	Velocity
ΔV	Velocity drop (for 75 ft of flight between shadowgraph stations 1 and 6
x	Distance
ρ	Density
μ	Viscosity

SUBSCRIPTS

2	Conditions immediately downstream of normal shock wave
w	Sphere surface
∞	Free-stream conditions
i, j	Shadowgraph station interval, i = 1 to 6, j = 2 to 6

vii

SECTION I
INTRODUCTION

Falling, spherically shaped, pressurized balloons are extensively used for atmospheric probing (Ref. 1). These probes can be used to determine several properties of the upper atmosphere (horizontal winds, density, temperature, and pressure), the most important property being atmospheric density. The velocity of descent of a sphere of specified size and weight at a particular altitude is a function of the density of the atmosphere at that altitude and the drag coefficient of the sphere at those conditions. Density is inversely proportional to the balloon drag coefficient and can be inferred if that drag coefficient is known.

For several years the Air Force Cambridge Research Laboratory has conducted falling sphere atmospheric soundings between the altitudes of 140 and 30 km. Two different kinds of balloons have been used, and the motion of each is measured by a different method. One probe is a 1-m-diam Mylar® passive sphere, ROBIN, whose space-time positions during its fall are measured with precision ground-based radar. The second balloon is an "Instrumented Sphere" whose falling motion is measured by on-board accelerometers. These two balloons have different fall rates and trajectories. Figure 1 (Appendix I) is a Mach number-Reynolds number envelope of typical trajectories of the two types of balloons.

The need for further sphere drag measurements arose from two sources, namely:

1. The results of previous sphere drag tests, by many experimenters and using a variety of test facilities, are not always in agreement.

2. Falling spheres experience some M_∞-Re_∞ values for which drag coefficients are not available.

It is for the reasons stated above that the present sphere drag study was undertaken. The investigation has been conducted in the M_∞-Re_∞ range defined in Fig. 1 according to the AFCRL specified priorities.

The present sphere drag investigation was undertaken in the von Kármán Gas Dynamics Facility (VKF) of AEDC. In an aeroballistic range, sphere drag coefficient was measured for a broad range of Mach number ($0.12 < M_\infty < 6.39$) and Reynolds number ($15 < Re_\infty < 50,300$).

SECTION II
AEROBALLISTIC RANGE

The aeroballistic range testing was conducted in the Hyperballistic Range (K). This range is a variable density, free-flight test unit that is used for aerophysical testing and for classical aerodynamic tests, notably the measurement of drag. The aeroballistic range consists basically of two tanks, a pumping system, a launcher, and several instrumentation systems.

2.1 RANGE K

The range tank and blast tank are 6-ft-diam steel cylinders connected by a short spool piece containing a high vacuum valve which permits isolation of the two tanks (see Fig. 2). The 14-ft-long blast tank is situated between the launcher and the range tank. The blast tank is used to absorb the expanding muzzle gases, and it is in this chamber that the model is separated from the sabot which adapts it to the bore of the launcher. Once separated from the sabot, which is stopped in the blast tank, the model flies through a 3-in.-diam hole in the spool piece and into the range tank.

The range tank is 100 ft long and is equipped with the instrumentation necessary to make the desired test measurements. Shadowgraph, schlieren, temperature, and pressure instrumentation systems are permanently installed. Flight is terminated by model impact on a thick plate at the end of the range tank.

A three-stage vacuum pumping system provides the desired range pressure. The blast and range tanks have independent pumping systems which facilitate testing at low pressures because the range tank can be kept isolated at low pressure while the launcher is being prepared for the next shot. For this test, all shots were fired with the blast and range tank pressures equal.

Three different launchers were employed in achieving the desired range of velocities, $0.2 \leq M_\infty \leq 6.0$:

1. Cold-Gas Gun - Most of the spheres for which $M_\infty < 1.7$ were launched with a single-stage, cold-gas pneumatic launcher using helium as the driving gas. This launcher is essentially the same as that used by Lawrence (Ref. 2) in an earlier VKF sphere drag test.

2. 20-mm Cannon - The majority of the spheres for which $M_\infty > 1.7$ were launched with a 20-mm-diam, smooth-bore, single-stage launcher. Burning gunpowder supplied the driving pressure.

3. Rifle - A few shots were made with a 30-cal, rifled-bore, single-stage, powder-driven launcher.

Launchers 1 and 2 were used for 92 percent of the shots.

2.2 RANGE INSTRUMENTATION

Six dual-axis spark shadowgraph stations record the model position-time history for each flight. These stations are located at nominally 15-ft intervals along the range tank. Optical axes at each station are mutually orthogonal with the range centerline. The shadowgraph consists of a pinhole spark source on one side of the range and a Fresnel lens and camera on the other side. Except for the Fresnel lens, the shadowgraph system components are external to the range tank. The spark has a duration of 0.1 μsec; therefore, this is the effective exposure time of the shadowgram. A shadow detector is used to trigger the spark when the model is near the center of the shadowgraph field of view. When the spark is initiated, a signal is sent to a multichannel digital event chronograph which records the times of successive shadowgram exposure. The Fresnel lenses bear scribed fiducial grids, and the stations have been surveyed accurately as to orthogonality and spacing so that model position can be determined in real space with respect to master range axes. This survey has been further refined by calibration shots with spheres of high density material fired into a hard vacuum ($\Delta V \approx 0$) at velocities which minimize time-position uncertainties.

Gas temperatures in the range tank are measured by means of mercury-in-glass thermometers and by copper-constantan thermo-couples read out on a strip-chart recorder. A pair of these probes is located near each of the six shadowgraph stations.

In order to ensure that the air in the range is sufficiently dry, dew-point temperature is measured with a hygrometer located near the center of the range tank. Dry air can be supplied by the VKF high pressure bottle ($H_2O < 100$ ppm) or from a source of pure breathing air ($H_2O < 30$ ppm).

A high sensitivity, single-pass schlieren photographic system is available for visualizing the model flow field. The viewfield diameter is 12 in., and the system is operable in either single-frame or multiple-frame modes.

All gages used to measure pressure in the range are connected to a large stainless steel manifold which can be isolated from the range tank and kept under hard vacuum when not in use. As many as six gages can be connected to the manifold. For this test three types of gages were used:

1. Hass Mercury Manometer - This instrument is used over the pressure range from 15 to 760 torr. It has a resolution of 0.05 torr.

2. Micromanometer - This is an oil-filled, U-tube manometer with which VKF has considerable experience. It is used for measuring pressures between 0.1 and 15 torr. Resolution of the micromanometer is 0.00075 torr.

3. Baratron® - This is a variable-capacitance pressure transducer which has a small internal volume. The volume of the other two instruments is large and they, therefore, do not respond as rapidly as the Baratron to a changing pressure. The Baratron has two sensing heads: 1 torr and 30 torr. This permits the measurement of pressures from 30 torr down to approximately 10^{-4} torr. Baratron resolution is 1×10^{-4} torr for pressures above 10 torr and is 1×10^{-5} torr for pressures below 10 torr.

Insofar as possible, these pressure gages are calibrated with standards traceable to the National Bureau of Standards (NBS). In pressure regions where no NBS standard exists ($p < 1$ torr), calibration is accomplished by reasonable extension of existing standards and by means of a VKF-built calibrator described in Ref. 3. Since Ref. 3 was written, a new calibrator has been built to closer tolerances, and greater precision is now possible. The calibrator itself has been thoroughly checked against the NBS standards where possible. Calibration of all the gages was performed before, during, and after this test in order to ensure the greatest possible accuracy in the pressure measurement.

2.3 MODELS AND SABOTS

The variety of sphere materials and sizes used in the range test are listed in Table I (Appendix II) and illustrated in Fig. 3. Whenever possible, spheres of a conventional material were used. Commercially available, precision grade, standard spheres were chosen in order to ensure high quality surface finish and to minimize nonsphericity. The spheres were then individually inspected and measured at AEDC. The variety of spheres used was necessary in order to produce the desired

Reynolds number and Mach number at a velocity drop, ΔV, of between 1 and 6 percent of the average velocity, V.

The minimum model size of 3/32-in. diameter was the smallest that could be reliably detected by the present shadowgraph triggers. This size limitation, along with the desire to maintain ΔV between 1 and 6 percent, establishes the minimum Reynolds number at which tests can be conducted with conventional model materials. Models of molded Dylite® were used to overcome this limitation. Dylite is a foamed plastic that was used by VKF in the manufacturing of spheres whose density ranged from 1 to 6 lb/ft^3. References 4 and 5 discuss the original use of Dylite in the manufacturing of lightweight models and the measurement of C_D with these models. The use of these lightweight foam models allowed testing at lower Re_∞ while maintaining the desired model deceleration. The lower Re_∞ limitation for Dylite models was not reached in this test.

Several sabot designs were used during the course of this test. Typical examples are shown in Fig. 3. Except for a few Dylite and partially Dylite sabots, all were made of Lexan®. A different method of separating the sphere from the sabot was employed with each of the three launchers. Figure 4 illustrates these stripping methods.

SECTION III
RANGE SPHERE DRAG MEASUREMENT

3.1 THEORY

The equation of motion of a sphere in free flight is simply Newton's Law written as follows:

$$D = ma = 1/2 \rho\, V^2 C_D A \tag{1}$$

Using the relationships $p = \rho R T$ and $A = \pi/4\, d^2$ and substituting in Eq. (1), it can now be written

$$m\, \frac{dV}{dt} = \frac{\pi\, p\, V^2 C_D\, d^2}{8\, R\, T} \tag{2}$$

or, solving for C_D

$$C_D = \frac{8m\, R\, T}{\pi\, p\, d^2\, V^2} (dV/dt) \tag{3}$$

Making the substitution

$$1/V\, (dV/dt) = dt/dx \cdot dV/dt = dV/dx$$

5

Eq. (3) takes the form

$$C_D = \frac{8m\,R\,T}{\pi\,p\,d^2\,V}\,(dV/dx) \qquad (4)$$

It is shown that drag coefficient can be obtained if the sphere mass, diameter, velocity, and deceleration and the range temperature and pressure are known. These quantities can all be measured in a range experiment.

3.2 METHOD

Before launching, the sphere is cleaned, inspected, weighed, and measured to determine its surface finish quality, mass, and diameter. The sphere is then launched into dry air at a known pressure and temperature. Position-time measurements are obtained during the flight of the sphere, and then velocity and deceleration are derived from these data. The sphere mass, diameter, and material and the range pressure are varied in order to produce the desired Reynolds number at a given velocity and to keep the velocity drop between 1 and 6 percent.

3.3 DATA REDUCTION

The sphere image on the shadowgrams is read with a digitized film reader, and the resultant numerical values are converted, by means of a computer program containing the range shadowgraph system survey, into real space positions. These model positions and the associated timing values are used to calculate the average velocity between all pairs of adjacent shadowgraphs ($V_{i,\,i+1}$ for i = 1 to 5). In addition, average velocities over a two-station interval ($V_{i,\,i+2}$ for i = 1 to 4) are calculated. This second set of velocities has only half of the uncertainty in x and t, compared to the first set, since the total distance and time are doubled.

A least-squares straight line is computer fitted to the velocity-position data. Figure 5 is a typical example of this fitting. By fitting a straight line to these data, the assumption is made that C_D is a constant during the flight. This assumption is quite valid for this test since the model velocity drop, ΔV, was less than 6 percent of the midrange velocity. The value of V used in the computation of Re_∞ and C_D and the value of dV/dx used in the computation of C_D are taken from the fitted line. In this data reduction, Eq. (4) is used to calculate C_D.

Another data reduction method is also used on the position-time data. The time-position relationship of a model in free flight can be represented by a cubic equation in distance, viz

$$t = a_0 + a_1 x + a_2' x^2 + a_3 x^3$$

This equation is computer fitted to the time-position data by the method of least squares. In this case the deceleration is not assumed constant. If the model undergoes a large percentage velocity drop, this treatment of data is required. Reynolds number and C_D are computed from values of V and dV/dt taken from the fitted cubic. In this treatment, C_D is calculated from Eq. (3).

Although the cubic fit was not necessary for the treatment of position-time data on this test since $0.01 \leq \Delta V/V \leq 0.06$, both linear fit derived and cubic fit derived values of M_∞, Re_∞, and C_D were computed for all shots. To verify the contention that the linear fit is adequate if $\Delta V/V < 0.06$, differences in linear and cubic fit derived values of M_∞, Re_∞, and C_D were obtained for seven shots where $0.058 < \Delta V/V < 0.073$. These shots were picked because these differences will increase with increasing $\Delta V/V$. For all seven shots, the differences in M_∞ and Re_∞ were less than 0.01 percent and for C_D were less than 0.1 percent.

3.4 MEASUREMENTS AND UNCERTAINTY

3.4.1 Distance

As explained in Section 4.3, downrange position is determined from the shadowgrams. The results of past Range K shadowgraph station surveys and calibration shots in conjunction with check calibration shots fired during the course of this test show that the maximum error in model position (flight distance) is less than ±0.0025 in. The flight distance between adjacent shadowgraph stations is nominally 15 ft.

3.4.2 Time

The digital event chronograph associated with the shadowgraph system provides timing values with a resolution of 1×10^{-7} sec. The maximum error in the time of flight between adjacent shadowgraphs is $\pm 1 \times 10^{-7}$ sec ($\pm 0.1 \, \mu$sec). For this test, interstation flight time varied between $1.1 \times 10^5 \, \mu$sec ($M_\infty = 0.12$) and $2.1 \times 10^4 \, \mu$sec ($M_\infty = 6.39$). The timing error is not cumulative. The maximum error in the total time of flight is also $\pm 0.1 \, \mu$sec.

7

3.4.3 Velocity

The velocity used in the computation of C_D and Re_∞ is the midrange velocity as derived from the linear fit to the $V_{i,j}$ and x data. The maximum error in $V_{i,i+1}$ is 0.03 percent. On this test, shots were rejected if the maximum $[(V_{i,i+1}$ computed from x, t data) - $(V_{i,i+1}$ from curve fit)$]$ was more than 0.025 percent of the midrange velocity. This maximum velocity error was less than <0.02 percent on 95 percent of the shots. The midrange velocity, used in calculating C_D and Re_∞, is known to an uncertainty of less than 0.02 percent, since it is obtained from a curve fit to all the velocity-position data. The velocity range on this test was from 136 to 7250 ft/sec.

3.4.4 Deceleration

Deceleration is one of the least accurately known quantities. Whereas small perturbations around the true values of x and t produce very small changes in velocity, such perturbations can produce a relatively large change in dV/dx. An analysis of x, t, and dV/dx errors indicates that for the wide range of shots made during this test, the maximum possible uncertainty in deceleration can be greater than 1 percent. However, the x, t, and V accuracy on the majority of the shots is such that the uncertainty in dV/dx should not exceed 1 percent.

3.4.5 Mass

Sphere mass was determined on either of two analytical balances or on a torsion balance. The choice was dependent upon sphere mass. Great care was taken in the handling of the spheres, and they were weighed after they had been cleaned and their diameters measured. Balance zero was checked before each weighing, and each sphere was weighed several times. For spheres of m < 0.021 gm (those weighed on the torsion balance), a class M standard weight of approximately equal mass was weighed before and after each sphere weighing. Uncertainties in the measurement of sphere mass are as follows:

$$0.00023 \text{ gm for } m > 0.5 \text{ gm}$$
$$0.00016 \text{ gm for } 0.14 < m < 0.5 \text{ gm}$$
$$0.00005 \text{ gm for } 0.05 < m < 0.14 \text{ gm}$$
$$0.00002 \text{ gm for } 0.015 < m < 0.05 \text{ gm}$$
$$0.00001 \text{ gm for } m < 0.015 \text{ gm}$$

3.4.6 Diameter

Two instruments were employed in the measurement of sphere diameter. Spheres of conventional materials were measured with a

8

light wave micrometer which has an accuracy of ±0.00001 in. Since this instrument applies mechanical pressure to the sphere during measurement, this technique is not suitable for the foam spheres. These were measured with a microscope which has an accuracy of ±0.0001 in. Several measurements were made on each sphere in order to determine the maximum and the minimum diameters. The diameter used in the calculation of C_D and Re_∞ was the average of these two diameters. Spheres of conventional materials were selected such that the uncertainty in diameter attributable to nonsphericity was always less than 0.1 percent of the diameter. For the foam spheres, the uncertainty in diameter attributable to nonsphericity was 0.5 percent for $d \approx 0.25$ in. and 1.0 percent for $d \approx 0.125$ in.

3.4.7 Temperature

Range temperature, at any probe location, is most accurately determined by the mercury-in-glass thermometer which has a maximum error of ±0.1°F. The thermocouple temperatures have an accuracy of ±0.5°F and were used as a check on the thermometer temperature readings in order to determine that there were no transients at the time of the shot. Even without noticeable transients at any probe location, there usually exists a slight gradient in temperature along the length of the range. The temperature at any probe location never differed from the average of the six temperature measurements by more than ±2°F. This maximum variation yields an uncertainty of no greater than 0.38 percent in absolute temperature. Average range temperature on this test varied between extremes of 63.2 and 83.8°F, but was normally between 73 and 79°F.

3.4.8 Pressure

The pressure variation of this test was from 538 to 0.034 torr. This required the use of all three types of gages listed in Section 2.2. The use of each gage was limited to that pressure range over which it had the greatest accuracy. Where pressure ranges for more than one gage overlapped, each was read. The difference in pressure between gages was no greater than 1.0 percent even at the end of a particular gage's range. This does not necessarily imply a pressure uncertainty of 1.0 percent since the pressure reading of the gage not at the extreme of its pressure range would be the more accurate. The maximum uncertainty in pressure is no greater than 1 percent for $p \geq 1$ torr. For pressures below 1 torr, the uncertainty increases with decreasing pressure and reaches a maximum no greater than 2 percent at $p = 0.034$ torr.

3.4.9 Drag Coefficient

The uncertainties specified above are maximum possible uncertainties. Maximum probable uncertainties would be less than or equal to these values. The maximum probable uncertainty in drag coefficient attributable to uncertainties in the measurements are as follows:

V	0. 02 percent
T	0. 28 percent
dV/dx	1. 0 percent
m	0. 1 to 0. 3 percent (conventional materials)
	0. 5 percent (1/4-in. -diam Dylite)
	1. 0 percent (1/8-in. -diam Dylite)
d	0. 2 to 0. 3 percent (conventional materials)
	1. 0 percent (1/4-in. -diam Dylite)
	2. 0 percent (1/8-in. -diam Dylite)
p_∞	0. 5 percent (p_∞ > 1 torr)
	1. 0 percent (0. 1 < p_∞ < 1 torr)
	2. 0 percent (p_∞ < 0. 1 torr)

As can be seen from the data in Figs. 11a through h and 11l through v, the scatter around the fitted curve is such that C_D is certainly determined to within ±2 percent for $Re_\infty \geq 200$. Below Re_∞ = 200, the scatter increases because of increasing pressure uncertainty for all conditions, but the scatter becomes noticeably worse only when Dylite models are used. In spite of the increased data scatter, the greater number of shots fired at these conditions and the method of data treatment (Section 5. 1) results in values of C_D that are probably correct within ±2 percent even down to Re_∞ = 20.

3.4.10 Reynolds Number

The accuracy of Re_∞ is dependent upon the uncertainties in p_∞, T_∞, V, and d. The maximum probable uncertainties in Re_∞ are as follows:

0. 8 percent for $Re_\infty \geq 200$
1. 2 percent for Re_∞ < 200

3.4.11 Mach Number

As M_∞ depends only upon V and T, the maximum probable uncertainty is 0. 2 percent.

SECTION IV
DISCUSSION OF EXPERIMENTAL RESULTS

4.1 AEROBALLISTIC RANGE DATA

The results of the present test program for $0.1 < M_\infty < 6.0$ and $2 \times 10^1 < Re_\infty < 10^5$ are listed in Table II and are presented in Figs. 6a through v as the variation of drag coefficient with free-stream Reynolds numbers for discrete Mach number intervals. Also shown in these figures are the results of sphere drag measurements presented in Refs. 2, 5, and 6 through 12. No attempt has been made to ensure that this listing of references is complete. These data were selected because the ratio of the model wall temperature to free-stream temperature was approximately unity, as is the case for the ballistic range data contained herein.

At subsonic speeds (Figs. 6a through j), the present data are in good agreement with those obtained by Lawrence (Ref. 2) in the same facility. The data contained in Refs. 6 and 7 for subsonic velocities are consistent with the data obtained in the present investigation (Figs. 6a through j). For supersonic velocities, the data available from a variety of sources (Refs. 5 and 6 through 11) are also consistent with those obtained in the present investigation (Figs. 6k through v).

Curves have been faired through all of the available data at the discrete Mach number intervals listed in Figs. 6a through v. An average Mach number has been assigned to each of these Mach number intervals (e. g., for interval $0.19 < M_\infty < 0.27$, $M_{\infty_{avg}} = 0.23$) and cross-plots of C_D versus Mach number have been derived at fixed Reynolds numbers (Figs. 7a through d). The symbols shown in Fig. 7 are not experimental points but are values derived from faired curves in Figs. 6a through v. It is from these crossplots that drag coefficients should be derived. An estimation of C_D at $M_\infty = 0$ is shown in Appendix IV.

It is evident from a consideration of the data contained in Figs. 6a through v that for $Re_\infty < 100$ the spread in the experimental values of C_D increases. In general, measurements in this regime were obtained with ultralight spheres and at ambient pressures less than $100\,\mu Hg$. Several factors contribute to this spread -- larger uncertainties in model weight and diameter, model distortion, and pressure.

From an examination of the measurement errors discussed in Section 4.4 and the consistency of the experimental data (Figs. 6a through v), indications are that the total errors in sphere drag coefficient derived from the faired curves are no greater than ±2 percent.

11

4.2 SPHERE DRAG COEFFICIENTS AT SUBSONIC SPEEDS

An accurate knowledge of the drag coefficient of a sphere at low subsonic speeds is of interest in the ROBIN Falling Sphere program. From a consideration of the possible falling sphere trajectories (Fig. 1), a knowledge of the sphere drag coefficients for $0.1 < M_\infty < 0.5$ and $10^3 < Re_\infty < 5 \times 10^4$ is required.

Before 1930, many measurements of the drag of a sphere falling through various fluids were made, and a body of information was generated for $10^{-1} < Re_\infty < 10^6$. It was considered that these data gave the level of the incompressible drag coefficient of a sphere in steady nonturbulent flow. Usually these data, which have a significant degree of scatter, are represented by a single line which is called the "standard drag curve." This curve has appeared in many textbooks and reports at least as far back as 1931 (Ref. 13). (No attempt is made here to determine its exact origin.)

The "standard drag curve" for the range of interest of the ROBIN Spheres is shown in Fig. 8. Also shown in this figure are two examples of the early data upon which this curve has been based (Refs. 14 and 15).

Heinrich, Niccum, and Haak (Ref. 16) made some sphere drag measurements in a wind tunnel for $0.078 < M_\infty < 0.39$ and $2 \times 10^3 < Re_\infty < 2 \times 10^4$. These data are compared with the standard drag curve in Fig. 8 and are shown to be significantly higher than the standard values. Sivier (Ref. 17) has measured the drag of magnetically supported spheres in a wind tunnel with a free-stream turbulence intensity up to 6 percent. These sphere drag values (cf. Fig. 8) are also significantly greater than the standard drag values. Zarin (Ref. 18) refined the magnetic balance system used by Sivier (Ref. 17) and varied the free-stream turbulent intensity level. He obtained some sphere drag measurements at free-stream turbulent intensity levels of less than 1 percent. These values are shown in Fig. 8. For $Re_\infty > 10^3$ these values are still significantly greater than the standard values. For $Re_\infty < 10^3$ these values are in good agreement with the standard values. From his study, Zarin concluded that small degrees of free-stream turbulence were the cause of his higher-than-standard drag values.

Also shown in Fig. 8 are the present drag values from Fig. 6b. It can be seen that these values are in reasonable agreement with the standard values for $5 \times 10^2 < Re_\infty < 10^4$. It is reasonable to assume that the ballistic range data are representative of a free-stream turbulent intensity level approaching zero. If the effects of turbulence shown by Zarin (Ref. 18) are correct, then it might be inferred that some

12

consideration of the scaling of free-stream turbulence intensity level may be necessary before sphere drag coefficients from turbulent test facilities can be applied to a particular falling sphere in the atmosphere. It is an experimentally demonstratable fact that turbulence can affect the critical Reynolds number where boundary-layer transition occurs. The critical Reynolds number is that Reynolds number for which the drag coefficient decreases sharply and passes through $C_D = 0.3$ as Re_∞ increases. Increasing degrees of turbulence have been shown to reduce the critical Reynolds number for $Re_\infty > 10^5$ (Refs. 19 and 20) and to increase C_D in the area $100 < Re_\infty < 1000$ (Ref. 18). Millikan and Klein (Ref. 19) found that the critical Reynolds number for a sphere in free flight in the atmosphere was not affected by varying atmospheric turbulence structure. This result was explained by the fact that the scale of the turbulence in the atmosphere is large compared with the boundary layer on the sphere. It would seem reasonable to assume that if the critical Reynolds number of a free-flight sphere is unaffected by the full-scale turbulence, then the drag coefficient at subcritical Reynolds numbers would also be unaffected by turbulence.

As a matter of interest, there appear to be inconsistencies in the literature as to the effect of free-stream turbulence upon drag coefficient. Zarin (Ref. 18) indicates that his and Sivier's (Ref. 17) greater than "standard values" for sphere drag can be explained in terms of turbulence, intensity, and scale. However, Probstein and Fassio (Ref. 21) explain Ingebo's (Ref. 22) lower than standard values of drag in terms of turbulence in the flow. Actually, depending on the particular Reynolds number regime, it would seem that turbulence could either raise or lower C_D.

4.3 EFFECTS OF COMPRESSIBILITY ON SPHERE DRAG COEFFICIENT

As in the case for the subsonic velocities, there is a generally accepted curve (Fig. 9) which has been used to indicate the effects of compressibility upon sphere drag coefficient. This curve appears to have originated with Hoerner (Ref. 23) and has been repeated in several references since (e. g., Refs. 1, 17, and 18). The form of the variation of sphere drag coefficient with Mach number (Ref. 23) was based upon several sets of data for $0 < M_\infty < 1.0$ obtained before 1946 (including, for example, the ballistic range data of Ref. 6). The curve is characterized by a pronounced dip in the drag coefficient at $M_\infty = 0.85$. Unfortunately, the ballistic range test (Ref. 6) did not obtain data for $0.65 < M_\infty < 0.85$. An inspection of the remaining data (Ref. 23) upon which this curve (Fig. 9) was based indicates that the curve fitted to the data may not, in fact, be the best fit to the data. This is confirmed to

13

some extent when Naumann's data (Ref. 7) is considered in Fig. 9. It can be seen (Fig. 9) that these data agree with Charters' and Thomas' data (Ref. 6) and do not show a dip in drag coefficient at $M_\infty \approx 0.85$.

The reason for presenting the above discussion is to examine the validity of the dip in light of the present results. If the form of Hoerner's curve is accepted, then to some extent his explanation for the reason for the dip is accepted (cf. Ref. 18). Hoerner's explanation for the dip is that it is attributable to "a favorable interaction between the local supersonic field of flow existing at and behind the location of the cylinder's (sphere's) maximum thickness and the flow pattern within its wake." If this reasoning is accepted, then for lower subcritical Reynolds numbers a curve with similar characteristics would be expected. None of the summary curves shown in Fig. 7 indicates that this occurs. To indicate that the effect has not been obscured by the smoothing procedure used in deriving the summary curves, the data obtained for $1930 < Re_\infty < 2080$ are shown in Fig. 10. These and Naumann's (Ref. 7) data are sufficiently well defined to state with some certainty that there is no dip in the C_D versus M_∞ curve for $M_\infty \approx 0.85$.

4.4 TRANSONIC SPHERE DRAG COEFFICIENTS

There appear to be very few experimental measurements of sphere drag in the transonic speed regime. The data contained in Figs. 6a through l and repeated in the summary curves in Figs. 7a through d represent the most comprehensive set of results in this speed regime. From a consideration of the data presented in Fig. 7 for $2 \times 10^1 < Re_\infty < 10^6$, it is apparent that the form of the C_D versus M_∞ variation at $0.9 < M_\infty < 1.1$ is a function of free-stream Reynolds number. For high Reynolds numbers (i. e., $Re_\infty > 10^5$), there appears to be a smooth transition from subsonic to supersonic drag values. For $2 \times 10^2 < Re_\infty < 10^4$, there is not a smooth transition from subsonic to supersonic drag values. For $2 \times 10^1 < Re_\infty < 2 \times 10^2$, the change from subsonic to supersonic drag values is accompanied by relatively large changes in C_D for small changes in M_∞.

The significance of these results is that they indicate a basic difficulty in measuring sphere drag at $M_\infty = 1.0$ in a short ballistic range such as the VKF 100-ft Range K. The reason for this is that a velocity drop of at least 10 ft/sec is required to derive an accurate drag coefficient at $M_\infty = 1.0$. This means that for $M_{\infty avg} = 1.0$ the Mach number varies from 0.996 to 1.004. At low Reynolds numbers in this speed regime, it is not completely valid to assume that C_D is constant, and the VKF 1000-ft range (Hyperballistic Range (G)) would be required in order to accurately detect the C_D change for a ΔV of only 10 ft/sec.

14

In Fig. 7 the slashed line in the region of $M_\infty \approx 1.0$ represents the authors' best guess as to the value of C_D. In applying these values to the full-scale sphere, a reduced degree of confidence should be ascribed to upper air density values obtained when $M_\infty \approx 1.0$.

As an item of general interest, Appendix III presents schlieren photographs of sphere shock wave development at transonic speeds.

4.5 SUPERSONIC SPHERE DRAG COEFFICIENTS

A review of Figs. 6k through v reveals that there is a limited amount of data in the $1.0 < M_\infty < 6.0$ regime from other sources for $T_w/T_\infty \approx 1.0$ (Refs. 5, 6, and 8 through 12). These data provide a good indication of the variation of drag coefficient with Reynolds number at a fixed Mach number for $Re_\infty > 10^4$. With the exception of some data obtained at $1.45 < M_\infty < 1.85$ and $200 < Re_\infty < 300$, these data are also in good agreement with present data for $Re_\infty < 10^4$.

It is of interest to consider the form of the C_D-Re_∞ curves shown in Figs. 6k through v. The total drag coefficient of a sphere can be written as the sum of drag components attributable to forebody pressure, afterbody pressure, and friction, viz

$$C_D = C_{DPF} + C_{DPB} + C_{DF}$$

The forebody pressure drag (C_{DPF}) of a sphere can be derived from the pressure distribution over a hemisphere (cf. Refs. 23 and 24). Clark (Ref. 24) has derived a simple expression for forebody drag

$$C_{DPF} = 0.901 - 0.462/M_\infty^2$$

This derivation is in good agreement with Hoerner's (Ref. 23). From a consideration of the experimental measurements of stagnation pressure on source-shaped bodies by Sherman (Ref. 25) shown in Fig. 11, this pressure term would be expected to be essentially constant for $Re_\infty > 3 \times 10^2$.

Lehnert (Ref. 26) has measured the afterbody pressure drag of a sphere over a range of Reynolds numbers. These data are shown in Fig. 12. Some afterbody pressure drag values have been derived from these curves for $Re_\infty \approx 10^6$ and are reported with some similar, more recent data by Jerrell (Ref. 27) in Fig. 13. The two sets of data are in good agreement.

15

the condition where the wall-to-free-stream temperature ratio is unity. When the ballistic range and full-scale spheres operate at conditions where $T_W/T_\infty \approx 1.0$, it is possible to use the ballistic range data directly for the full-scale drag values. To determine whether small changes in wall temperature could affect the drag coefficient significantly, a study was made of several sets of data (Refs. 5 and 30 through 39), where $T_W/T_\infty \neq 1.0$. These data are shown in Figs. 14a through f. The data are plotted with C_D as a function of Re_2 where Re_2 is considered to be a better parameter for comparison than Re_∞ when $M_\infty > 1$. Some of these data (cf. Figs. 14e and f) fall outside the Mach number limits of the present investigation but are included to illustrate the consistent effect of wall temperature upon sphere drag coefficient.

For Figs. 14e and f, the $T_W/T_\infty \approx 1.0$ data have been derived from VKF ballistic range data reported in Ref. 5, together with some hitherto unpublished data obtained between 1965 and 1969. Sphere drag data for $8.5 < M_\infty < 21.5$ are shown in Figs. 15a through c. At low Reynolds numbers there is more scatter in these data than there is for the present investigation. These data, together with the results of the present investigation, are summarized in Fig. 16. It is from Fig. 16 that the $T_W/T_\infty \approx 1.0$ data shown in Figs. 14e and f are derived.

Figure 14a demonstrates the consistency of experimental measurements from a variety of sources. The exception to this good agreement is the data presented in tabular form in Ref. 34 derived from University of Minnesota data referenced in Ref. 1.

All of the data (Figs. 14a through f) show that at a fixed Reynolds number the drag coefficient increases as T_W/T_∞ increases. To illustrate this effect more clearly, the data contained in Fig. 14 have been replotted as C_D versus T_W/T_∞ at various discrete values of Re_2 in Figs. 17a through f. The variation of drag coefficient with velocity and wall temperature has been defined theoretically (cf. Ref. 29) in the free-molecule limit, and the results are summarized in Fig. 18. As the free-molecule limit is approached, the form of the variation of drag coefficient with wall temperature should approach that which exists in the free-molecule limit. The $M_\infty \approx 2.0$ data contained in Fig. 17a is the most complete set of data from which to establish the effect of wall temperature. It is

17

evident from these data that when $C_D \geq 0.7 \, C_{D_{FM}}$ the temperature effects upon drag coefficient approximate those which are predicted theoretically in the free-molecule limit. Therefore, the curves that have been faired through the data in Figs. 17b through f have been based on the assumption that when $C_D \geq 0.7 \, C_{D_{FM}}$ the form of the C_D variation with T_w/T_∞ is that given by theory in the free-molecule limit.

In Figs. 14b, c, and e the C_D versus Re_∞ variation for $T_w/T_\infty \approx 1.0$ is shown as a solid line and a dashed extrapolation. The dashed position of these curves has been derived from data obtained for $T_w/T_\infty > 1.0$ shown in Figs. 17b, c, and e.

In discussions with J. Morrissey of AFCRL, it was indicated that there was an interest in obtaining some estimates of sphere drag at $Re_\infty \approx 1.0$. Using the data contained in Figs. 14a through f and 17a through f, some engineering extrapolations outside the scope of the experimental data have been made to satisfy this requirement. The result is given in Fig. 19. Obviously, there is an increased uncertainty in these values of drag coefficient.

The results that have been discussed in this section have been obtained in (1) ballistic ranges where the deceleration may be high, e. g., >100 g; (2) free flight in wind tunnels where the acceleration is low, $0[1\,g]$; and (3) models mounted on a balance in a wind tunnel where there is no acceleration. The effect of acceleration on the drag of spheres and cylinders has been investigated by several authors (Refs. 40 and 41.) Any differences in the measured drag coefficients discussed here can be shown to be caused by differences in wall temperature. This suggests that acceleration (or deceleration) has had no effect upon the sphere drag coefficient for the levels encountered in the ballistic range during these tests.

4.7 EFFECT OF SURFACE IRREGULARITIES AND MODEL SCALE ON DRAG COEFFICIENT

The ROBIN Sphere has six dimples in its surface caused by the holddown points of the internally mounted radar reflector. An approximation to these surface irregularities has been made on some spheres launched in support of this test program. Also, an investigation has been made of physical model scale at one specific condition. The results are listed below.

M_∞	Re_∞	C_D	Surface	d, in.	Material
0.268	10,625	0.412	Smooth	1.00	Nylon
0.263	10,386	0.412			
0.261	10,353	0.411			
0.254	10,118	0.420	↓		
0.253	10,121	0.419	Dimpled		
0.253	10,088	0.420			
0.253	10,081	0.416	↓	↓	↓
0.246	9,884	0.420	Smooth	0.25	Steel
0.246	9,871	0.419	Smooth	0.25	Steel

These results indicate that for the conditions of this investigation there
are no significant effects of scale or surface irregularity on sphere
drag coefficient which is seen to vary only ±1 percent from the mean
in all cases represented in the above table. Sivier (Ref. 17) tested
some moderately roughened spheres at $Re_\infty < 2 \times 10^3$ and found no effect
upon the sphere drag coefficient at $M_\infty = 0.16$.

4.8 DRAG COEFFICIENT AT HIGH SPEEDS

As can be seen from Section 5.6, there is not a large body of ex-
perimental data concerning the effects of wall temperature upon drag
coefficient. Consequently, to make use of as much of the available
data as possible concerning the effect of wall temperature, it has been
necessary to consider data at speeds higher than that required in the
present investigation. This has resulted in the derivation of C_D versus
M_∞ curves at fixed Reynolds numbers shown in Fig. 16.

At first sight, the form of the C_D versus M_∞ curve at low Reynolds
numbers appears to exhibit an unexpected variation. However, it must
be remembered that Knudsen number is a more realistic indicator of
the approach to the free-molecule limit rather than Reynolds number.
In fact, Knudsen number is proportional to M_∞/Re_∞. This means that
for $Re_\infty = 20$ the Knudsen number at $M_\infty = 20$ is twice that for $M_\infty = 10$.
This in turn means that the $M_\infty = 20$ condition is closer to the free-
molecule limit than the $M_\infty = 10$ condition even when Re_∞ is the same.
This explains why the high Mach number drag values are closer to the
free-molecule limits than the low Mach number values.

SECTION V
CONCLUSIONS

Measurements have been made such that reliable values of sphere
drag coefficient may be derived for any value of M_∞ and Re_∞ for

$T_w/T_\infty \approx 1.0$ within the bounds $0.1 < M_\infty < 6.0$ and $2 \times 10^1 < Re_\infty < 10^5$ with an uncertainty no larger than ± 2 percent.

Based on these and other published data, there is sufficient information contained herein to predict the effect of wall temperature on C_D when $T_w/T_\infty \neq 1.0$ for $2.0 < M_\infty < 6.0$.

From the present results and those obtained elsewhere, no measurable effect of acceleration upon drag can be detected, and, therefore, no effect is expected under the conditions of the ROBIN and "Instrumented Spheres" programs.

A brief investigation of model scale and surface irregularities indicates that for $M_\infty \approx 0.25$ and $Re_\infty \approx 10^4$ no effect on drag could be measured.

There is reasonable agreement between the present low speed data ($M_\infty < 0.25$ and $Re_\infty \leq 10^4$) and the classical data which has resulted in the derivation of the "standard drag curve." Any differences in the two sets of data may be explainable in terms of velocity differences in the basic data.

The present investigation represents the most comprehensive experimental program to date to define sphere drag in the velocity-altitude regime of interest in the "falling sphere" programs for measuring upper air density. It is believed that the present C_D, M_∞, and Re_∞ map is the most accurate produced to this time.

REFERENCES

1. "Status of Passive Inflatable Falling-Sphere Technology for Atmospheric Sensing to 100 Km." A symposium held at Langley Research Center, Hampton, Virginia, September 23-24, 1969. NASA SP-219.

2. Lawrence, W. R. "Free-Flight Range Measurements of Sphere Drag at Low Reynolds Numbers and Low Mach Numbers. AEDC-TR-67-218 (AD660545), November 1967.

3. Arney, G. D., Jr. and Henderson, W. F. "A Portable Calibrator for Intermediate Range Vacuum Gages." AEDC-TR-67-83 (AD645279), May 1967.

20

4. Bailey, A. B. and Koch, K. E. "Launching of Foamed Plastic Models with a Two-Stage Light-Gas Gun." AEDC-TR-66-60 (AD632925), May 1966.

5. Bailey, A. B. "Sphere Drag Measurements in an Aeroballistics Range at High Velocities and Low Reynolds Numbers." AEDC-TR-66-59 (AD633278), May 1966.

6. Charters, A. and Thomas, R. "The Aerodynamic Performance of Small Spheres from Subsonic to High Supersonic Velocities." Journal of the Aeronautical Sciences, Vol. 12, No. 4, October 1945, pp. 468-476.

7. Naumann, A. "Aerodynamishe Gesichtspinkte Der Windkomalentwickling." Jarbruch 1954. Der Wissen-schafthichen Gesellsehaft Luer Luftfahrt, E. V. (WGL).

8. May, A. and Witt, A. "Free-Flight Determinations of the Drag Coefficients of Spheres." Journal of the Aeronautical Sciences, Vol. 20, No. 9, September 1953, pp. 635-638.

9. May, A. "Supersonic Drag of Spheres at Low Reynolds Numbers in Free Flight." Navord R-4392, December 1956.

10. Clark, A. B. J. and Harris, F. T. "Free-Flight Air Drag Measurement Techniques." Journal of the Aeronautical Sciences, Vol. 19, No. 6, June 1952, pp. 385-390.

11. Riess, M. "On Measuring the Coefficient of Drag of an Accelerometer-Instrumented Sphere in a Shock Tube." NOL-TR-62-102, August 1962.

12. Hodges, A. J. "The Drag Coefficient of Very High Velocity Spheres." Journal of the Aeronautical Sciences, Vol. 24, No. 10, October 1957, pp. 755-758.

13. Eisner, F. "Das Widerstandsproblem." Proceedings of the Third International Congress on Applied Mechanics, Stockholm, 1931.

14. Wieselberger, C. "Wietere Feststellungen uber die Giesetze des Thussigk eits-und Luftwiderstandes." Z. Physik, Vol. 23, 1922, pp. 219-224.

15. Lunnon, R. G. "Fluid Resistance to Moving Sphere." Proceedings of the Royal Society of London. Series A, Vol. 118, April 2, 1928, pp. 680-694.

16. Heinrich, H. G., Niccum, R. J., and Haak, E. L. "The Drag Coefficient of a Sphere Corresponding to a 'One Meter ROBIN Sphere' Descending from 260,000 ft Altitude (Reynolds Nos. 789

to 23,448, Mach Nos. 0.056 to 0.90)." Research and Development of ROBIN Meteorological Rocket Balloon, Vol. II, Contract No. AF 19(604)-8034, University of Minnesota, May 1963 (AD480309).

17. Sivier, K. R. "Subsonic Sphere Drag Measurements at Intermediate Reynolds Numbers." PhD Thesis, The University of Michigan, Ann Arbor, Michigan, 1967.

18. Zarin, N. A. "Measurement of Non-Continuum and Turbulence Effects on Subsonic Sphere Drag." PhD Thesis, The University of Michigan, Ann Arbor, Michigan, 1969.

19. Millikan, C. B. and Klein, A. L. "The Effect of Turbulence." Aircraft Engineering, August 1933, p. 169.

20. Dryden, H. L. and Kuethe, A. M. "Effect of Turbulence in Wind Tunnel Measurements." NACA Report 342, 1930.

21. Probstein, R. F. and Fassio, F. "Dusty Hypersonic Flows." AIAA Journal, Vol. 8, No. 4, April 1970, pp. 772-779.

22. Ingebo, R. D. "Drag Coefficients for Droplets and Solid Spheres in Clouds Accelerating in Airstreams." NACA TN 3762, 1962.

23. Hoerner, S. F. "Fluid-Dynamic Drag." Published by the author, Midland Park, New Jersey, 1958.

24. Clark, E. L. "Aerodynamic Characteristics of the Hemisphere at Supersonic and Hypersonic Mach Numbers." AIAA Journal, Vol. 7, No. 7, July 1969, pp. 1385-1386.

25. Sherman, F. S. "New Experiments on Impact-Pressure Interpretation in Supersonic and Subsonic Rarefied Air Streams." NACA TN 2995, September 1953.

26. Lehnert, R. "Base Pressure of Spheres at Supersonic Speeds." Navord Report 2774, U. S. Naval Ordnance Laboratory, February 1953.

27. Jerrell, L. S. "Aerodynamic Characteristics of an Oblate Spheroid and a Sphere at Mach Numbers from 1.70 to 10.49." NASA TN D-5600, January 1970.

28. Davis, R. T. and Flügge-Lotz, I. "Second-Order Boundary-Layer Effects in Hypersonic Flow Past Axisymmetric Bodies." Journal of Fluid Mechanics, Vol. 20, Part 4, 1964, pp. 593-673.

29. Hayes, D. and Probstein, R. F. Hypersonic Flow Theory. Academic Press, 1959.

30. Aroesty, J. "Sphere Drag on a Low Density Flow." University of California Report No. HE-150-192, January 1962.

31. Ashkenas, H. I. "Sphere Drag at Low Reynolds Numbers and Supersonic Speeds." Jet Propulsion Laboratory Research Summary No. 36-12, Vol. 1, January 1962.

32. Sreekanth, A. K. "Drag Measurements on Circular Cylinders and Spheres in the Transition Regime at a Mach Number of 2." UTIAS, Report No. 74, April 1961.

33. Ashkenas, H. "Low-Density Sphere Drag with Equilibrium and Non-Equilibrium Wall Temperature." Jet Propulsion Laboratory Technical Report No. 32-442, August 1963.

34. Engler, N. A. "Development of Methods to Determine Winds, Density, Pressure and Temperature from the ROBIN Falling Balloon." University of Dayton Research Institute, Dayton Ohio, AFCRL-65-448, May 1965.

35. Potter, J. L. and Miller, J. T. "Consideration of Simulation Parameters for Blunt Thick Bodies in Rarefied High-Speed Flows." AEDC-TR-68-242 (AD678159), November 1968.

36. Wegener, P. and Ashkenas, H. "Wind Tunnel Measurement of Sphere Drag at Supersonic Speeds and Low Reynolds Numbers." Journal of Fluid Mechanics, Vol. 4, No. 10, 1961, pp. 550-558.

37. Whitfield, D. L. and Stephenson, W. B. "Sphere Drag in the Free Molecular and Transitional Flow Regimes." AEDC-TR-70-32 (AD704122), April 1970.

38. Kinslow, M. and Potter, J. L. "The Drag of Spheres in Rarefied Hypervelocity Flow." AEDC-TDR-62-205 (AD290519), December 1962.

39. Phillips, W. M. and Kuhlthau, A. R. "Drag Measurements on Magnetically Supported Spheres in Low-Density High-Speed Flow." Proceedings of the Sixth International Symposium on Rarefied Gas Dynamics, Vol. 1, Academic Press, 1969.

40. Selberg, B. P. and Nichols, J. A. "Drag Coefficient of Small Spherical Particles." AIAA Journal, Vol. 6, No. 3, March 1968.

41. Sarpkaya, T. "Separated Flow about Lifting Bodies and Impulsive Flow about Cylinders." AIAA Journal, Vol. 4, No. 3, March 1966.

APPENDIXES
I. ILLUSTRATIONS
II. TABLES
III. DEVELOPMENT OF SHOCK PATTERNS AT TRANSONIC SPEEDS
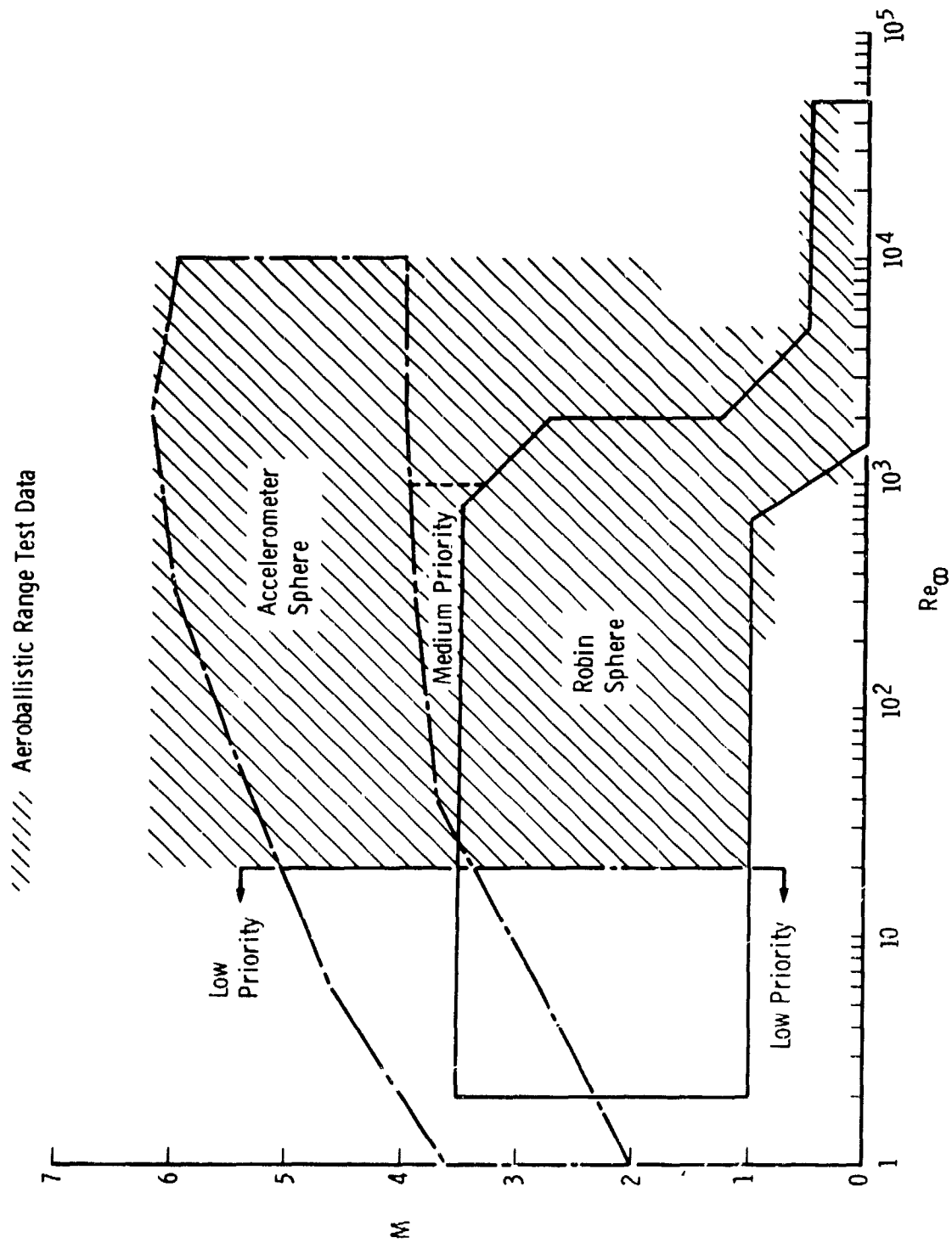IV. ESTIMATION OF C_D AT $M_\infty = 0$

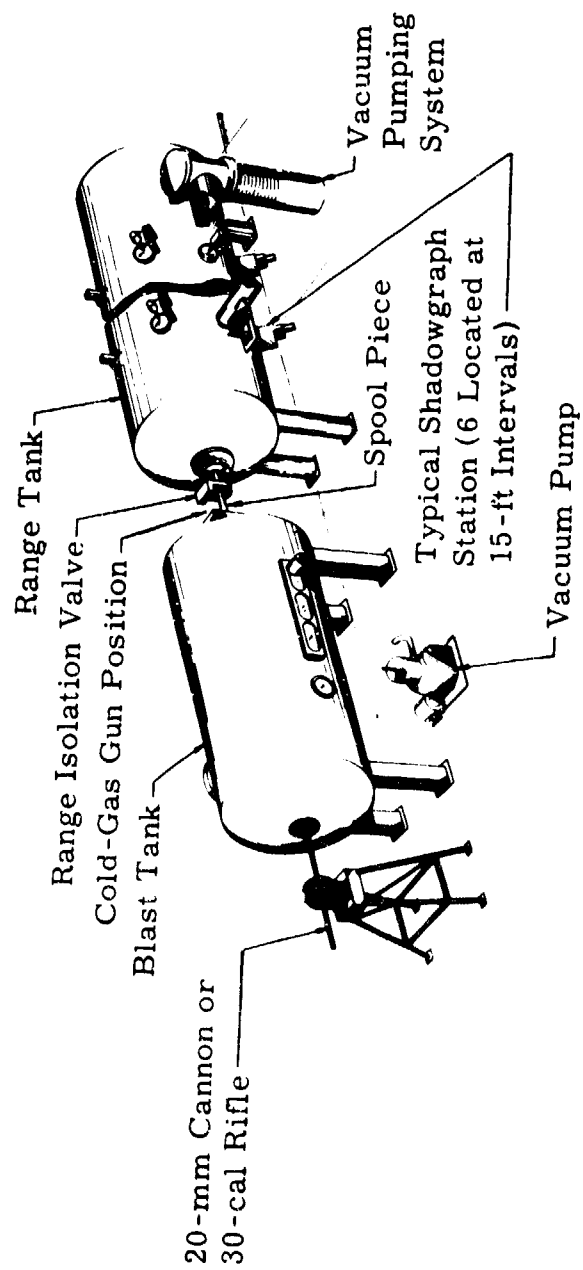Fig. 1 Envelope of AFCRL Falling Sphere Trajectories

Fig. 2 Range K

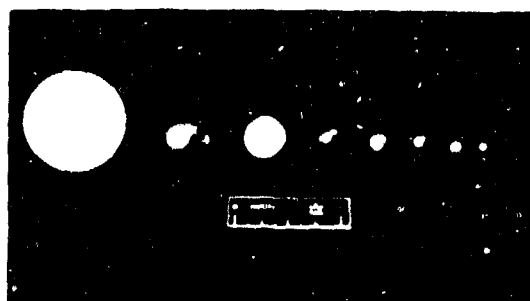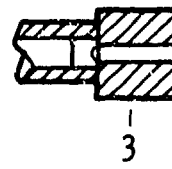a. Cold-Gas Gun Sabots

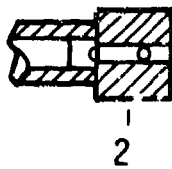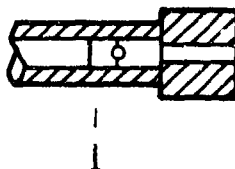b. 20-mm-Cannon Sabots

c. Rifle Sabot

Size and Material of the Spheres, from left to right, respectively, are as follows:

1-in. -diam Nylon
1/2-in. -diam Copper
7/16-in. -diam Dylite
3/8-in. -diam Stainless Steel
1/4-in. -diam Aluminum
1/4-in. -diam Beryllium-Copper
1/8-in. -diam Lexan
3/32-in. -diam Nylon

d. Typical Spheres Used in this Test

Fig. 3 Sabots and Spheres

29

1. MODEL AND SABOT TOGETHER IN LAUNCH TUBE.
2. MODEL AND SABOT SEPARATED AFTER SABOT STOPPED IN LAUNCH TUBE.
3. SPHERE GOES ON DOWN RANGE.

a. Cold-Gas Gun Stripping
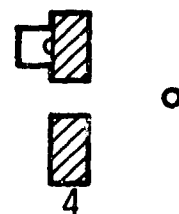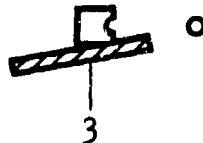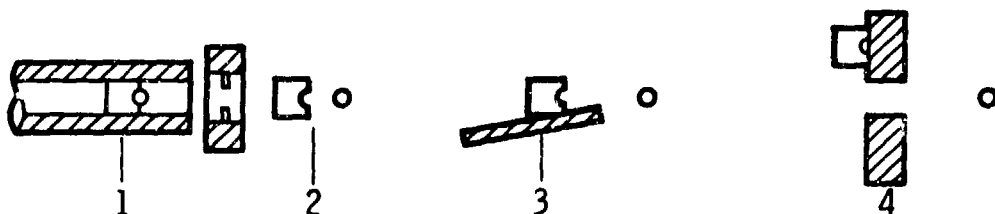
1. MODEL AND SABOT TOGETHER IN LAUNCH TUBE.
2. MODEL AND SABOT SEPARATED AFTER PASSING THROUGH PIN OR WASHER STRIPPER.
3. SABOT STRIKES ANGLED RAMP AND DEFLECTS VERTICALLY.
4. SABOT STRIKES CATCHER PLATE - SPHERE PASSES THROUGH HOLE AND ON DOWN RANGE.

b. 20-mm-Cannon Stripping
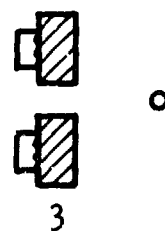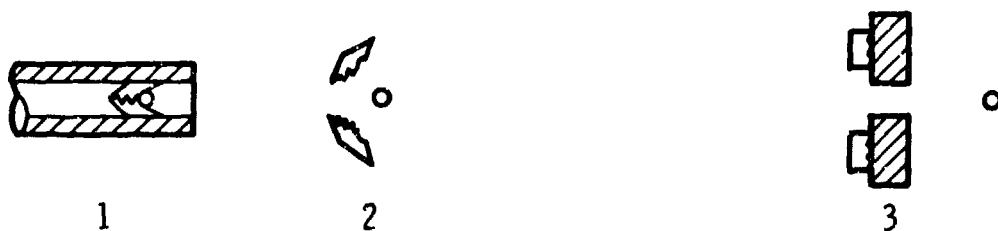
1. MODEL AND SABOT TOGETHER IN RIFLED LAUNCH TUBE.
2. PETALLED SABOT SPREADING UNDER ACTION OF CENTRIFUGAL FORCES.
3. SABOT ARRESTED BY CATCHER PLATE - SPHERE PASSES THROUGH HOLE AND ON DOWN RANGE.

c. Rifle Stripping

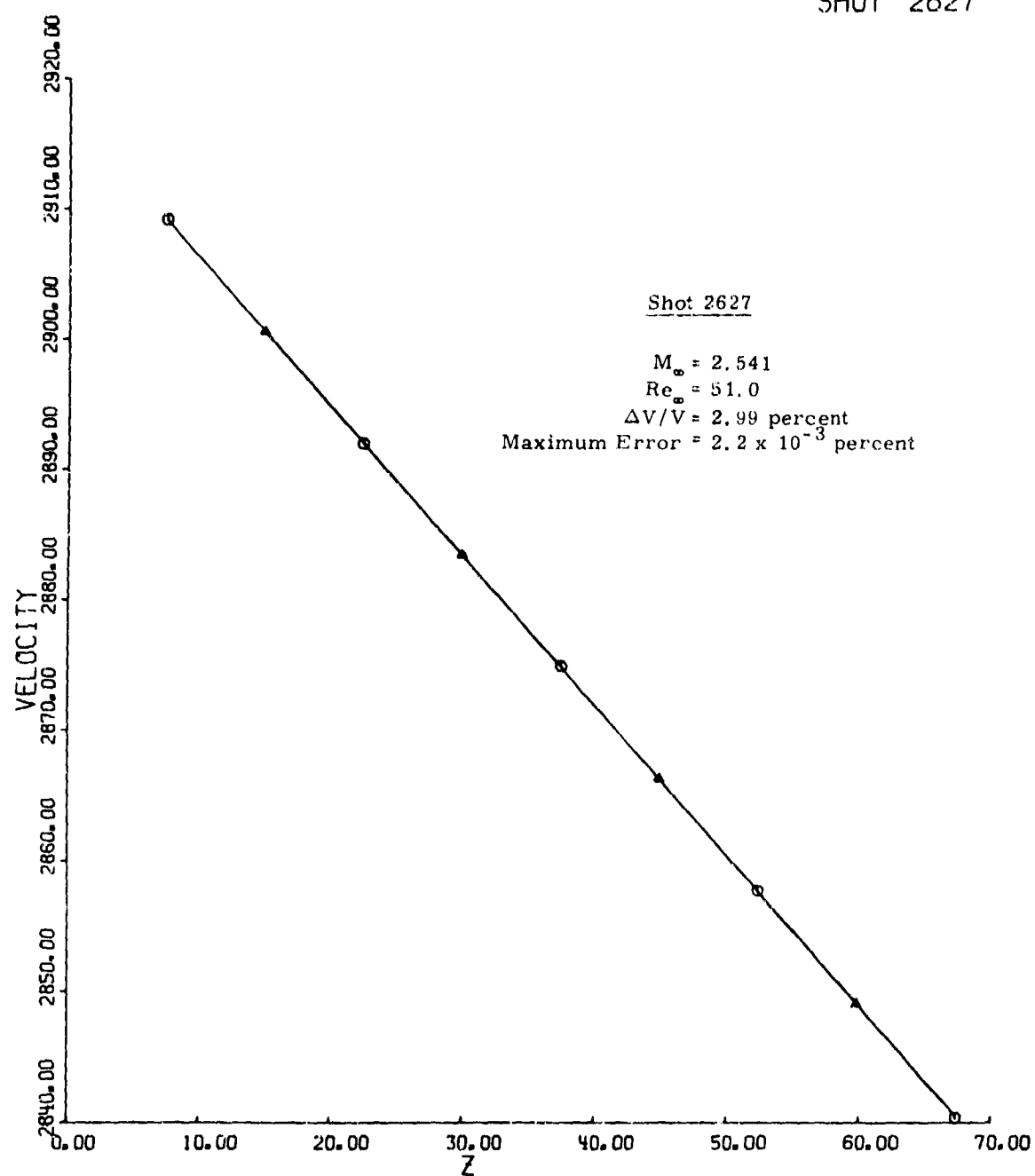Fig. 4 Model Separation Techniques Used in Range K

SHOT 2627

Shot 2627

$M_\infty = 2.541$
$Re_\infty = 51.0$
$\Delta V/V = 2.99$ percent
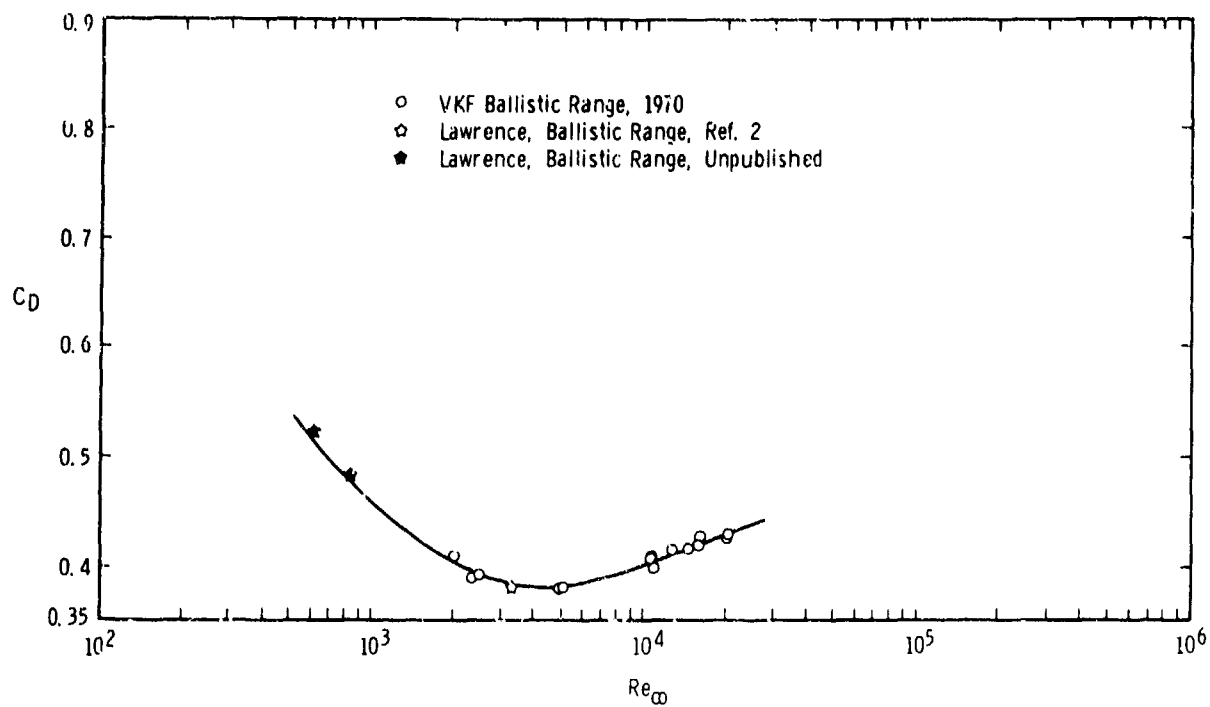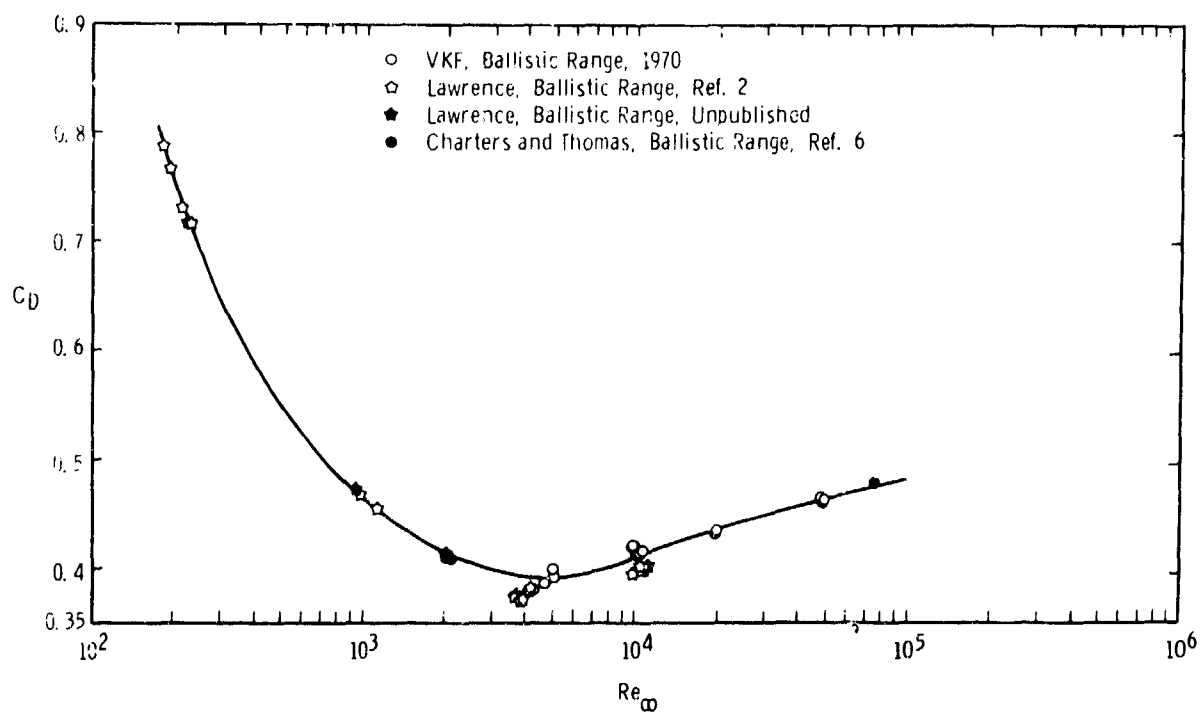Maximum Error $= 2.2 \times 10^{-3}$ percent

Fig. 5 Typical Least-Squares Linear Fit to Velocity-Distance Data

31

a. $0.12 \leqslant M_\infty \leqslant 0.18$

b. $0.19 \leqslant M_\infty \leqslant 0.27$

Fig. 6 Variation of Sphere Drag Coefficient with Reynolds Number

32
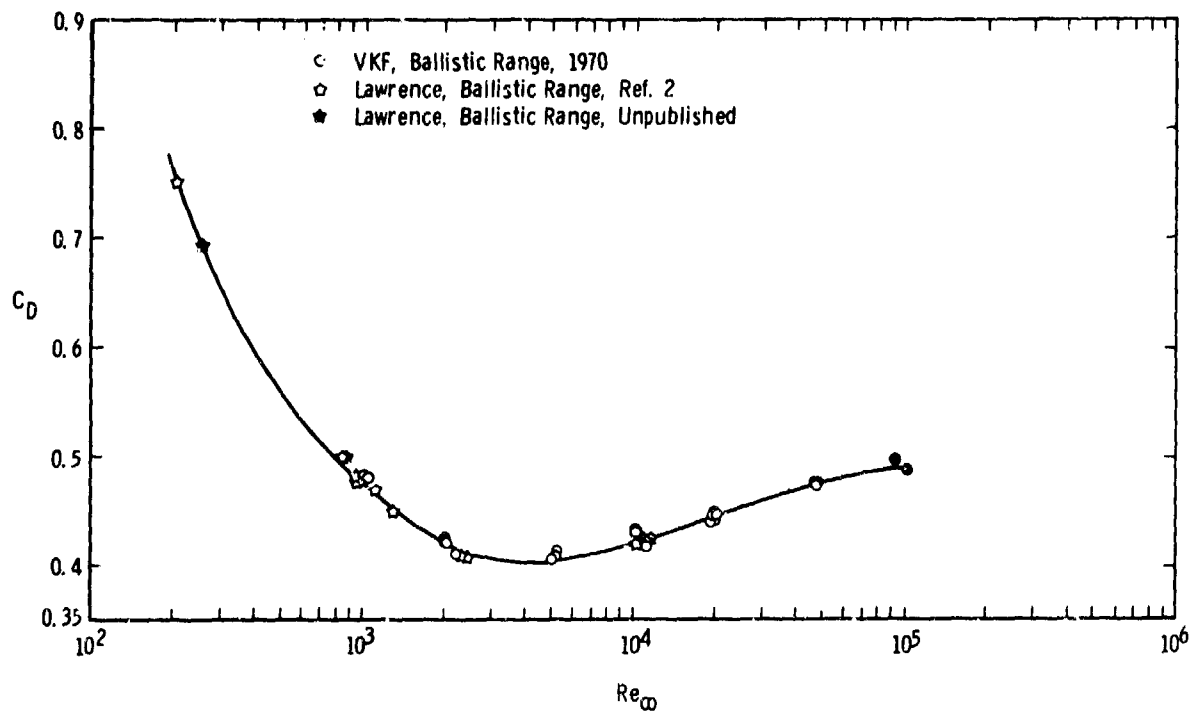
c. $0.28 \leqslant M_\infty \leqslant 0.42$
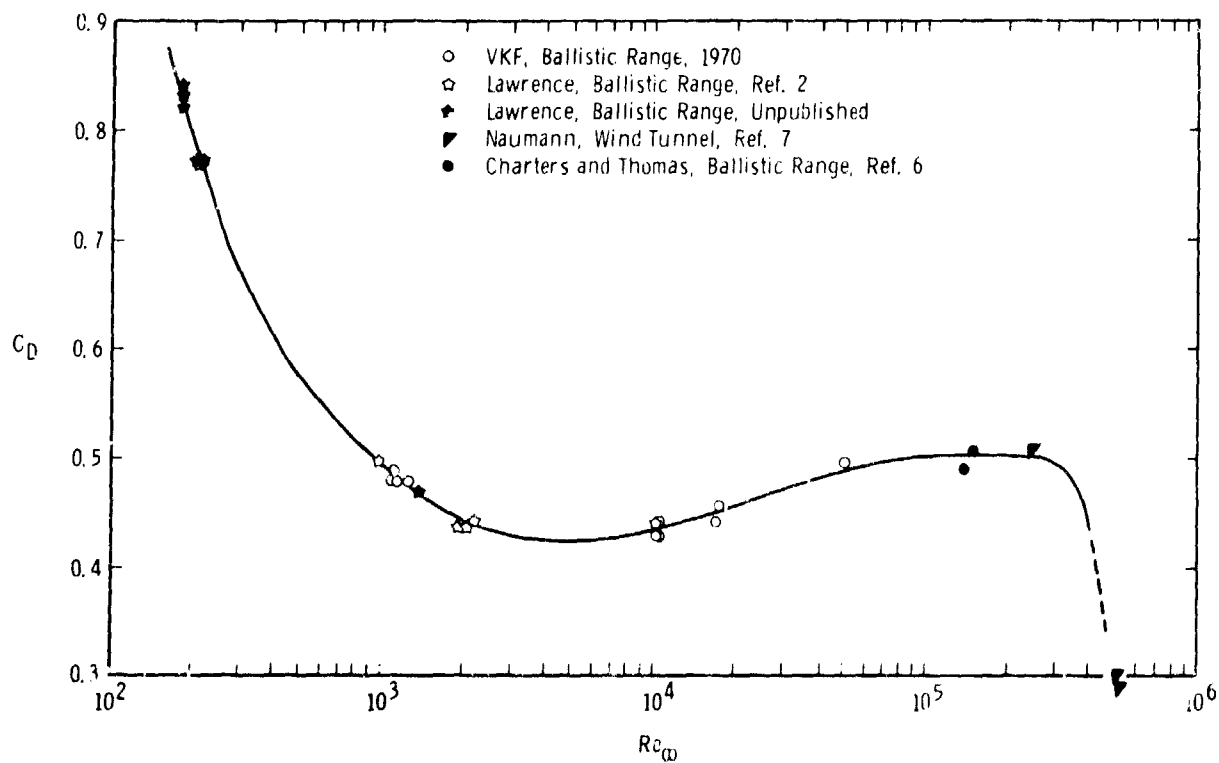
d. $0.43 \leqslant M_\infty \leqslant 0.55$

Fig. 6 Continued
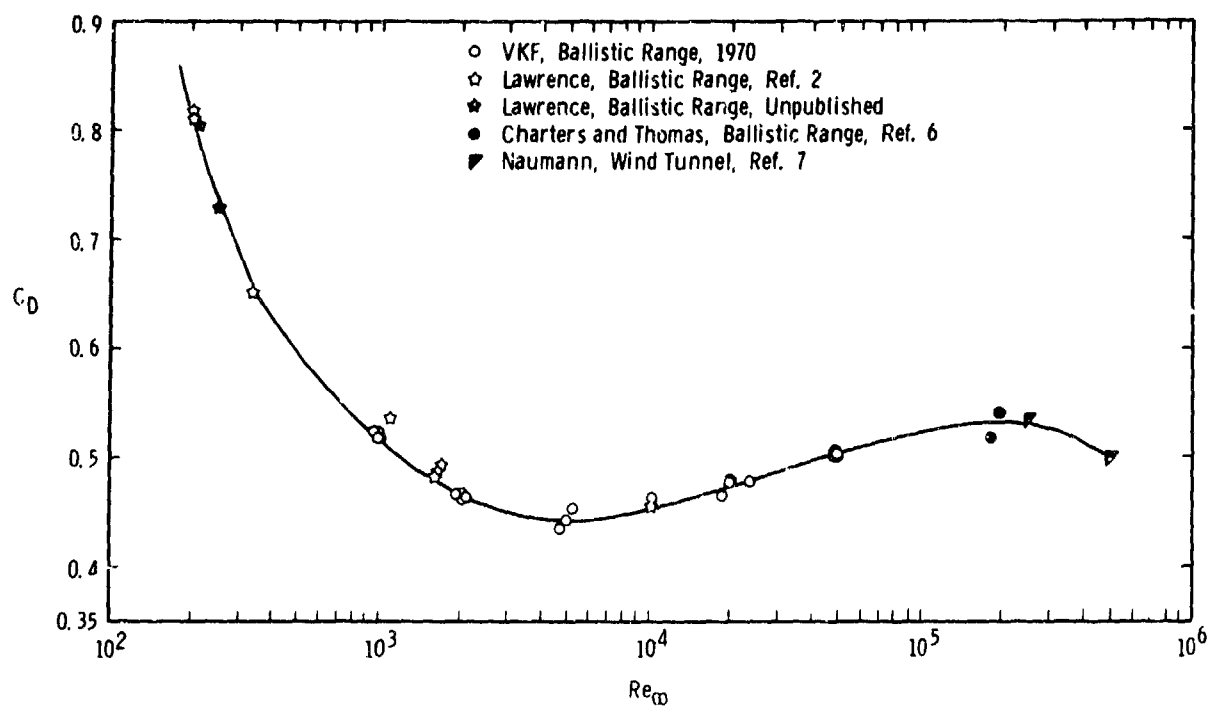
e. $0.57 \leqslant M_\infty \leqslant 0.63$
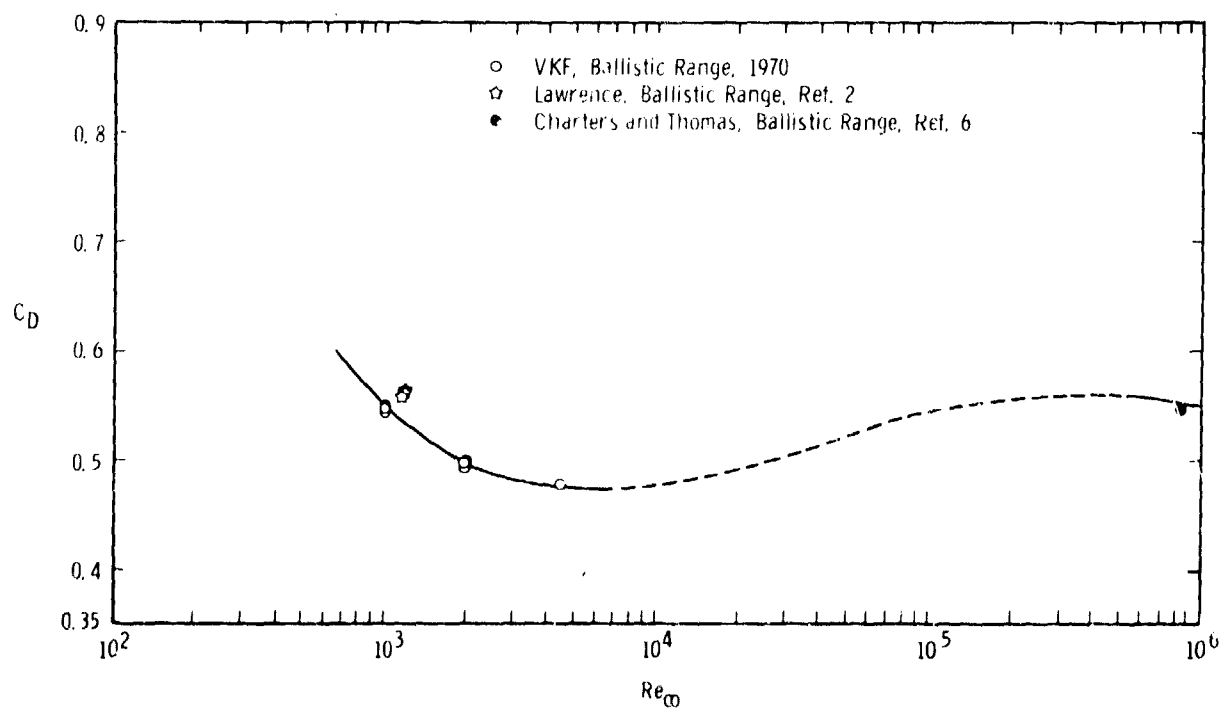
f. $0.70 \leqslant M_\infty \leqslant 0.74$

Fig. 6 Continued

34
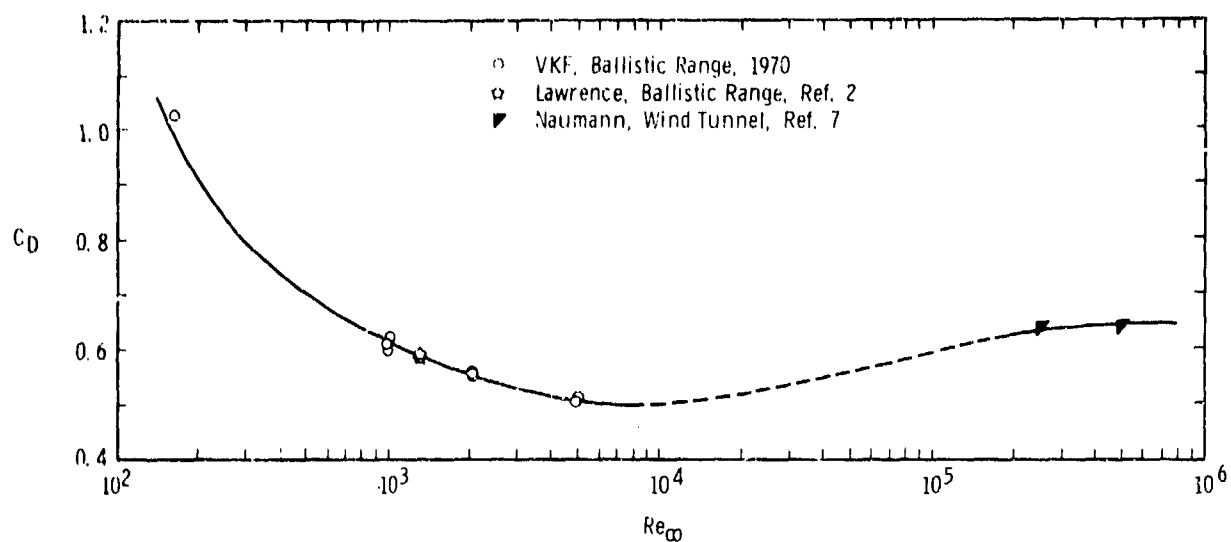
g. $0.79 \leqslant M_\infty \leqslant 0.83$
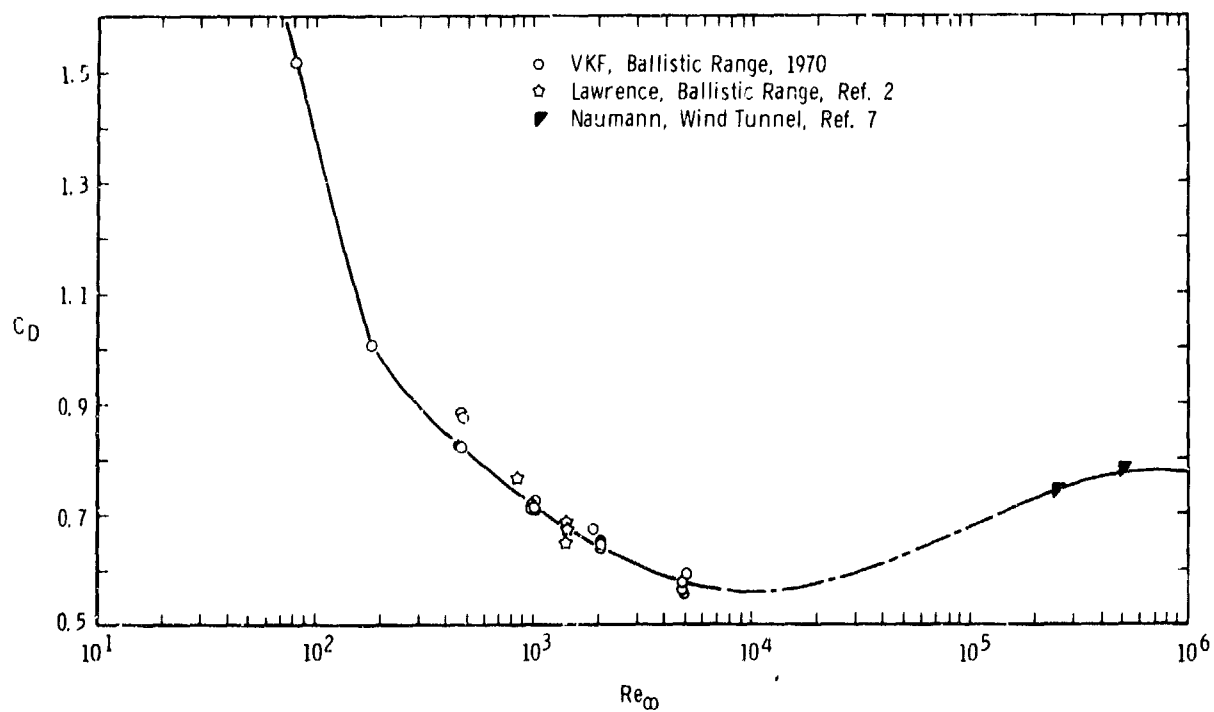
h. $0.88 \leqslant M_\infty \leqslant 0.95$

Fig. 6 Continued

35
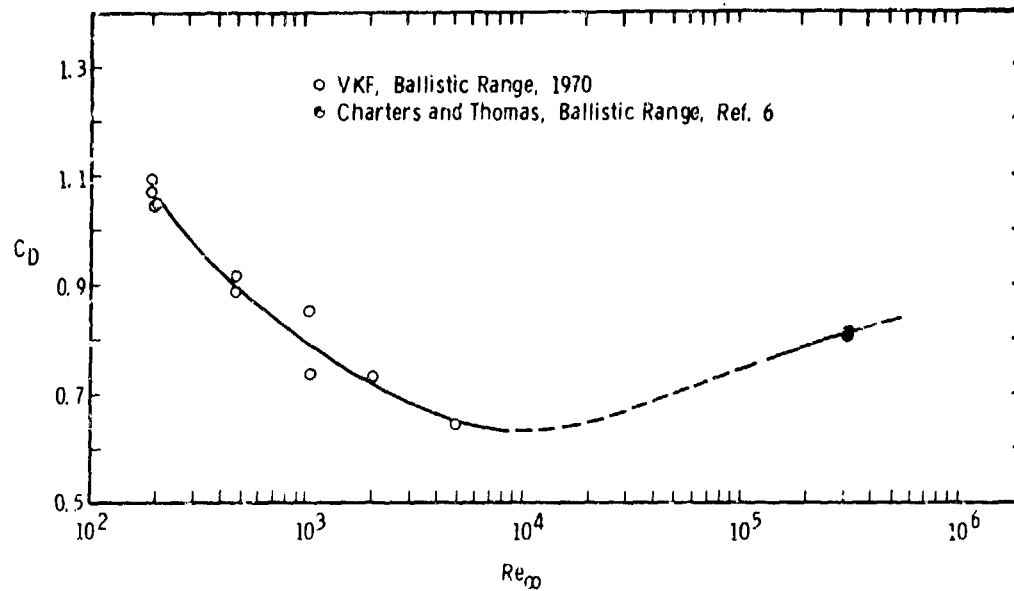
i. $0.96 \leqslant M_\infty \leqslant 0.97$
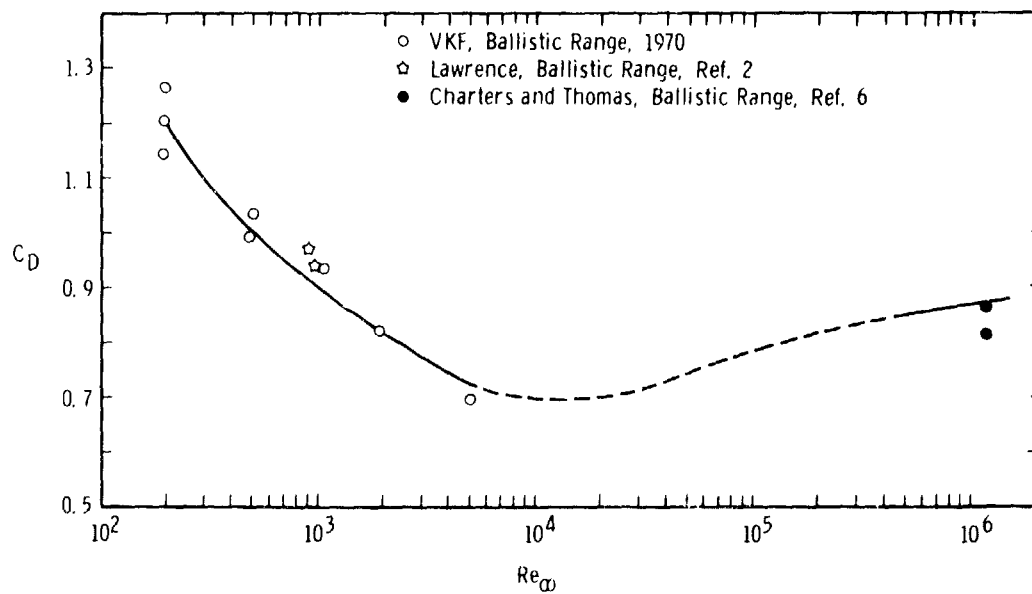
j. $0.98 \leqslant M_\infty \leqslant 0.998$

Fig. 6 Continued

36
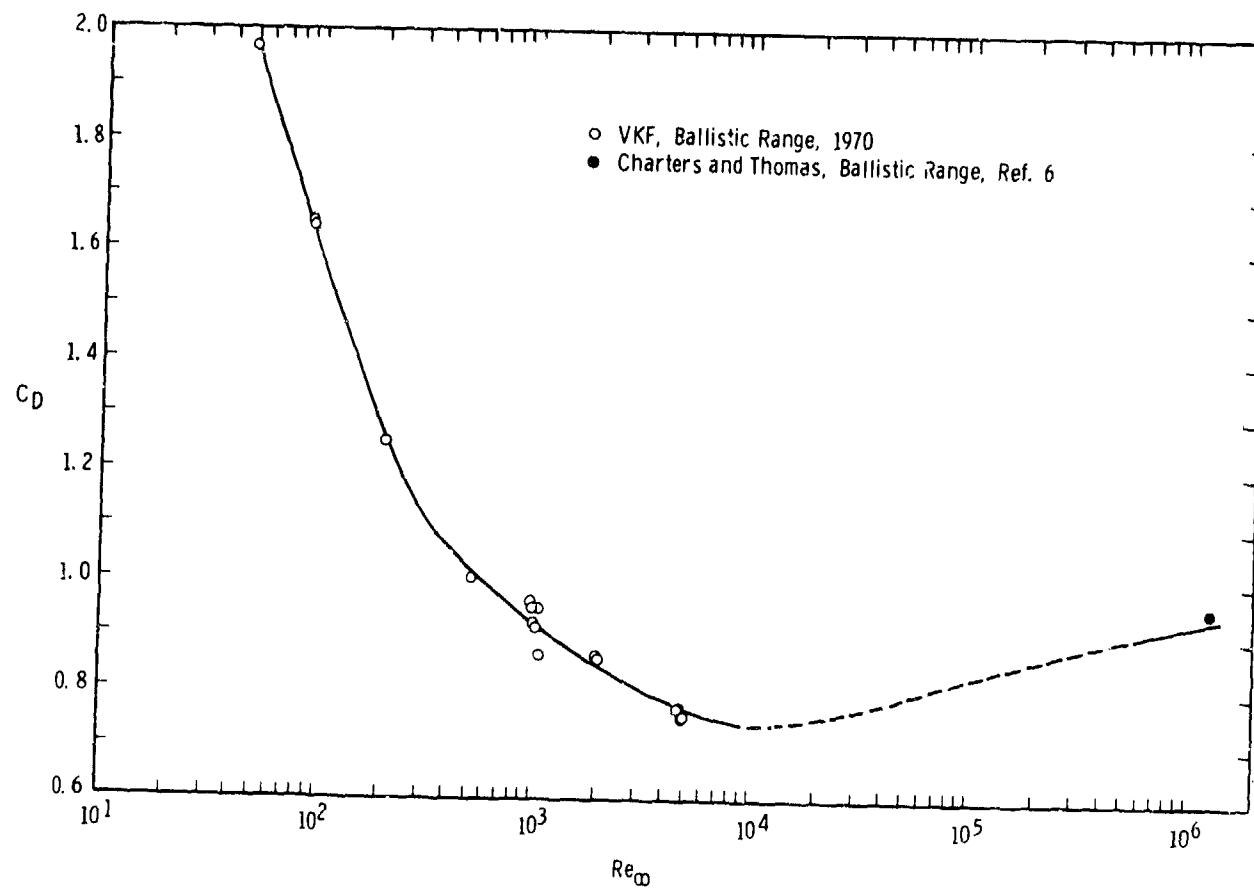
k. $1.003 \leqslant M_\infty \leqslant 1.07$
Fig. 6 Continued

37
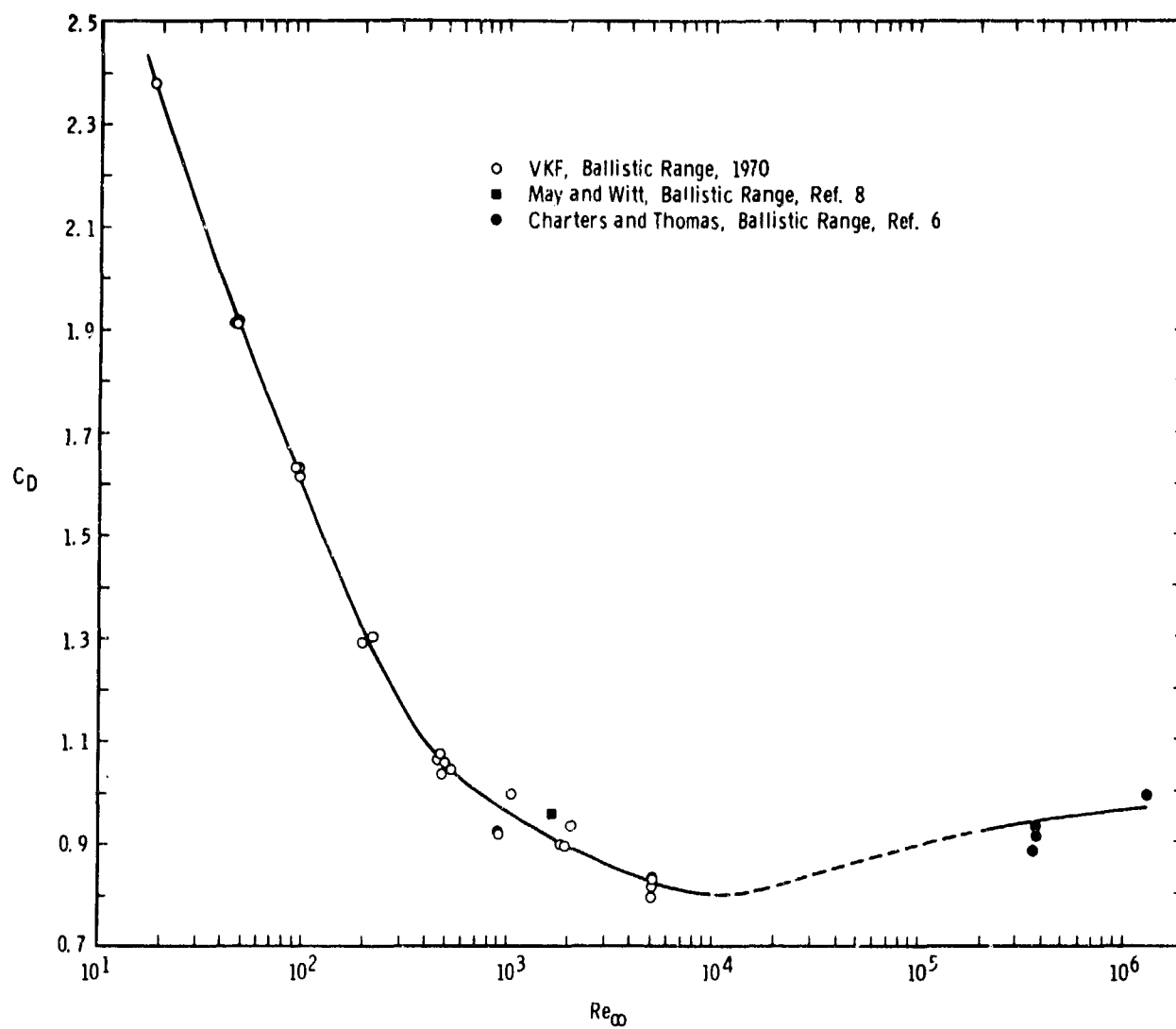
I. $1.08 \leqslant M_{\infty} \leqslant 1.19$

Fig. 6 Continued

38
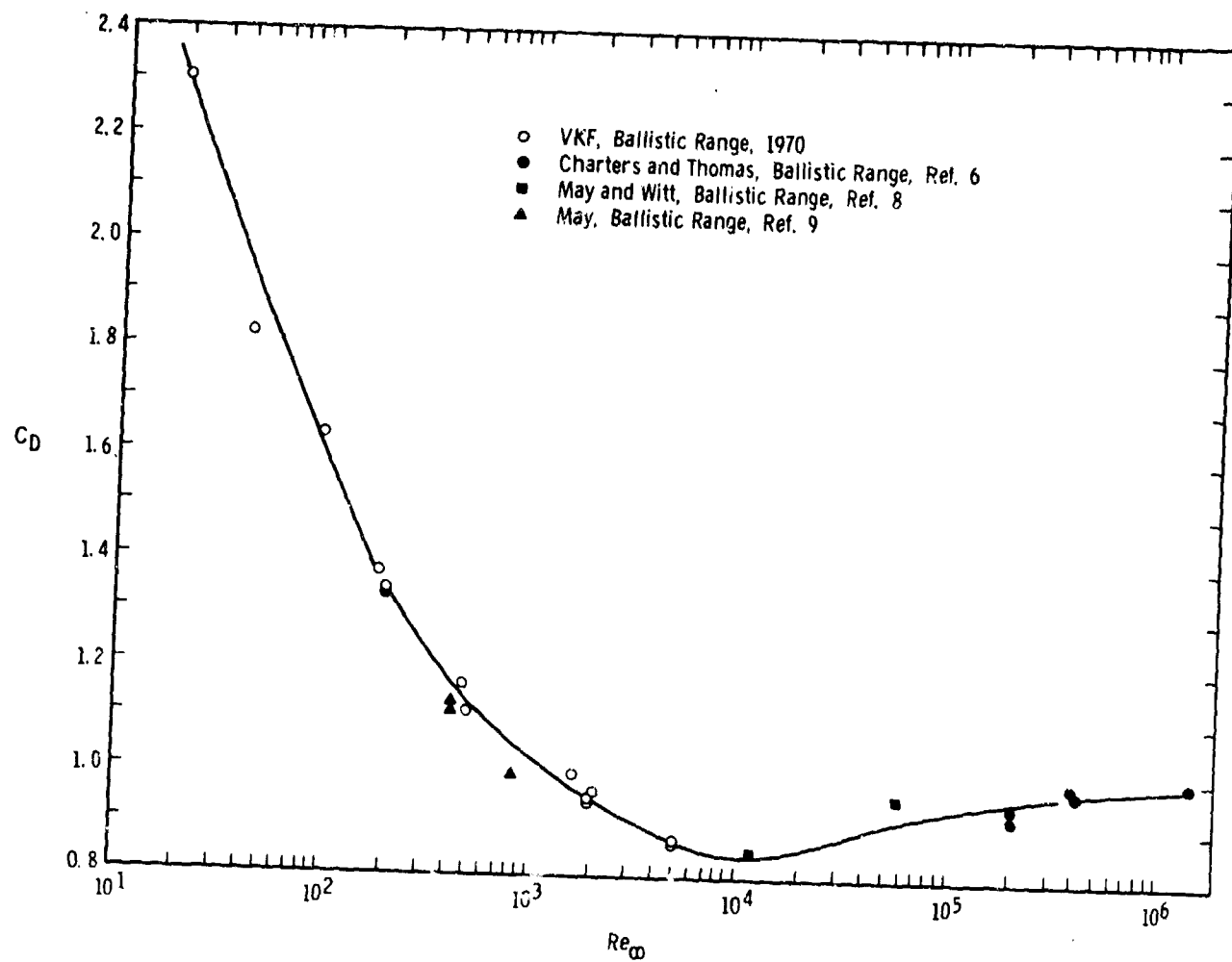
m. $1.2 \leqslant M_\infty \leqslant 1.3$
Fig. 6 Continued
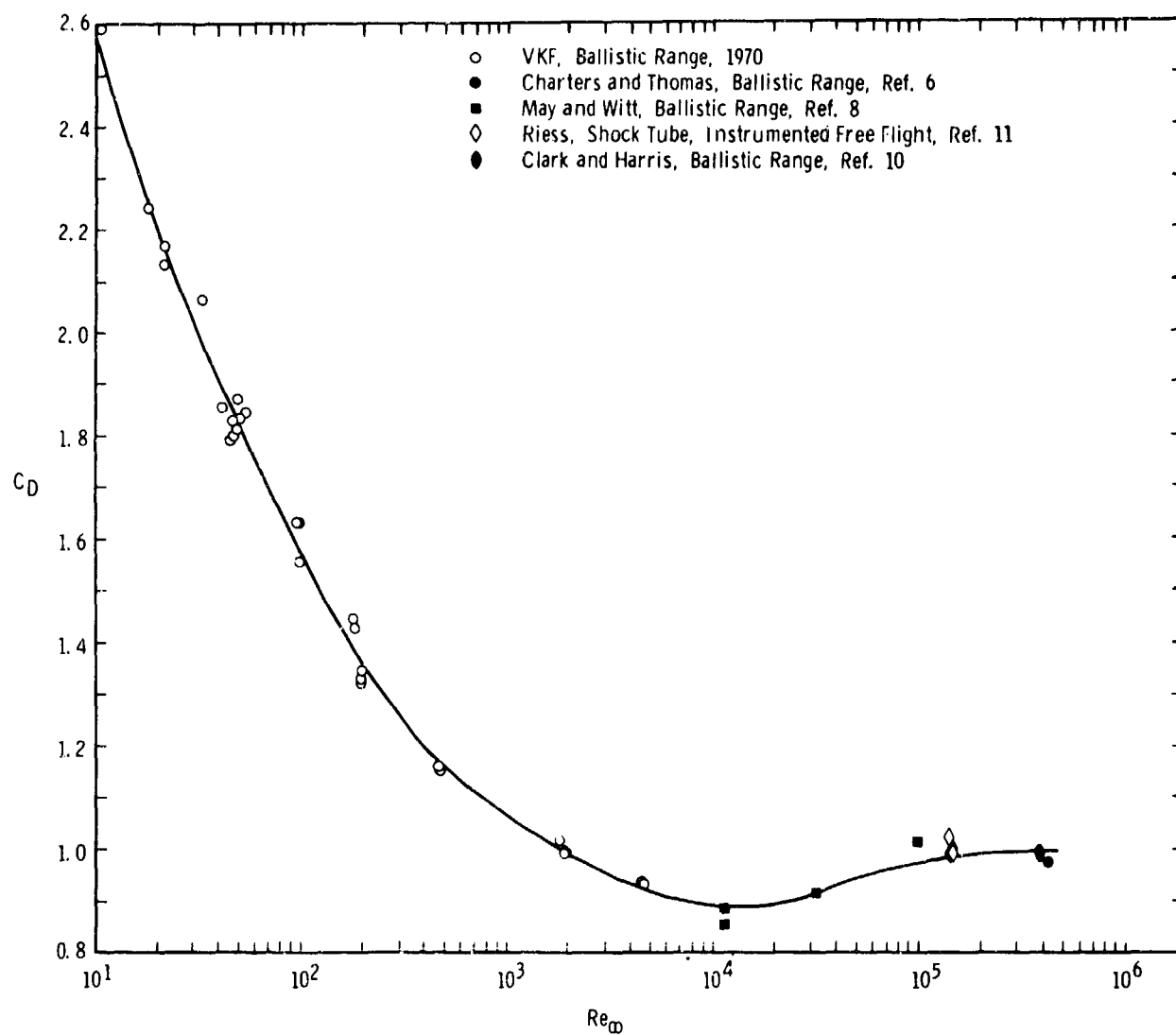
n. $1.3 \leqslant M_\infty \leqslant 1.45$
Fig. 6 Continued

40
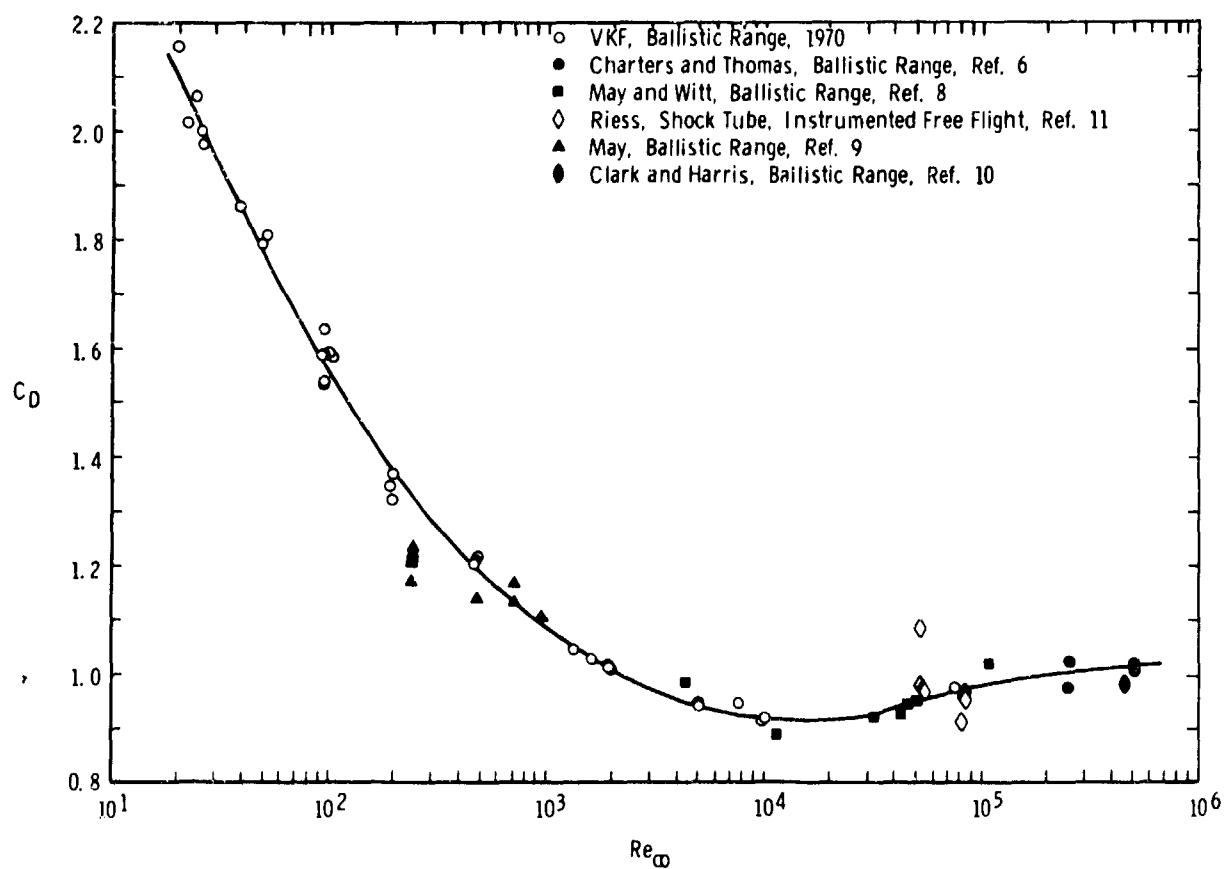
o. $1.45 \leqslant M_\infty \leqslant 1.65$

Fig. 6 Continued

41

p. $1.65 \leq M_\infty \leq 1.85$
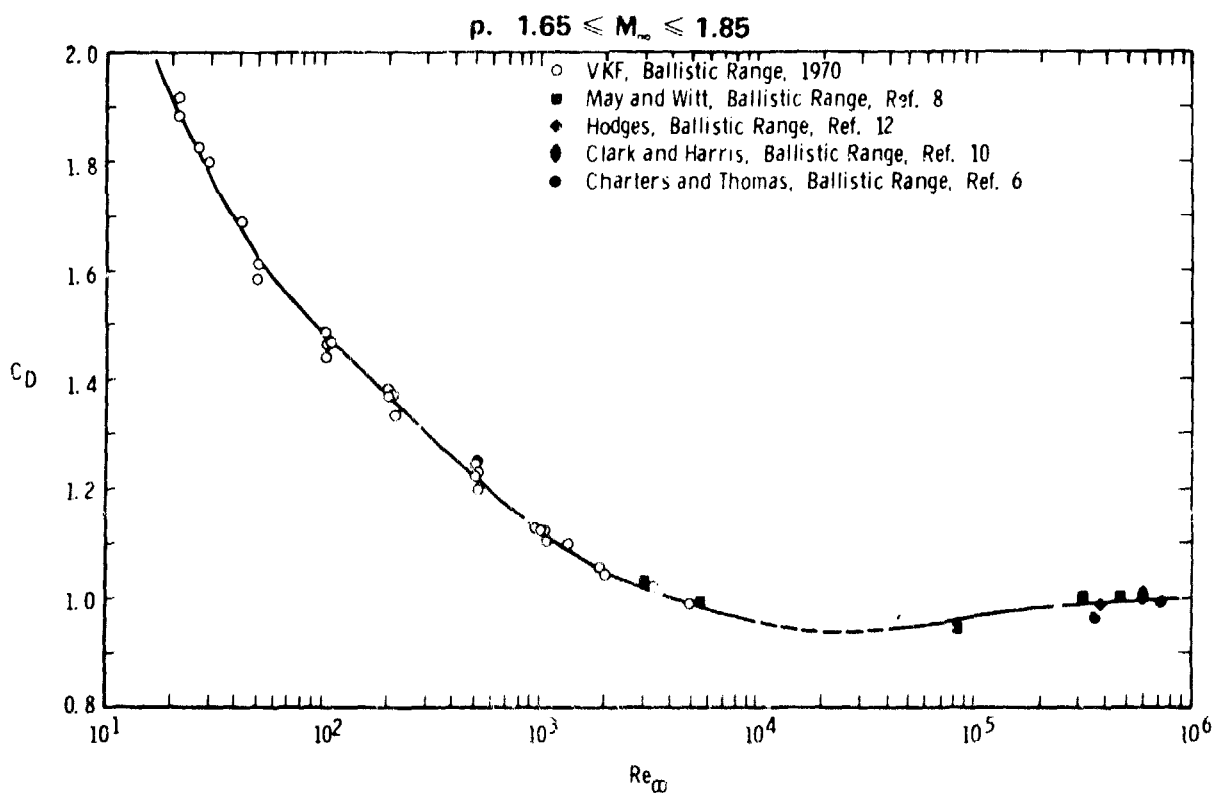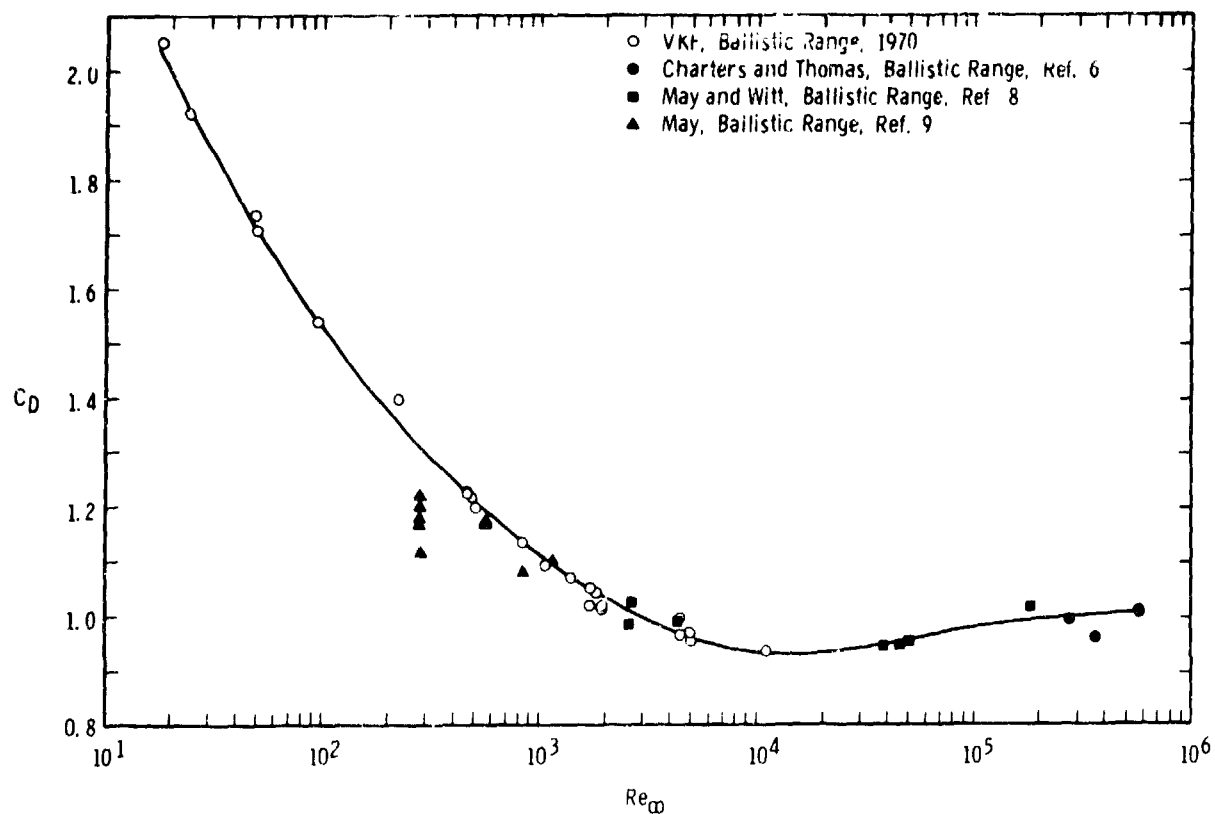
q. $1.9 \leq M_\infty \leq 2.2$
Fig. 6 Continued

42
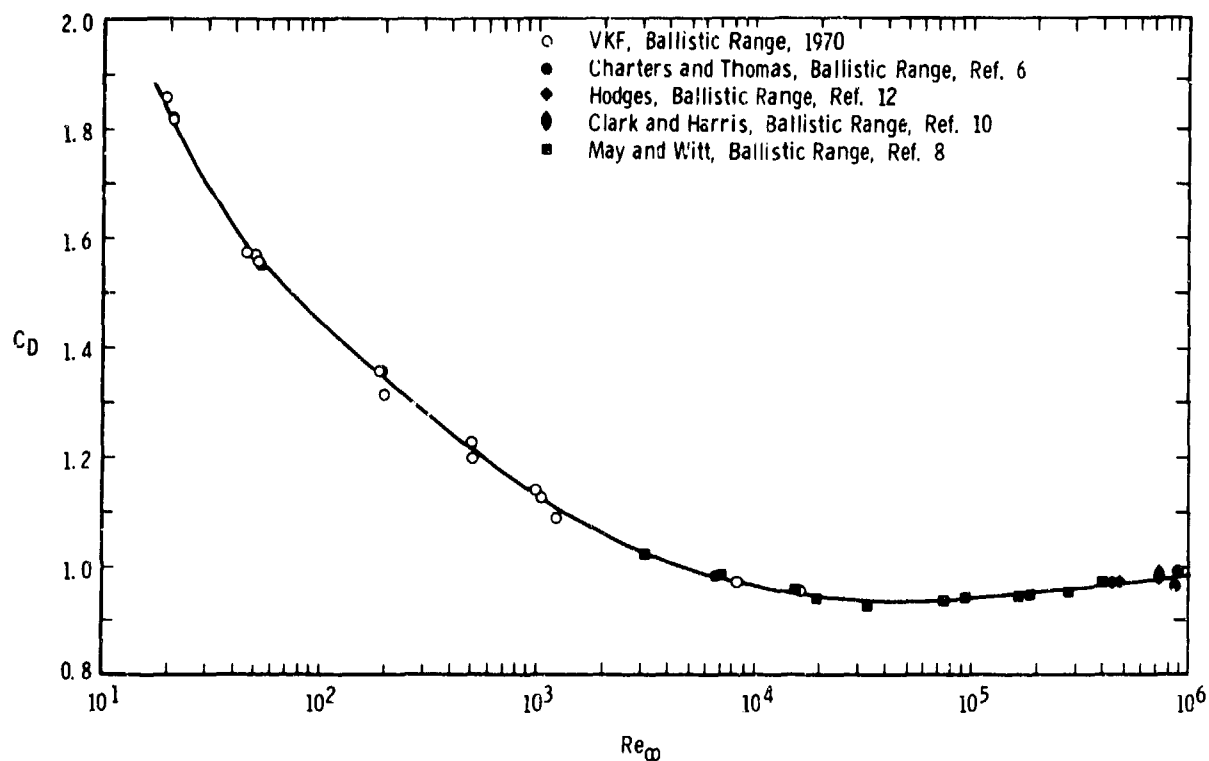
r. $2.4 \leqslant M_\infty \leqslant 2.7$
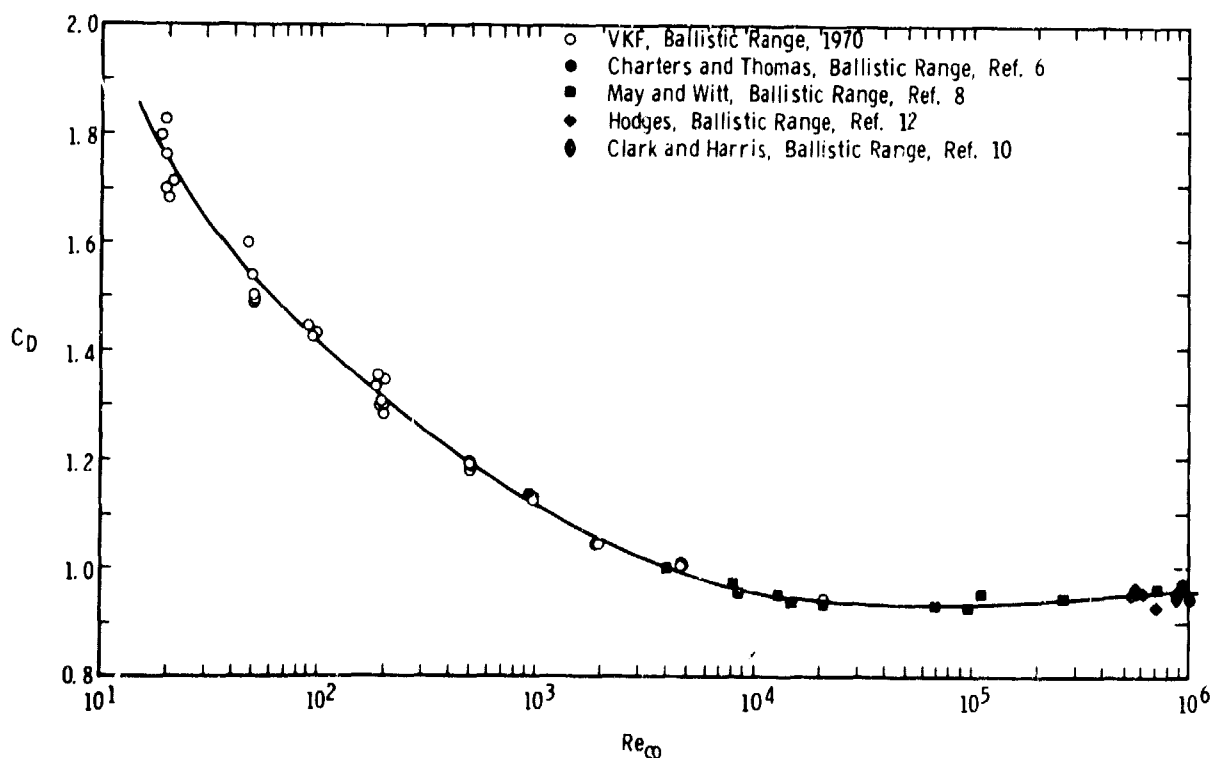
s. $2.8 \leqslant M_\infty \leqslant 3.2$

Fig. 6 Continued

43
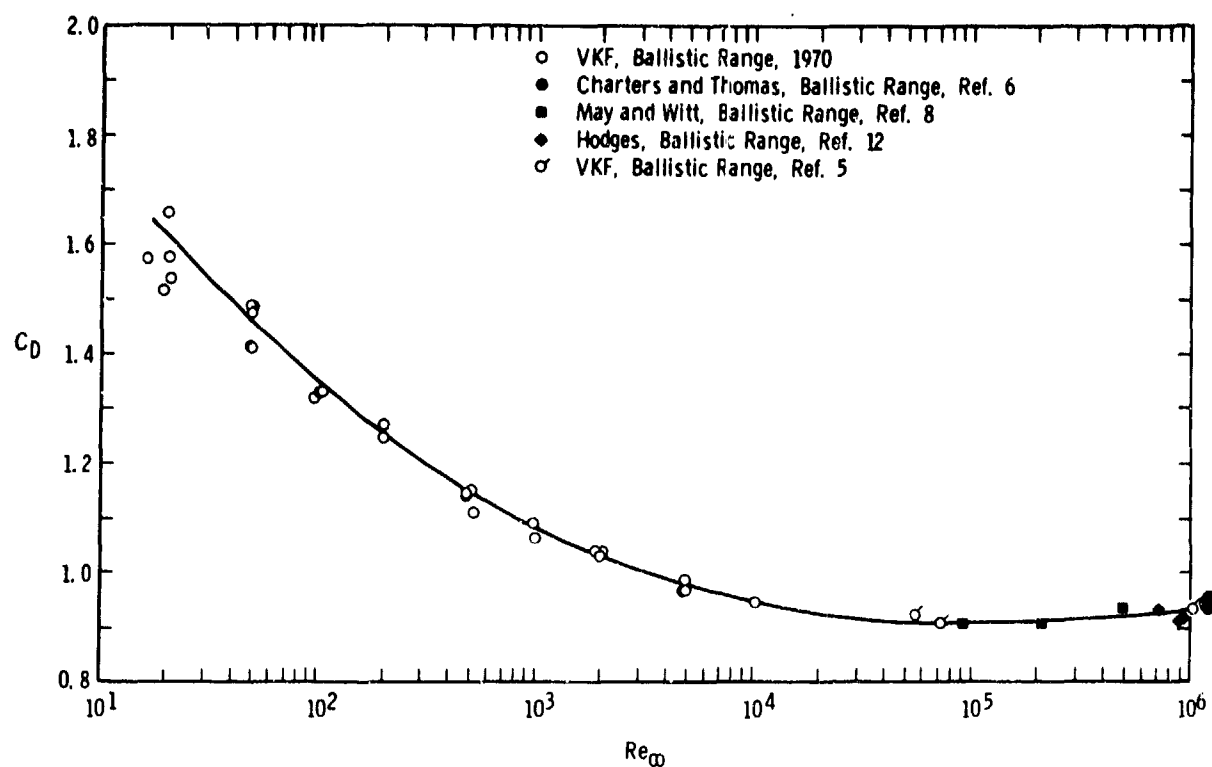
t. $3.8 \leqslant M_\infty \leqslant 4.2$
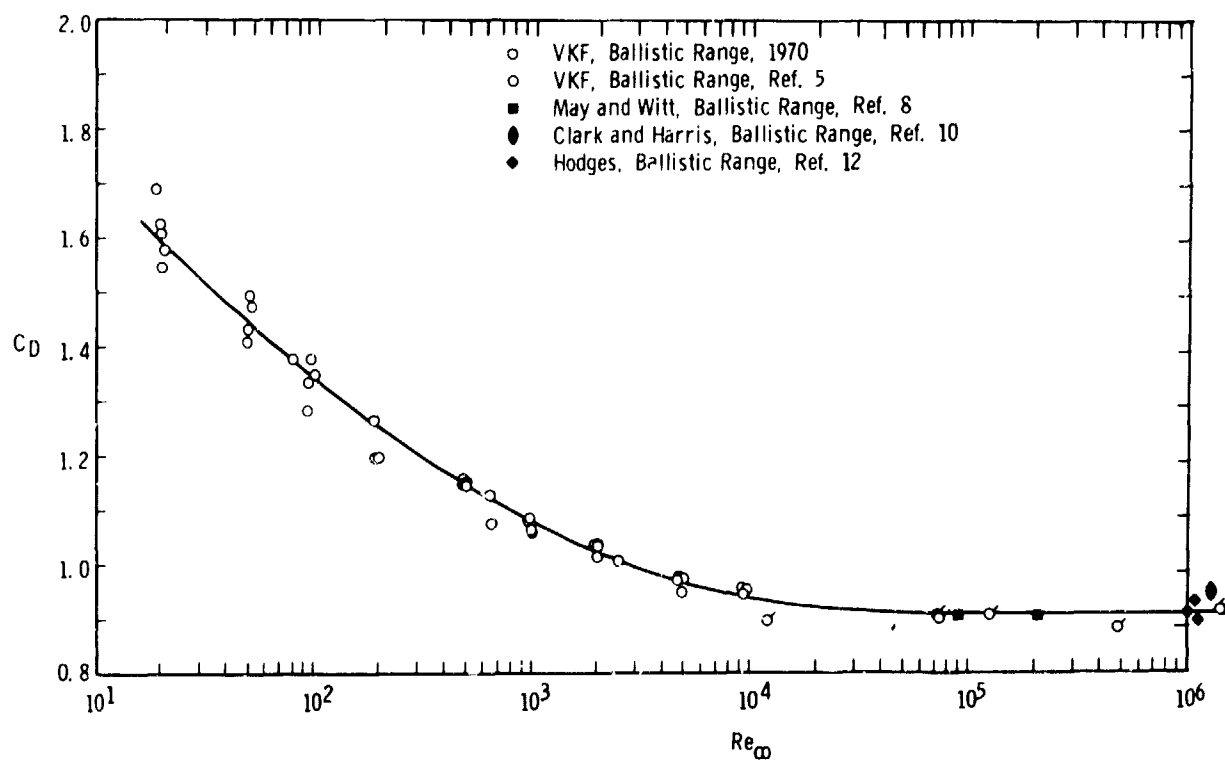
u. $4.8 \leqslant M_\infty \leqslant 5.2$

Fig. 6 Continued
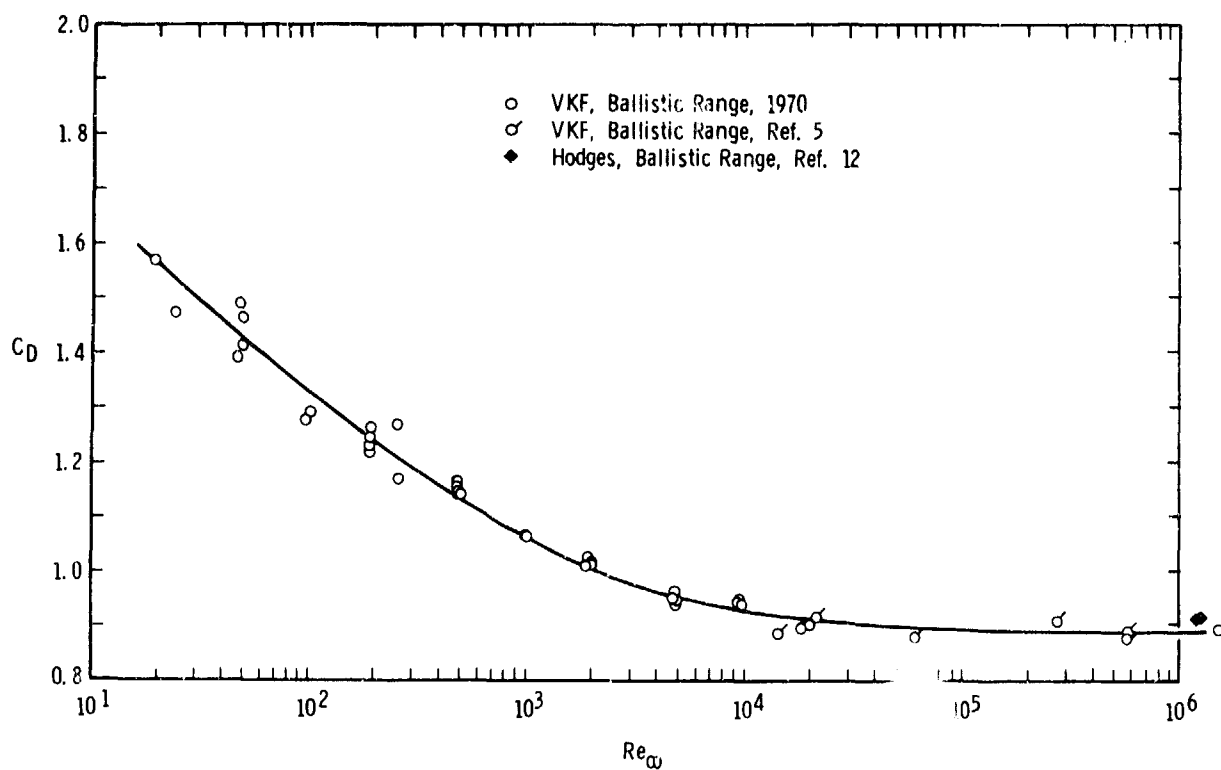
v. $5.8 \leqslant M_\infty \leqslant 6.2$

Fig. 6 Concluded
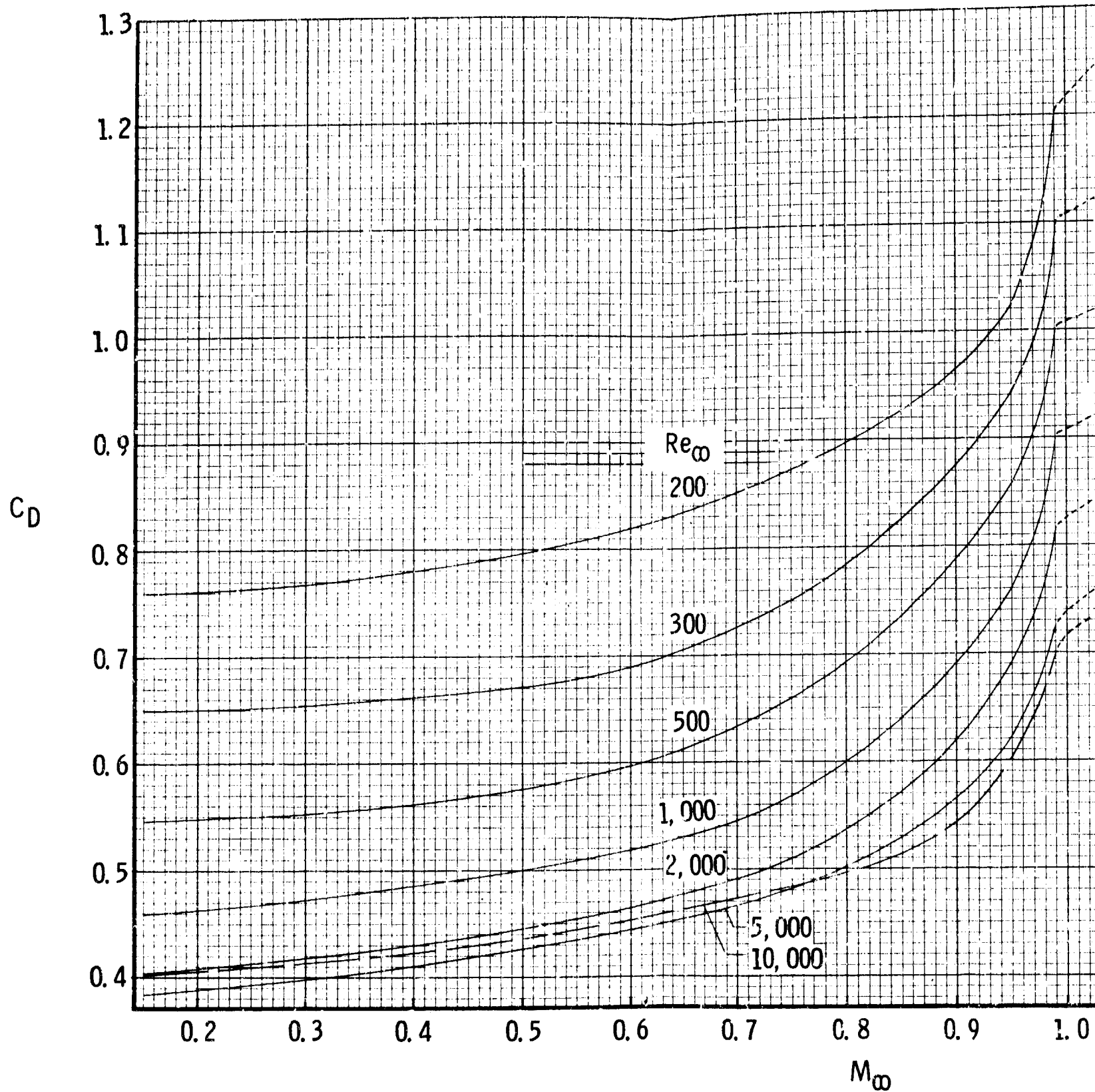
a. $0.2 \leqslant M_{\infty} \leqslant 1.9$

Fig. 7 Variation of Sphere Drag Coefficient with Mach Num
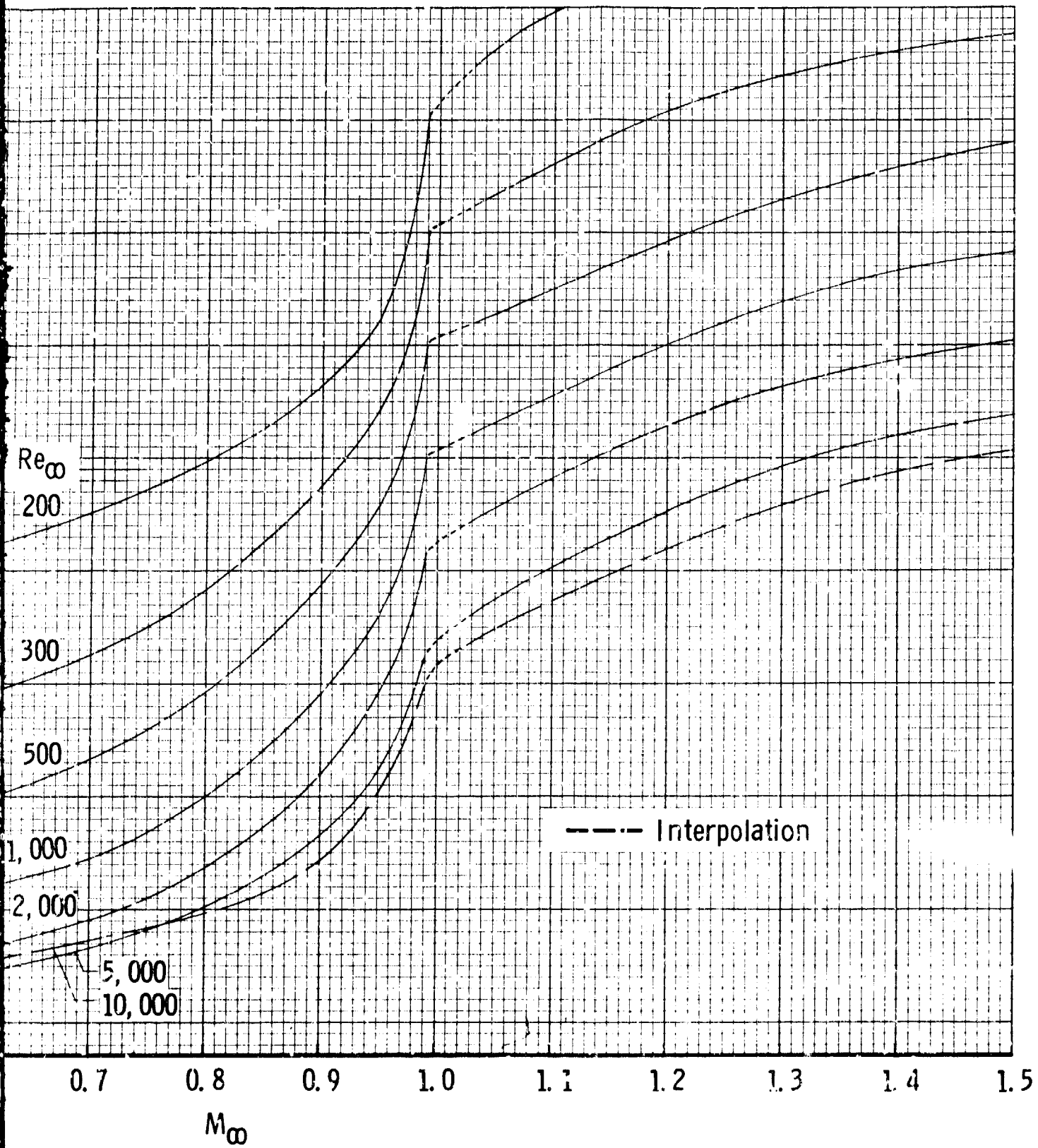
a. $0.2 \leqslant M_\infty \leqslant 1.9$

iation of Sphere Drag Coefficient with Mach Number

C_D

M_∞

b. $0.2 \leqslant M_\infty$
Fig. 7 Contin

48

Re_∞

10^6

5×10^5

10^5

5×10^4

2×10^4

10^4

— — — Interpolation

M_∞
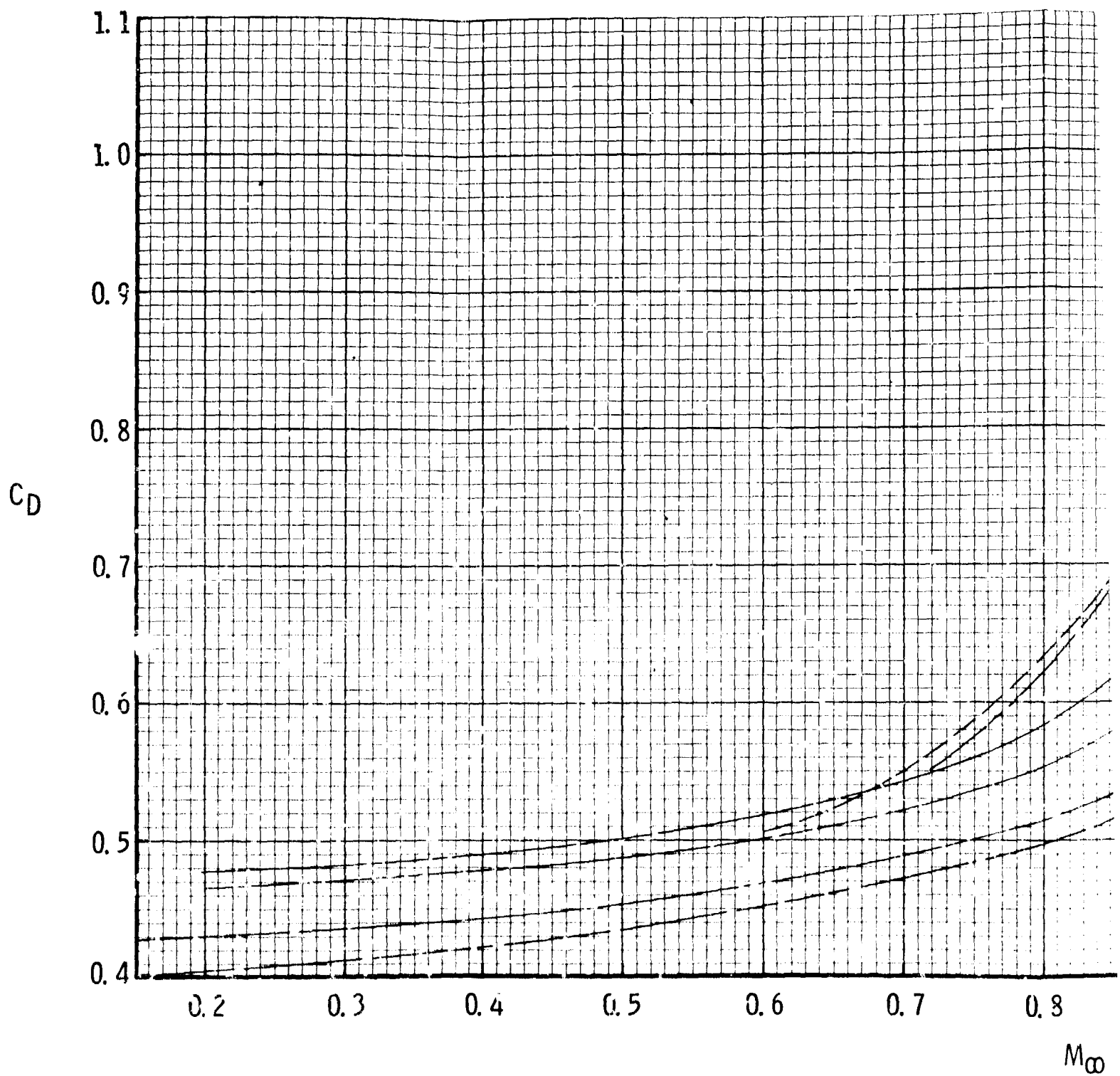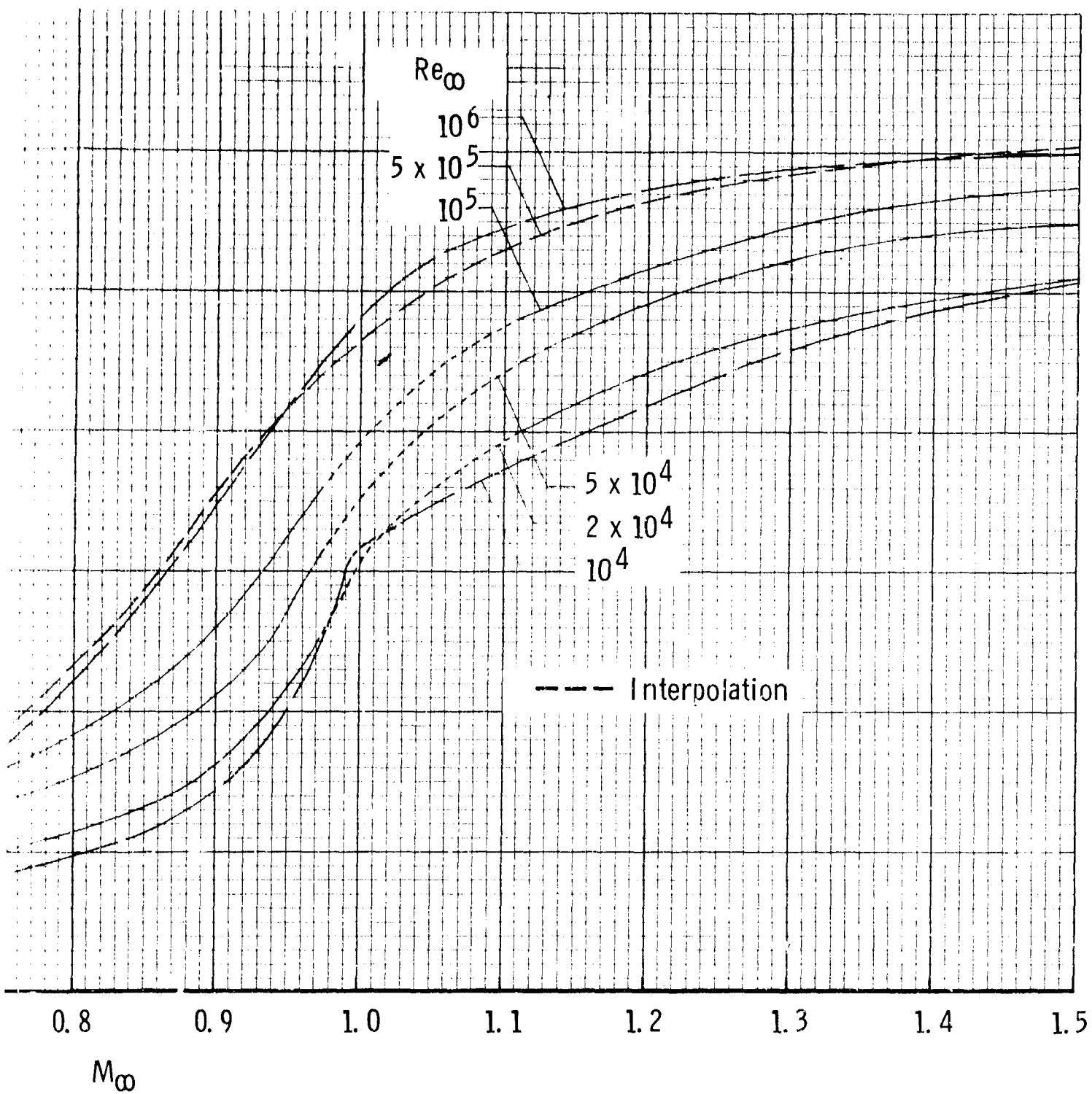
b. $0.2 \leqslant M_\infty \leqslant 1.5$
Fig. 7 Continued

c. $1.0 \leqslant M_\infty \leqslant 6.0$
Fig. 7 Continued

c. $1.0 \leqslant M_\infty \leqslant 6.0$
Fig. 7 Continued

49

--- Extrapolation

C_D

2.6 2.5 2.4 2.3 2.2 2.1 2.0 1.9 1.8

d. $1.0 \leqslant M_\infty \leqslant 6.0$
Fig. 7 Continued

C_D

1. 1

1. 0

0. 9

0. 8

0. 7

1. 0

2. 0

Re_∞

10^6

10^5

5×10^4

2×10^4
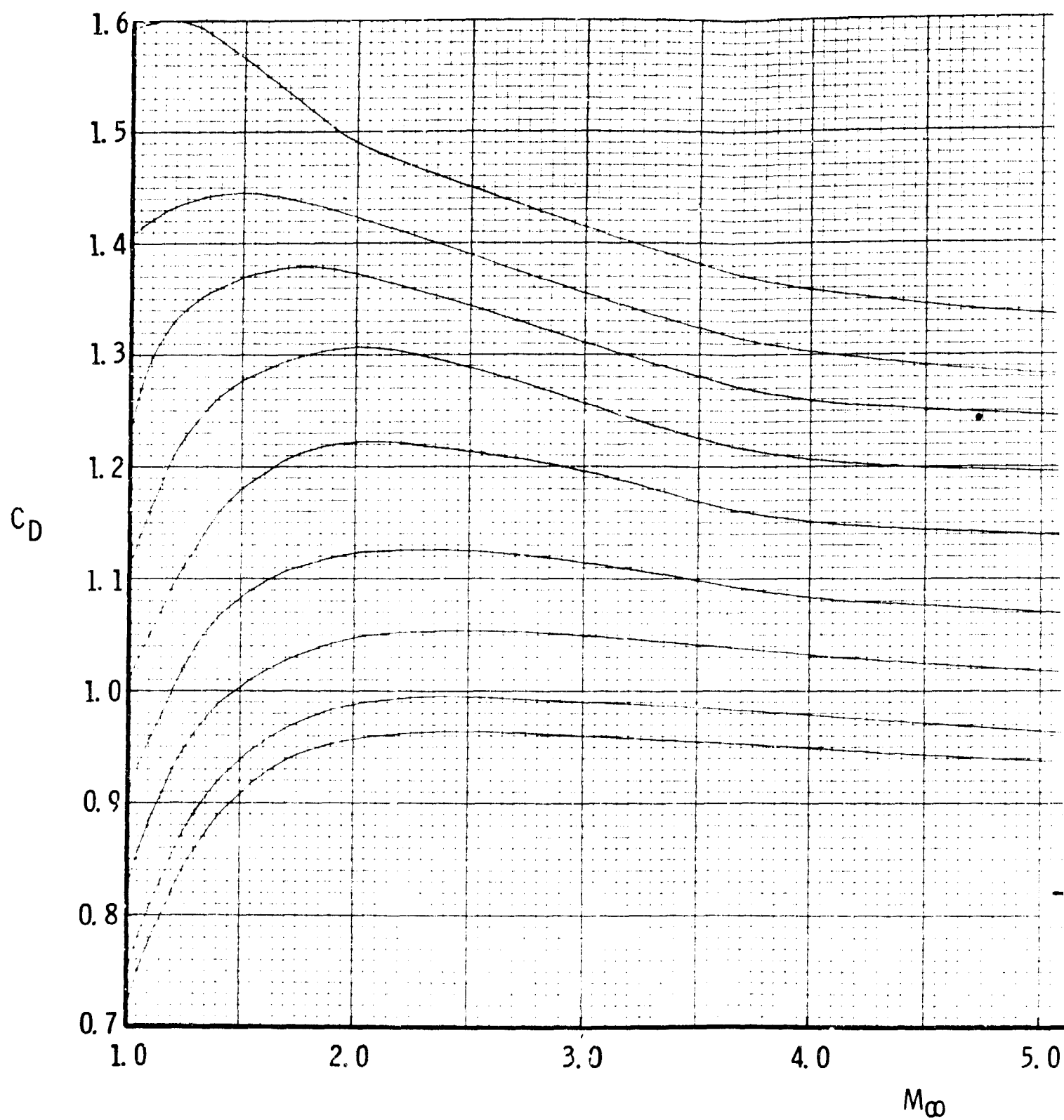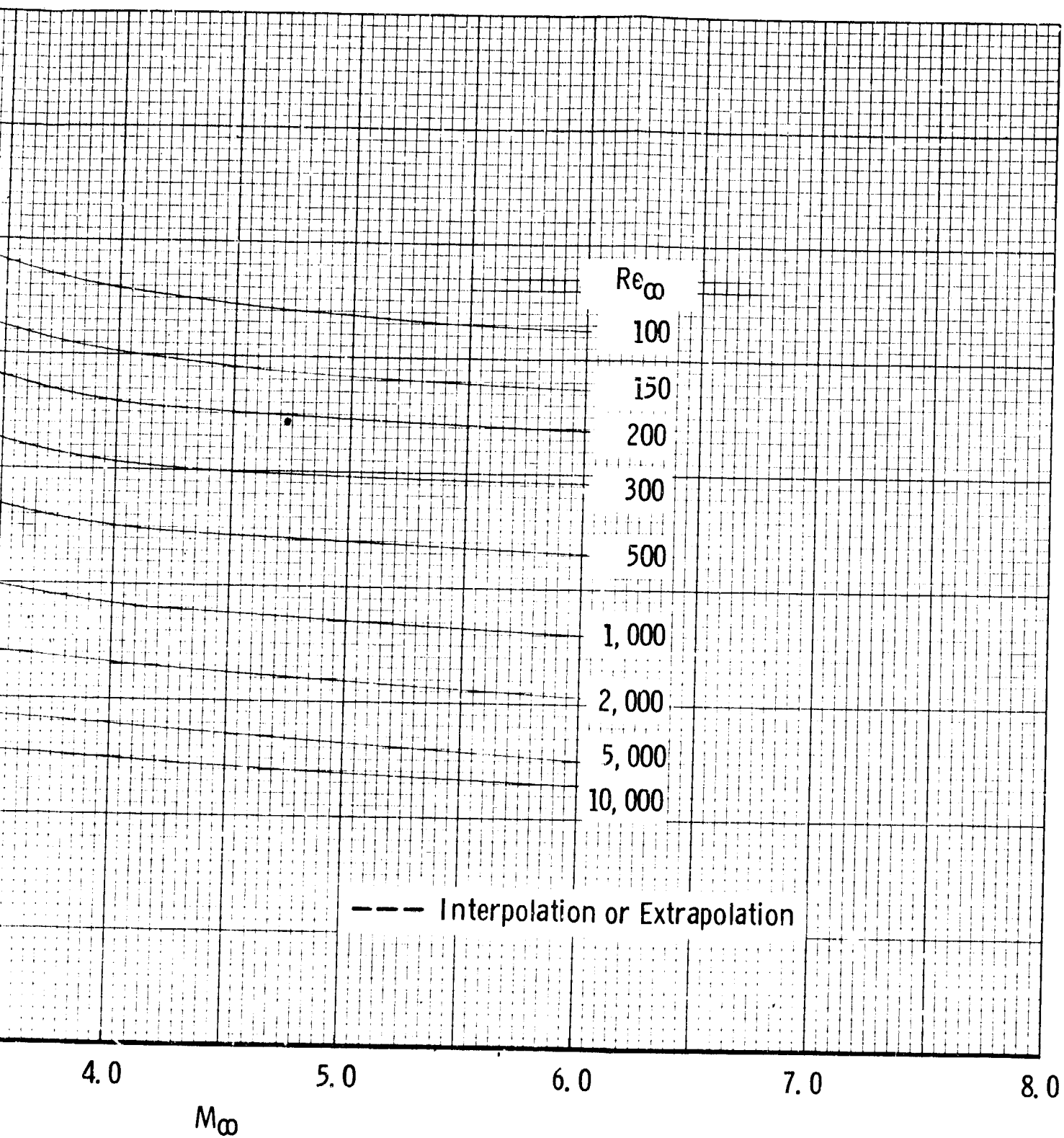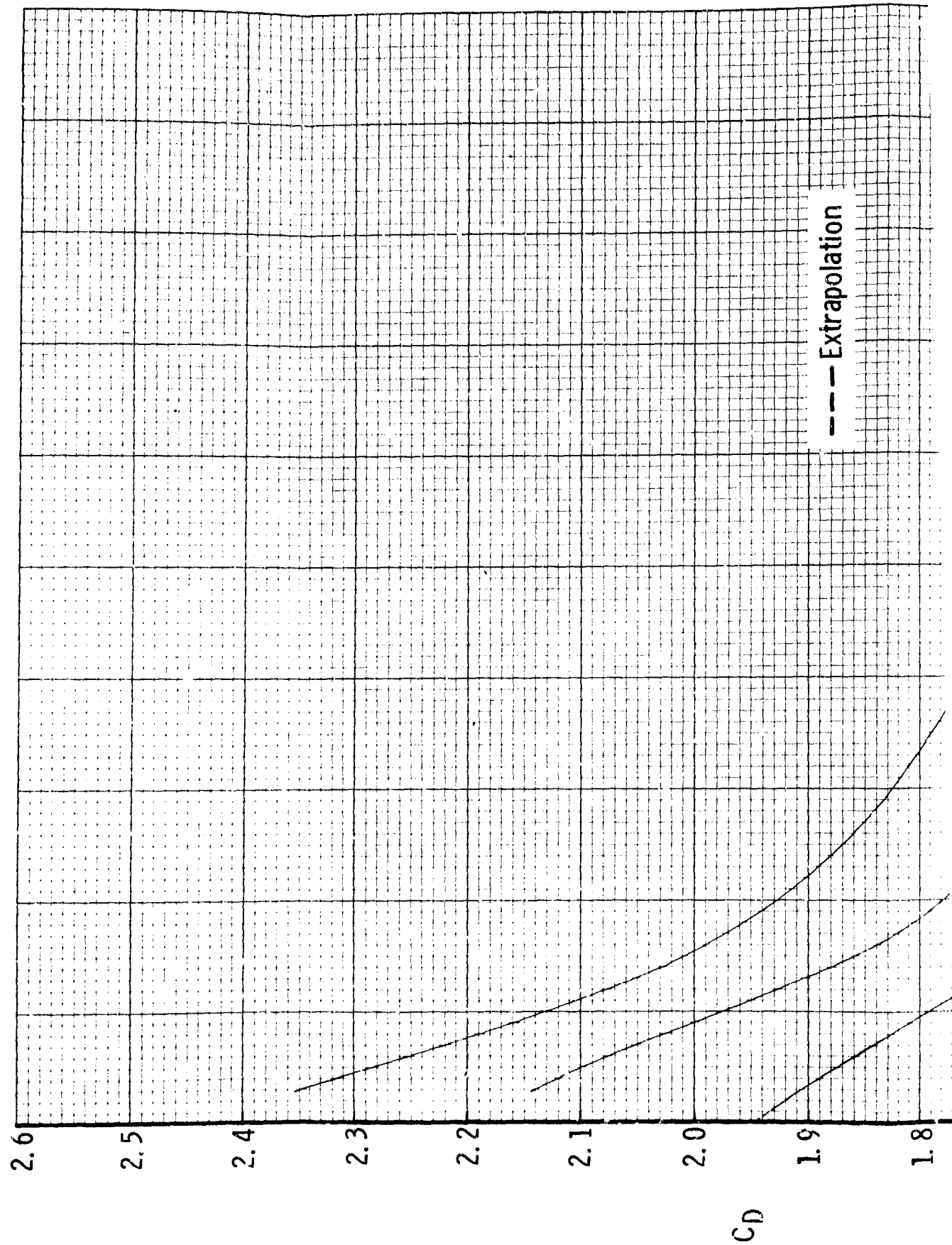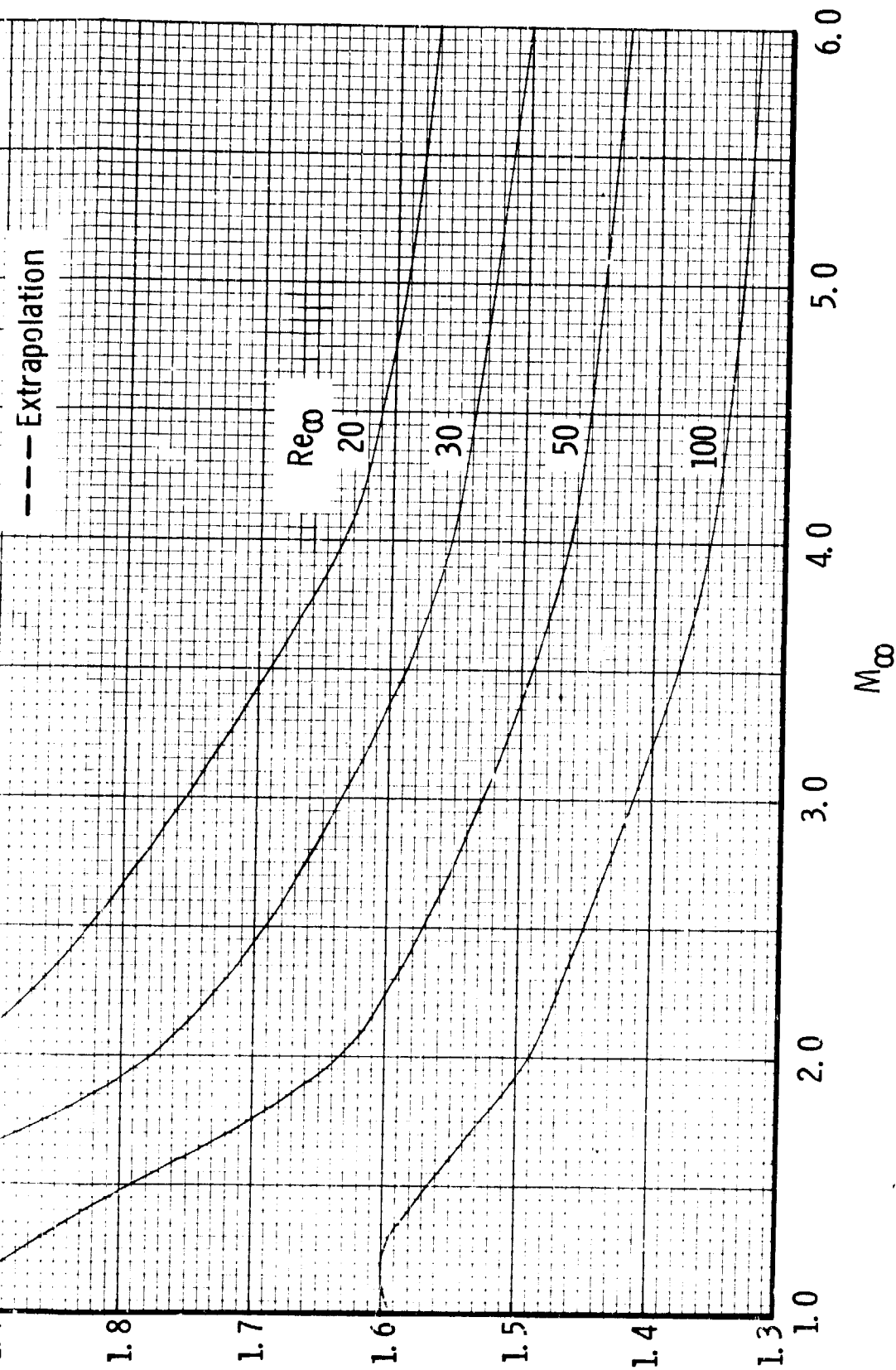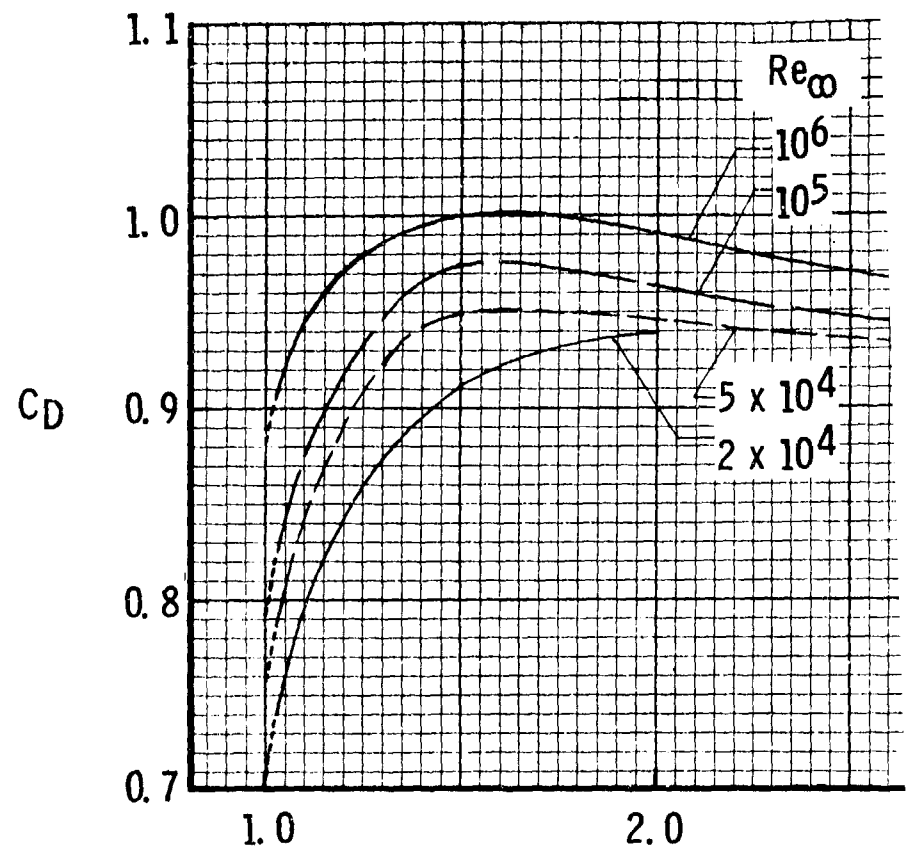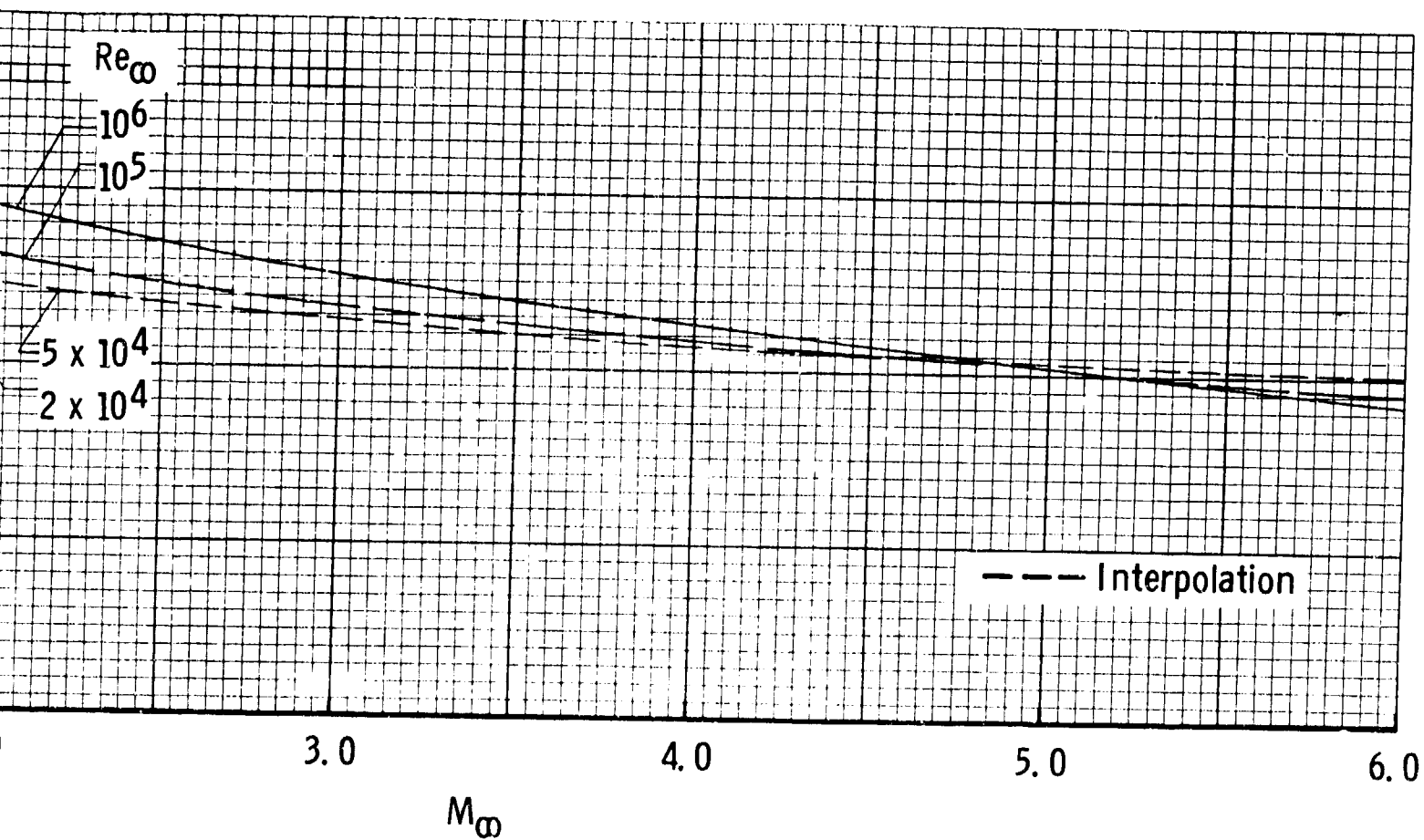
e. $1.0 \leqslant M_{\infty} \leqslant 6.0$
Fig. 7 Concluded
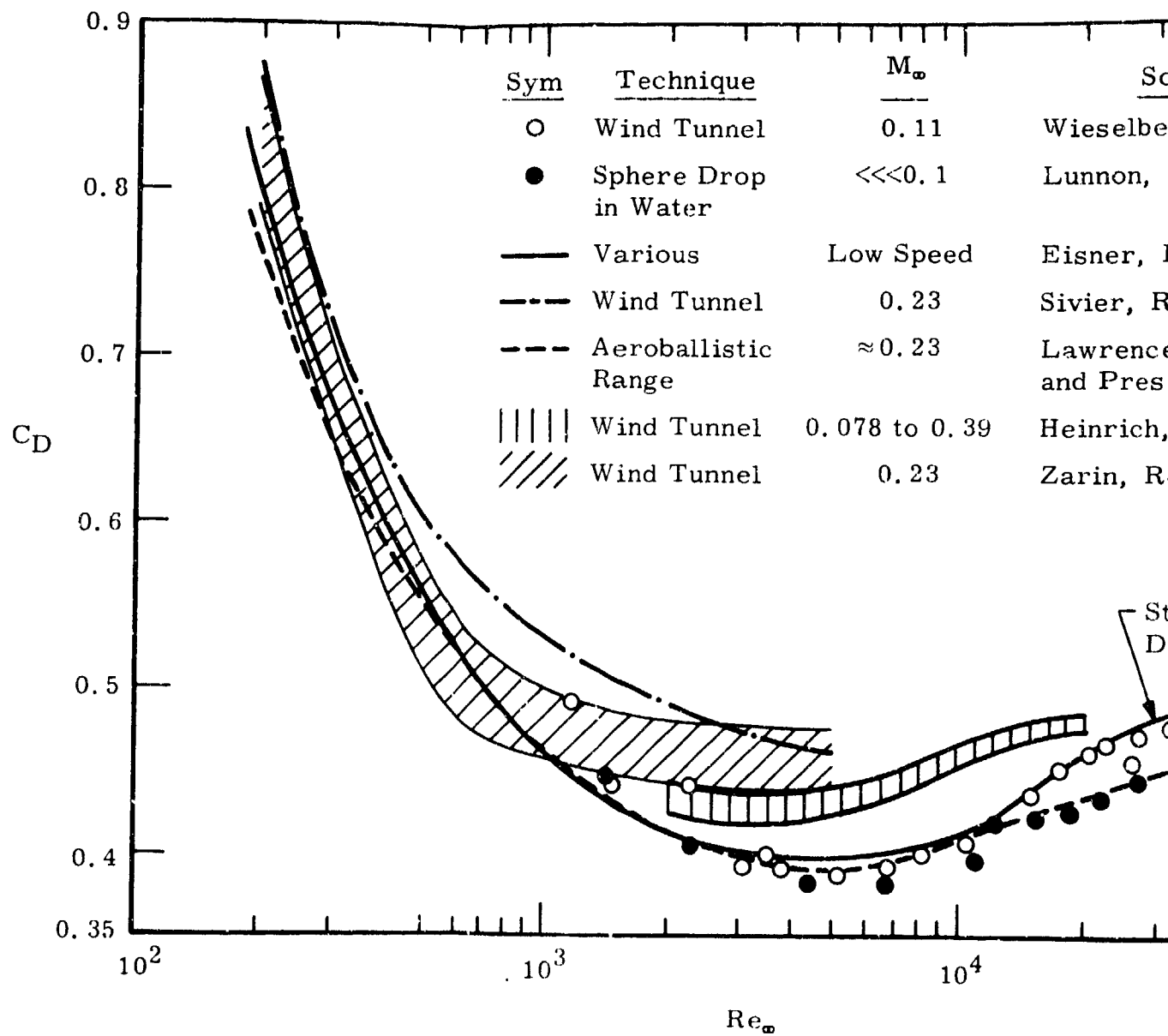
Fig. 8 Comparison of Sphere Drag Measurements at Low Speeds

Source
ieselberger, Ref. 14
unnon, Ref. 15
isner, Ref. 13
vier, Ref. 17
awrence, Ref. 2
nd Present
einrich, Ref. 16
arin, Ref. 18

Standard
Drag Curve

10^5
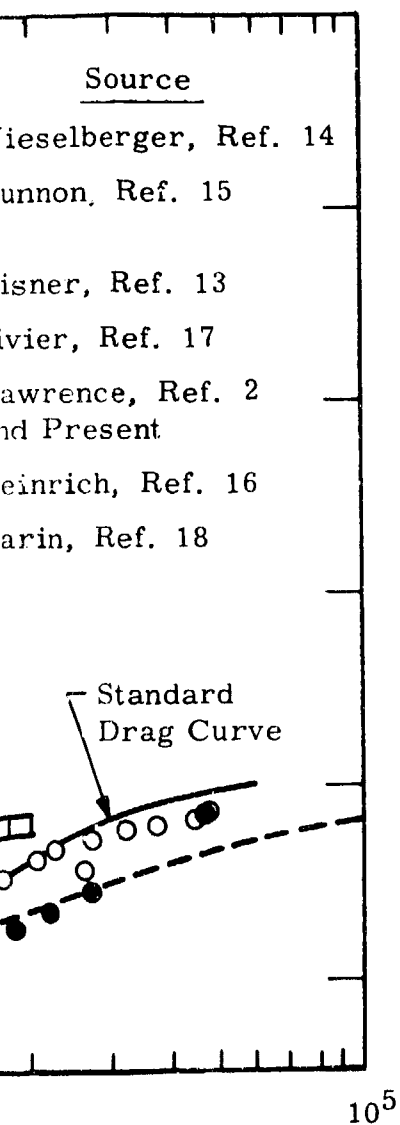
eeds
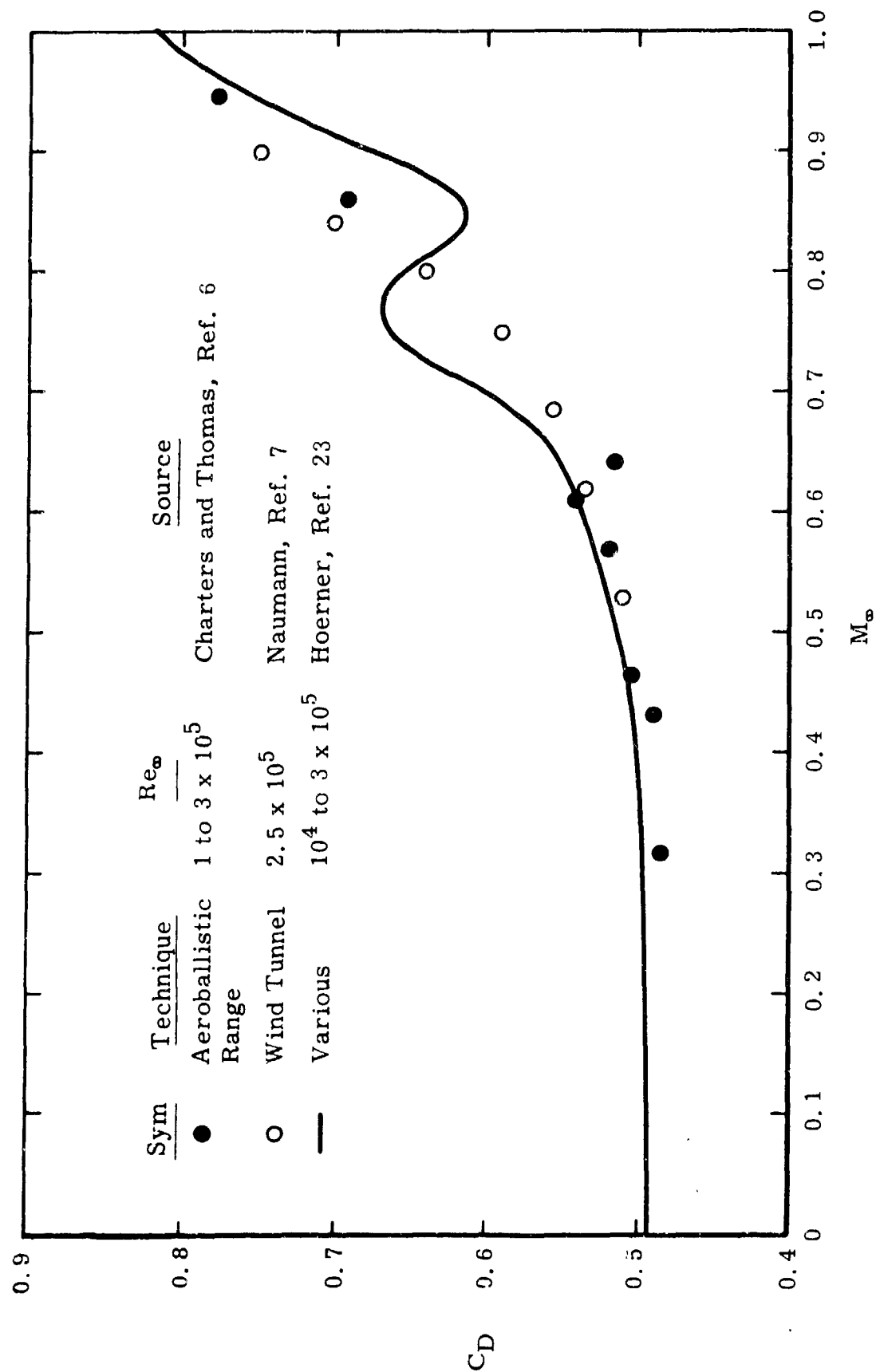
Fig. 9 Variation of Sphere Drag Coefficient with Mach Number (Pre-1970 Data)
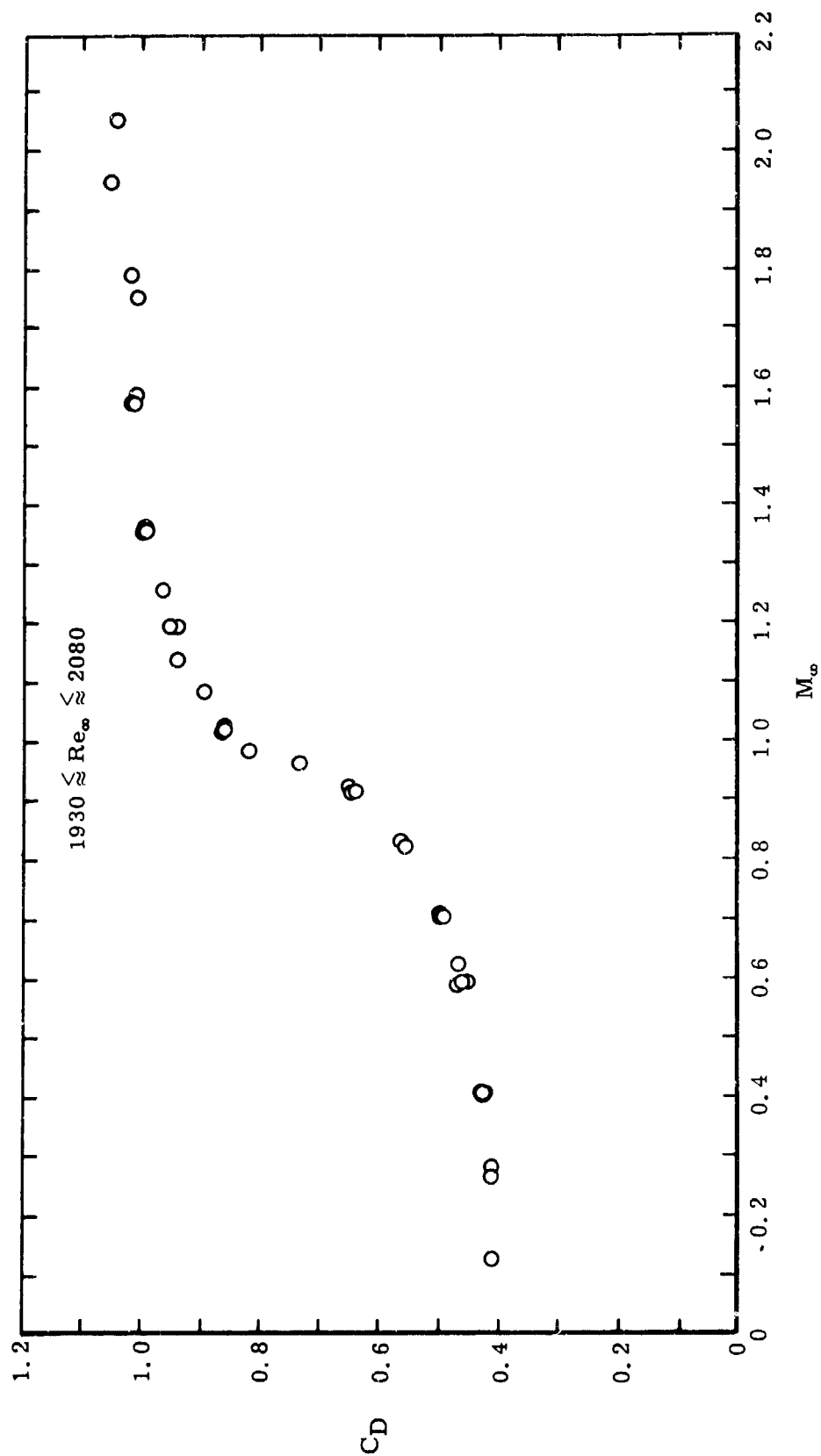
Fig. 10 Variation of Sphere Drag Coefficient with Mach Number (1970 Data)
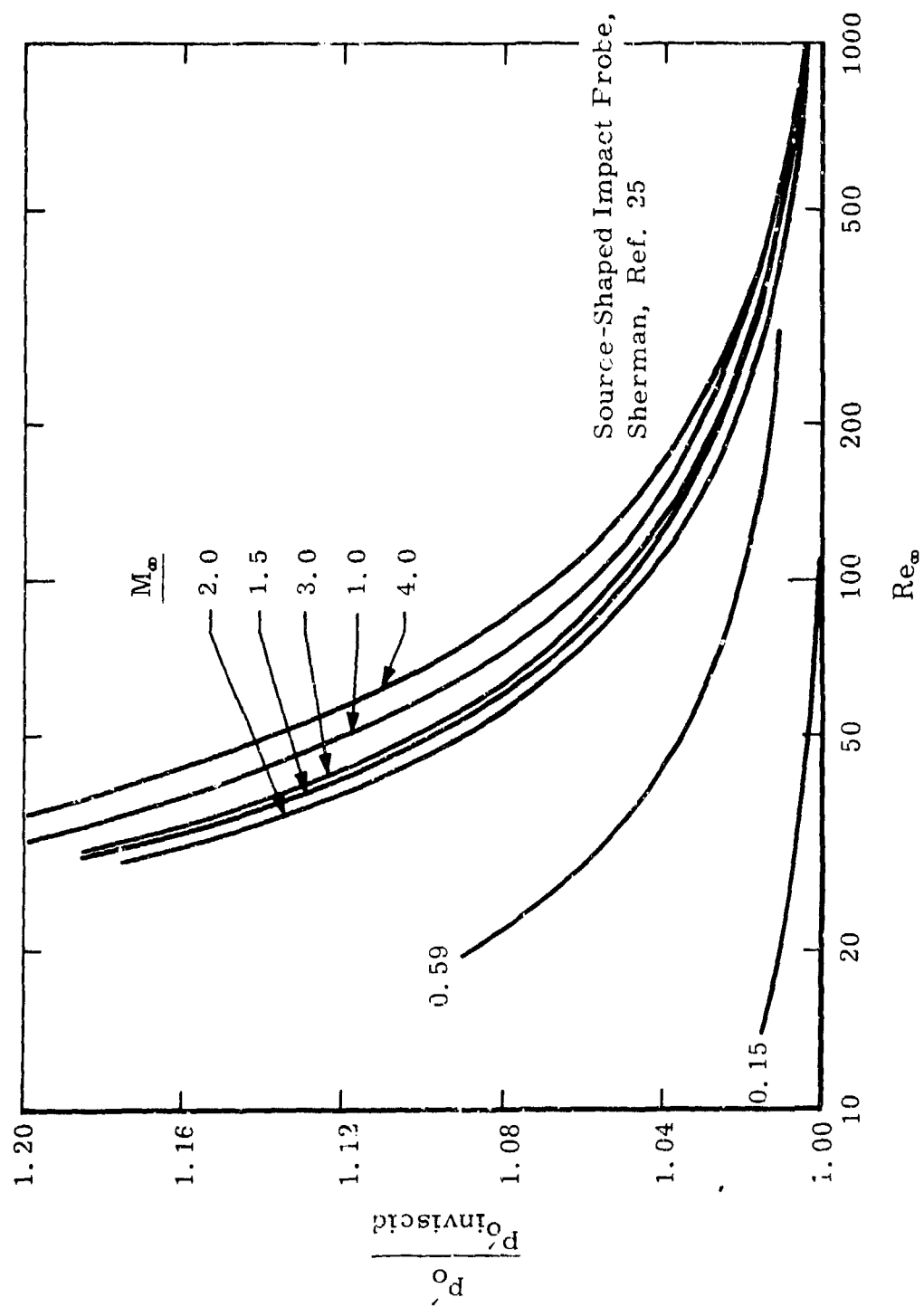
Fig. 11 Stagnation Point Pressure as a Function of Mach Number and Reynolds Number
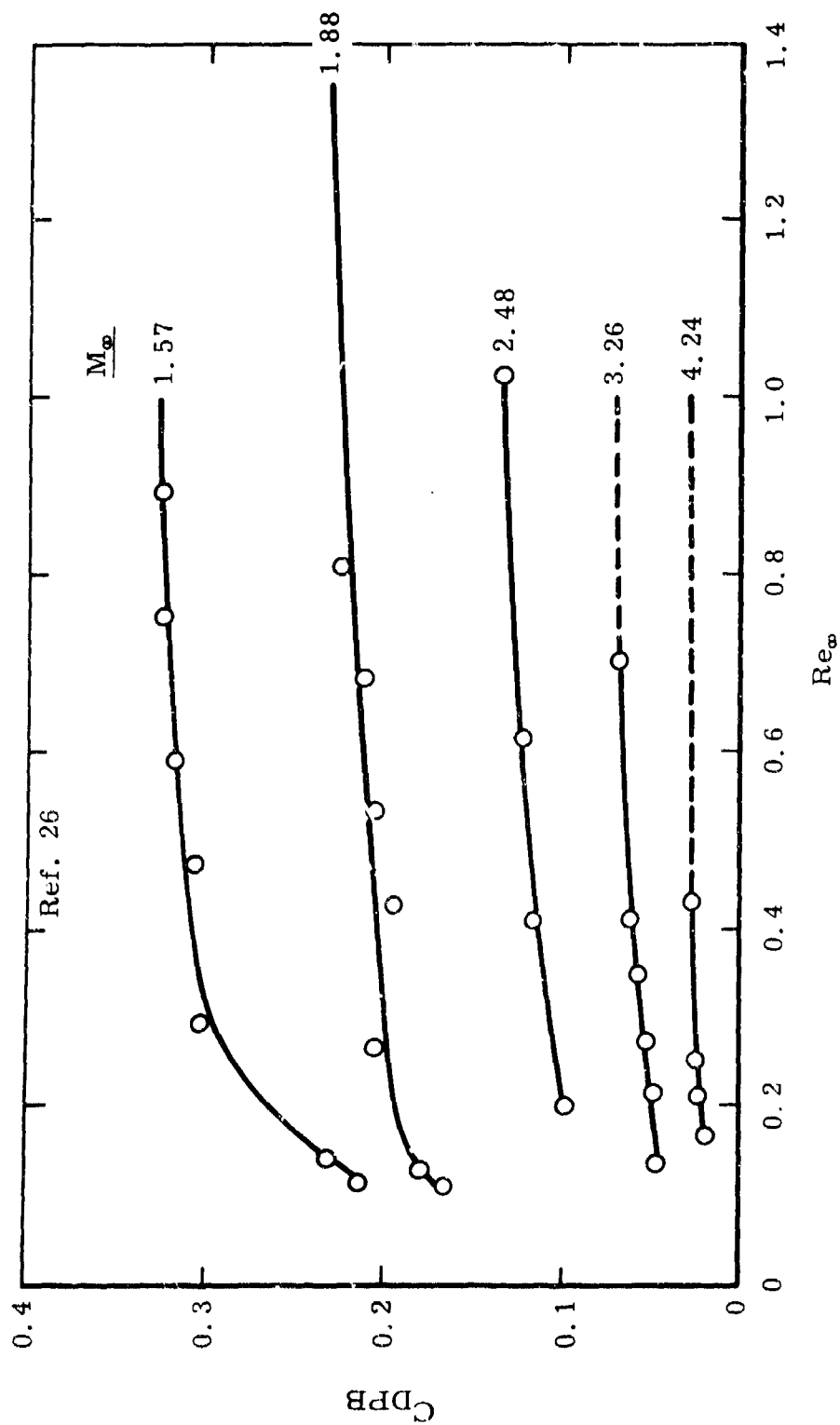
Fig. 12 Variation of Afterbody Pressure Drag with Reynolds Number for a Sphere
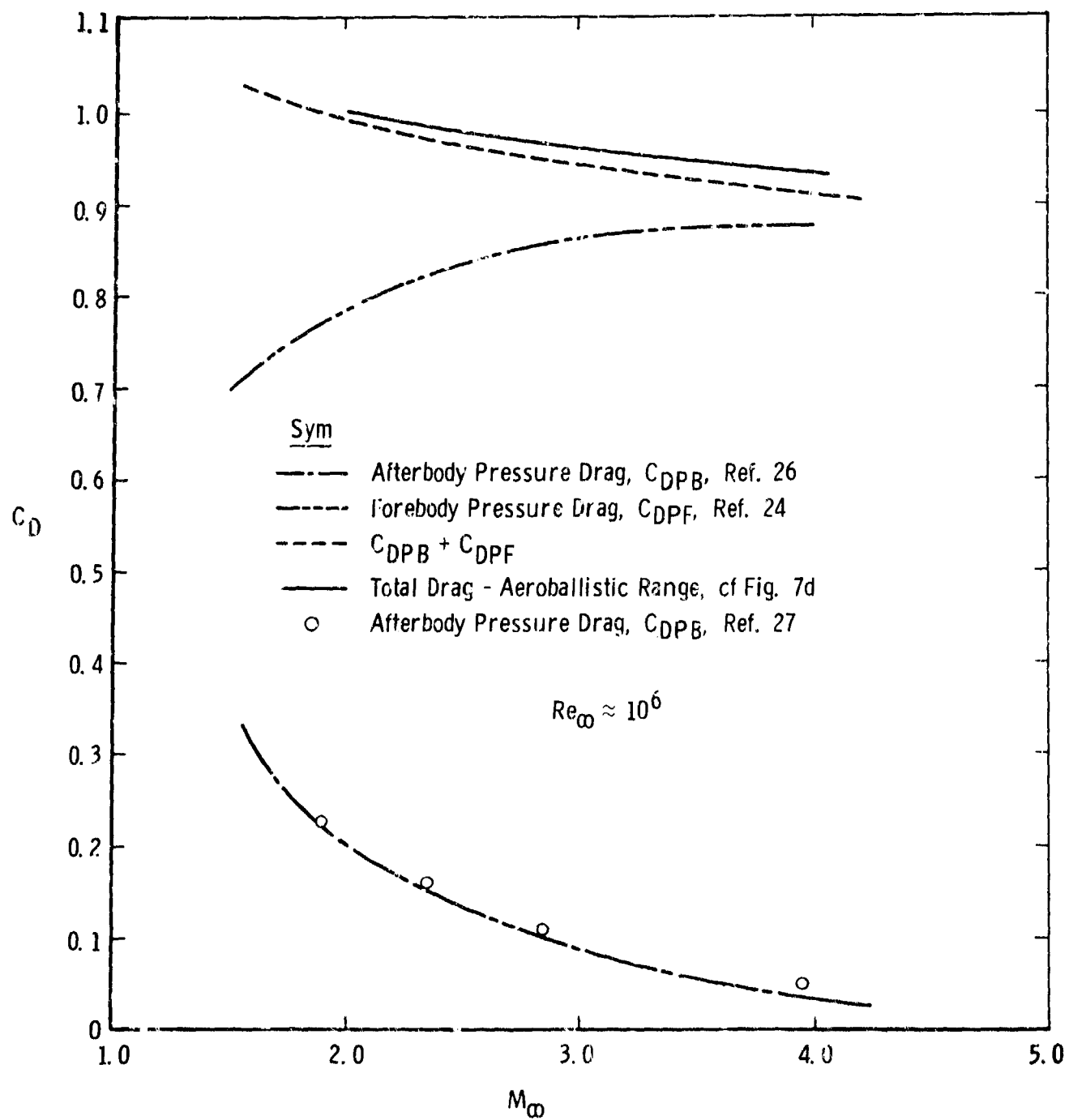
Fig. 13 Total Drag as a Function of Mach Number

Sym

— · — Afterbody Pressure Drag, C_{DPB}, Ref. 26

— · — Forebody Pressure Drag, C_{DPF}, Ref. 24

— — — $C_{DPB} + C_{DPF}$

——— Total Drag - Aeroballistic Range, cf Fig. 7d

○ Afterbody Pressure Drag, C_{DPB}, Ref. 27

$Re_\infty \approx 10^6$

57
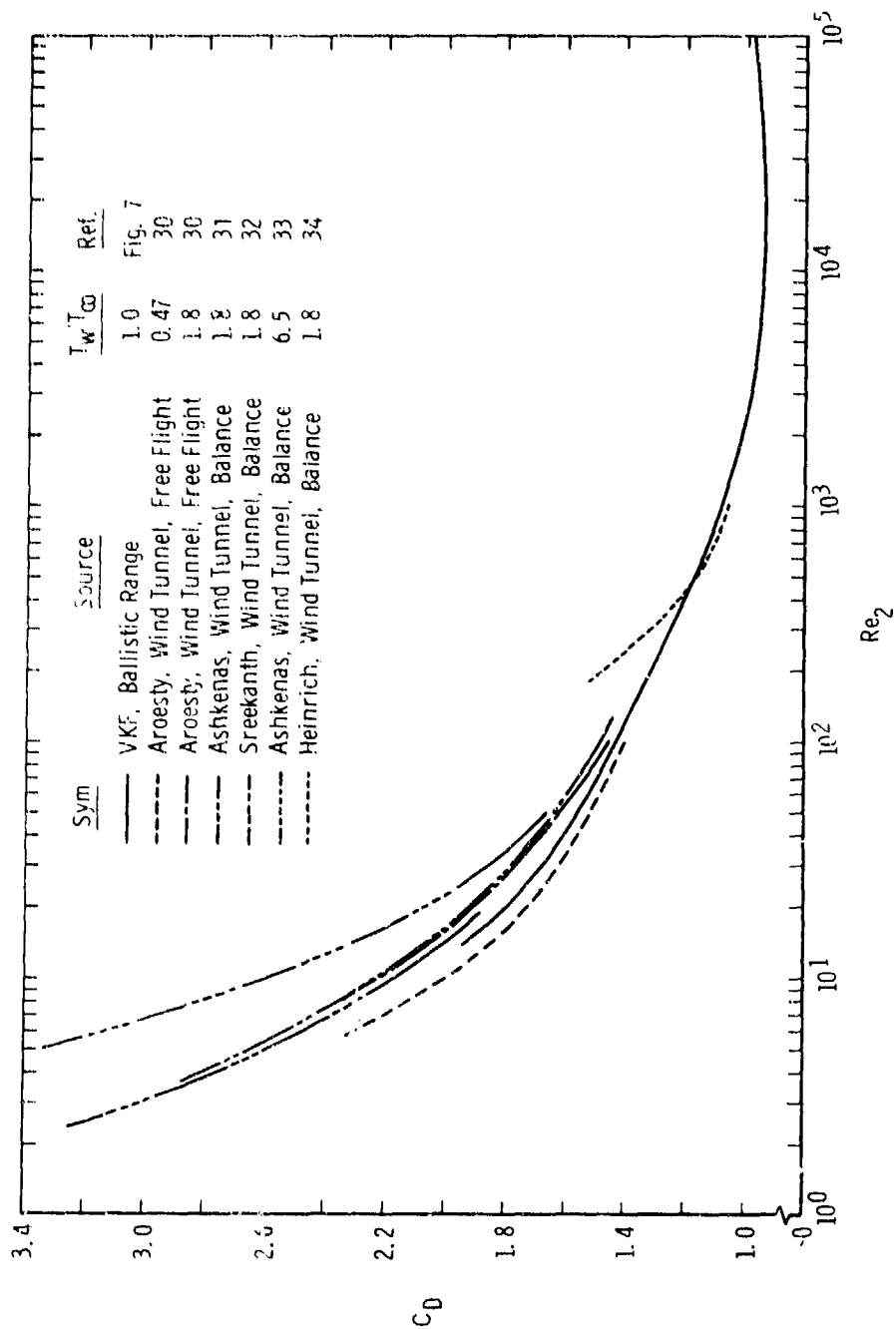
a. $M_\infty \approx 2.0$

Fig. 14 Variation of Sphere Drag Coefficient with Reynolds Number and Wall Temperature

Sym	Source	T_w/T_∞	Ref.
———	VKF, Ballistic Range	1.0	Fig. 7
———	Aroesty, Wind Tunnel, Free Flight	0.47	30
———	Aroesty, Wind Tunnel, Free Flight	1.8	30
———	Ashkenas, Wind Tunnel, Balance	1.8	31
———	Sreekanth, Wind Tunnel, Balance	1.8	32
———	Ashkenas, Wind Tunnel, Balance	6.5	33
———	Heinrich, Wind Tunnel, Balance	1.8	34

58
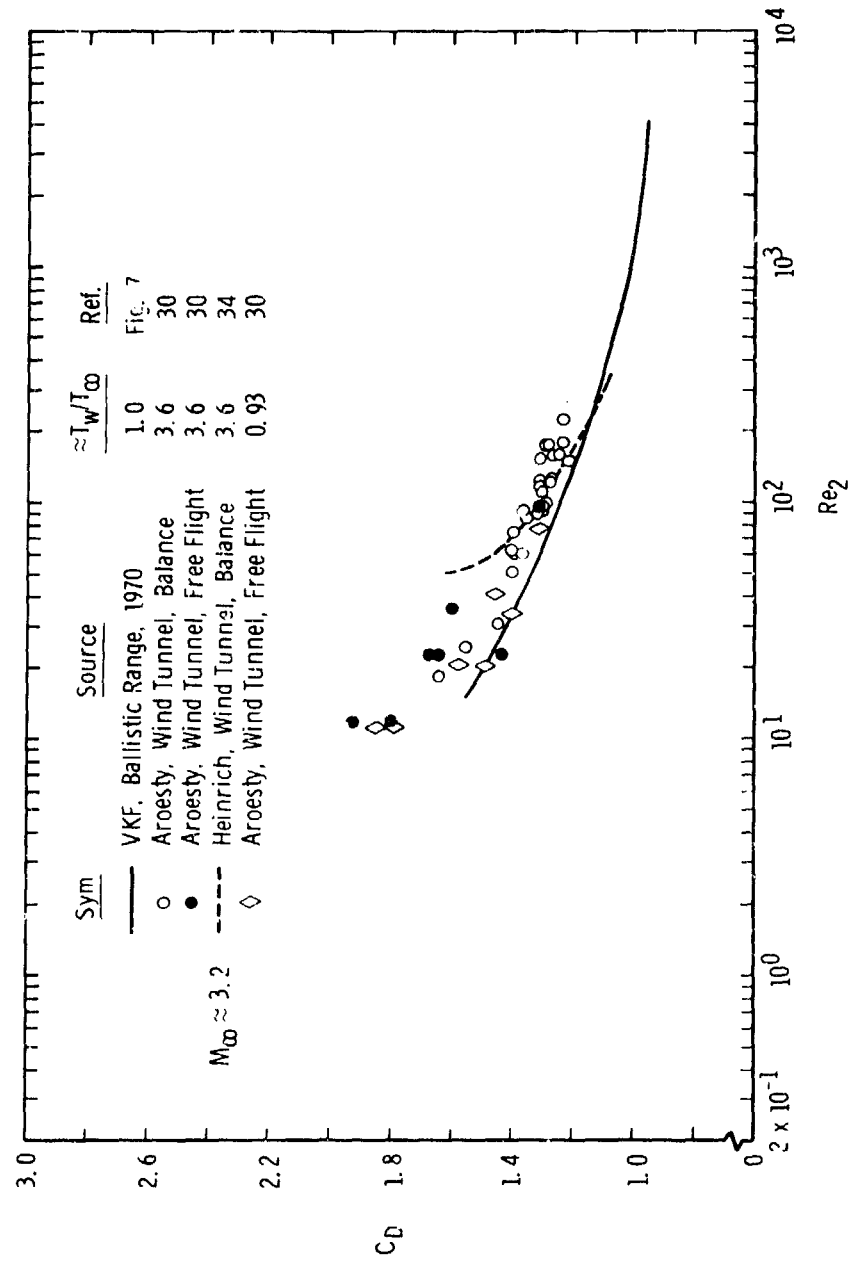
b. $3.4 \leqslant M_{\infty} \leqslant 3.6$
Fig. 14 Continued

59
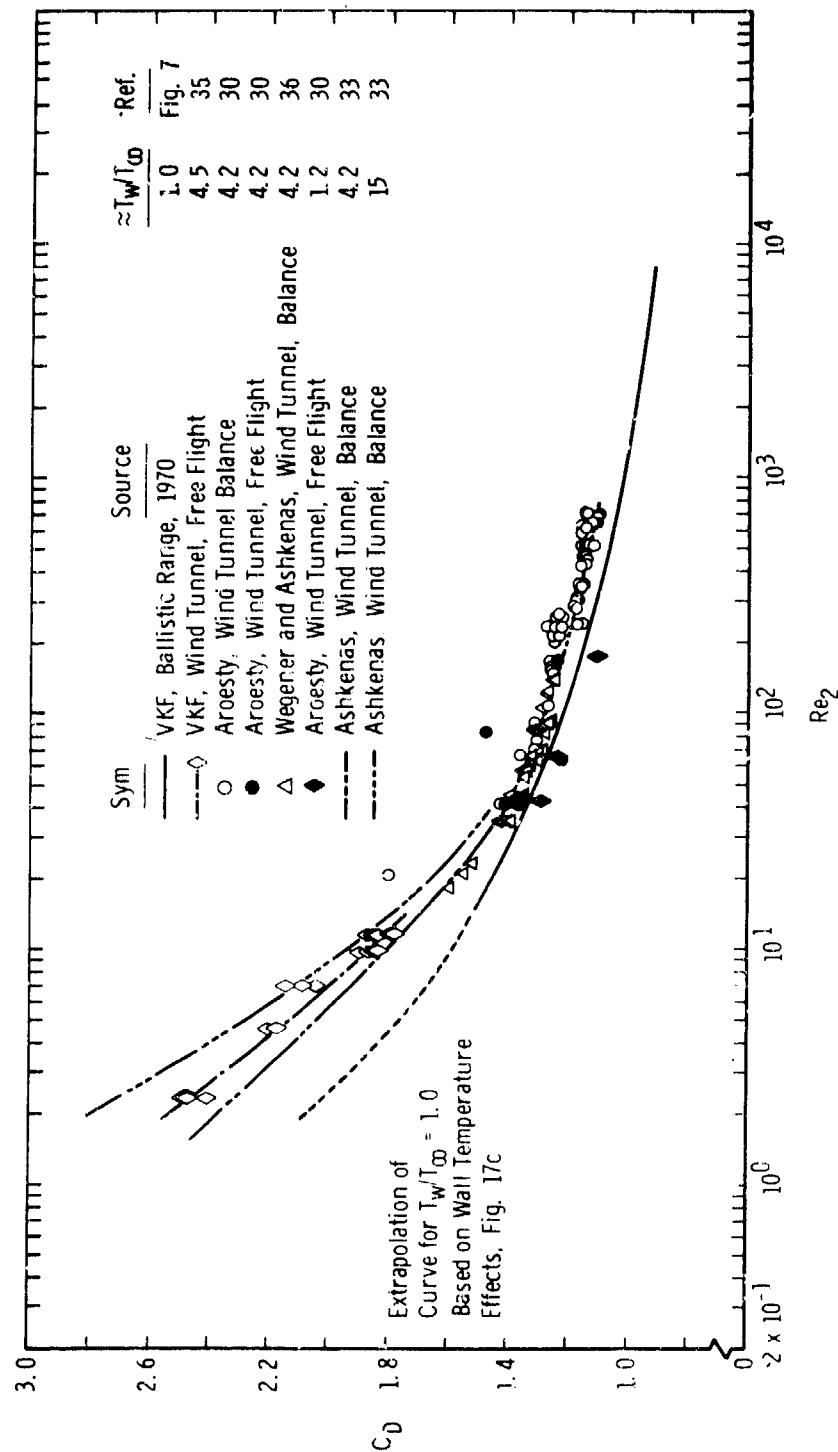
c. $4.0 \leqslant M_\infty \leqslant 4.2$

Fig. 14 Continued

60
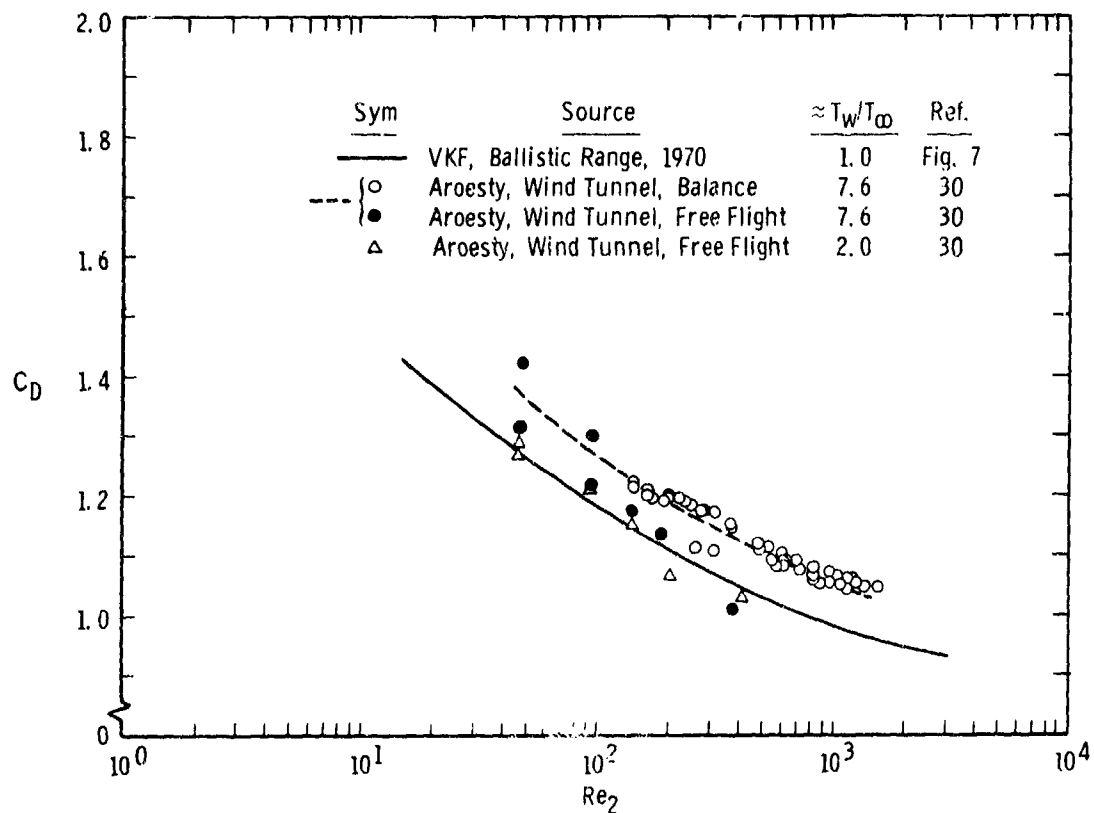
d. $5.8 \leqslant M_\infty \leqslant 6.1$

e. $M_\infty \approx 7.35$

Fig. 14 Continued

61

Sym	Source	$\approx T_W/T_\infty$	Ref.
—·—	VKF, Ballistic Range, Interpolation	1.0	Fig. 16
--○--	VKF, L. D. M. Wind Tunnel, Free Flight	2.15	38
--●--	VKF, L. D. M. Wind Tunnel, Free Flight	4.0	38
--◆--	VKF, Wind Tunnel C, Balance	14.0	38
—·—	Phillips, Free Jet, Magnetic Balance	21.0	39
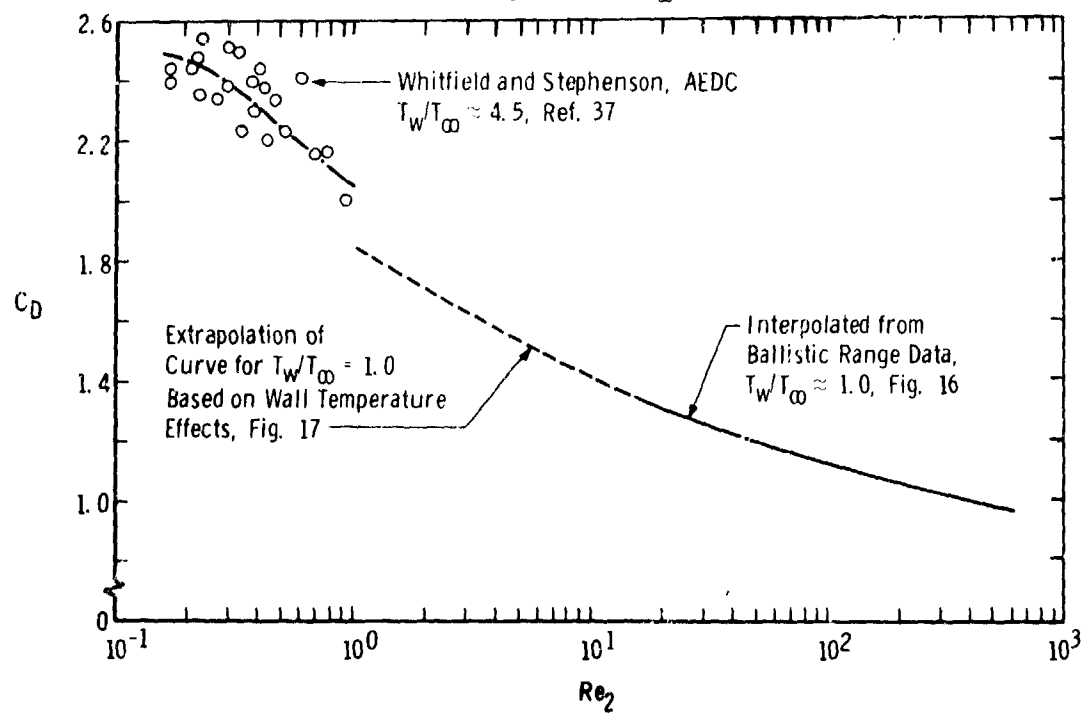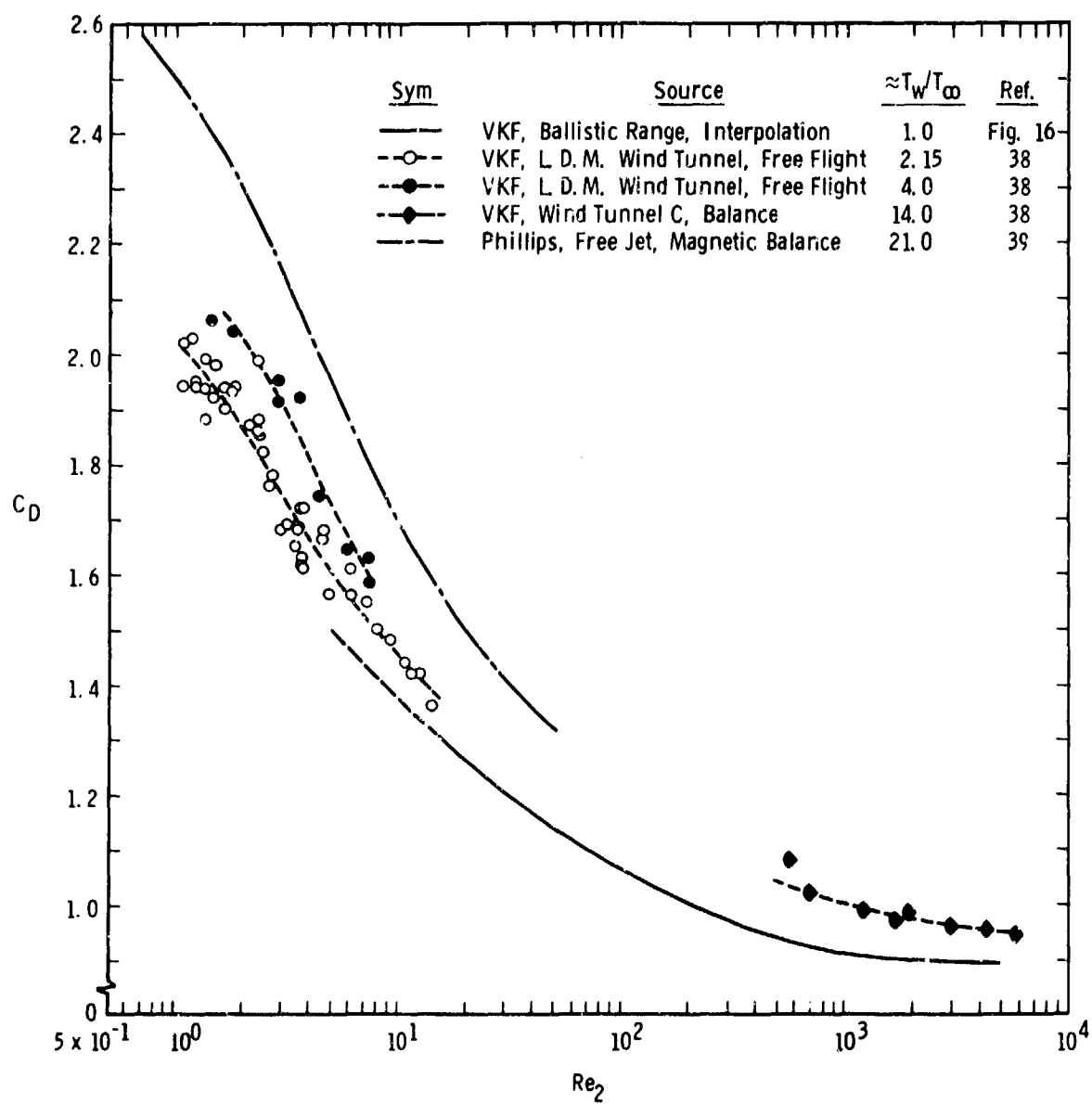
f. $10.0 \leqslant M_\infty \leqslant 10.8$

Fig. 14 Concluded

a. $8.3 \leqslant M_\infty \leqslant 10.0$

Fig. 15 Variation of Sphere Drag Coefficient with Reynolds Number at Hypersonic Speeds
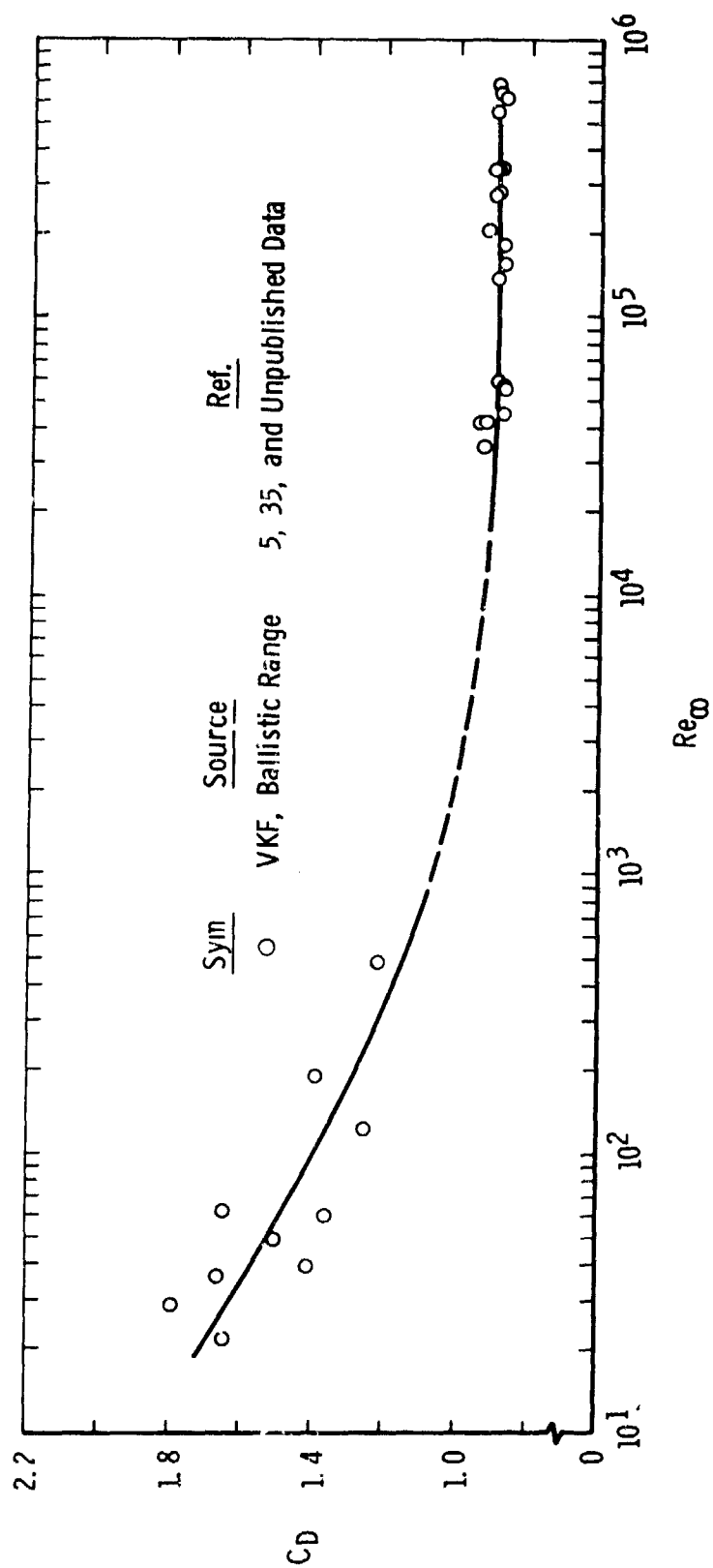
b. $13 \leqslant M_\infty \leqslant 14$
Fig. 15 Continued

64
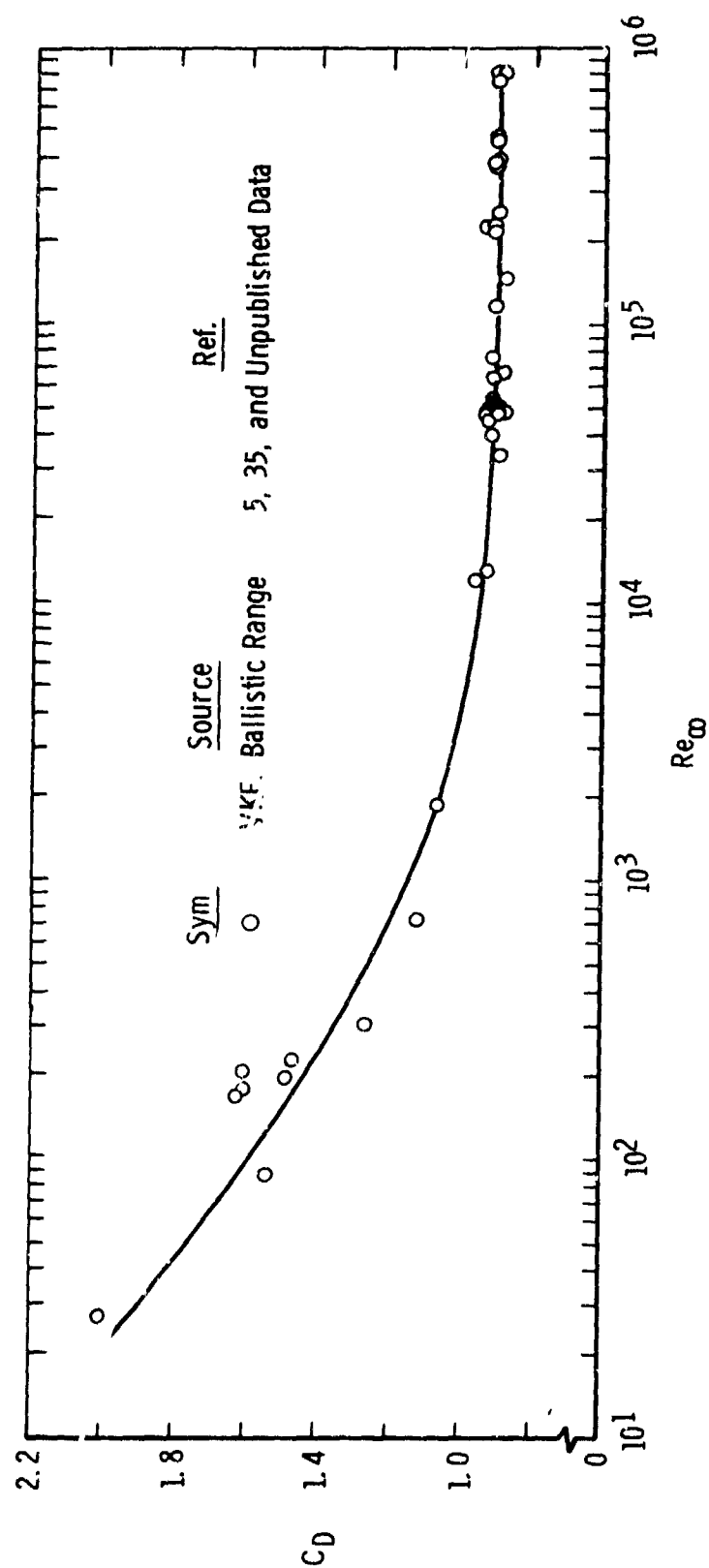
c. $16.5 \leqslant M_\infty \leqslant 21.5$
Fig. 15 Concluded
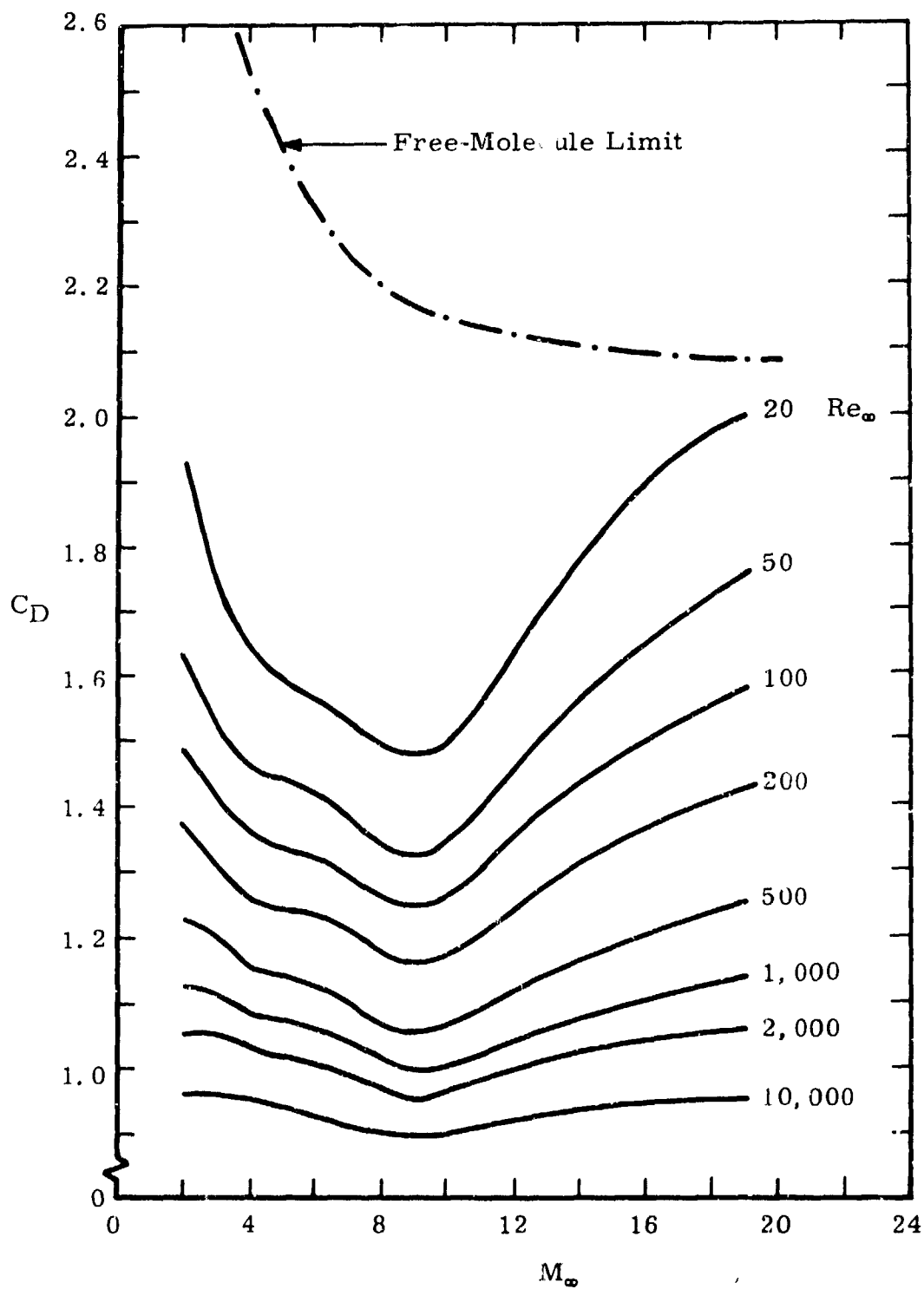
Fig. 16 Variation of Sphere Drag Coefficient with Mach Number at Hypersonic Speeds and $T_w/T_\infty \approx 1$
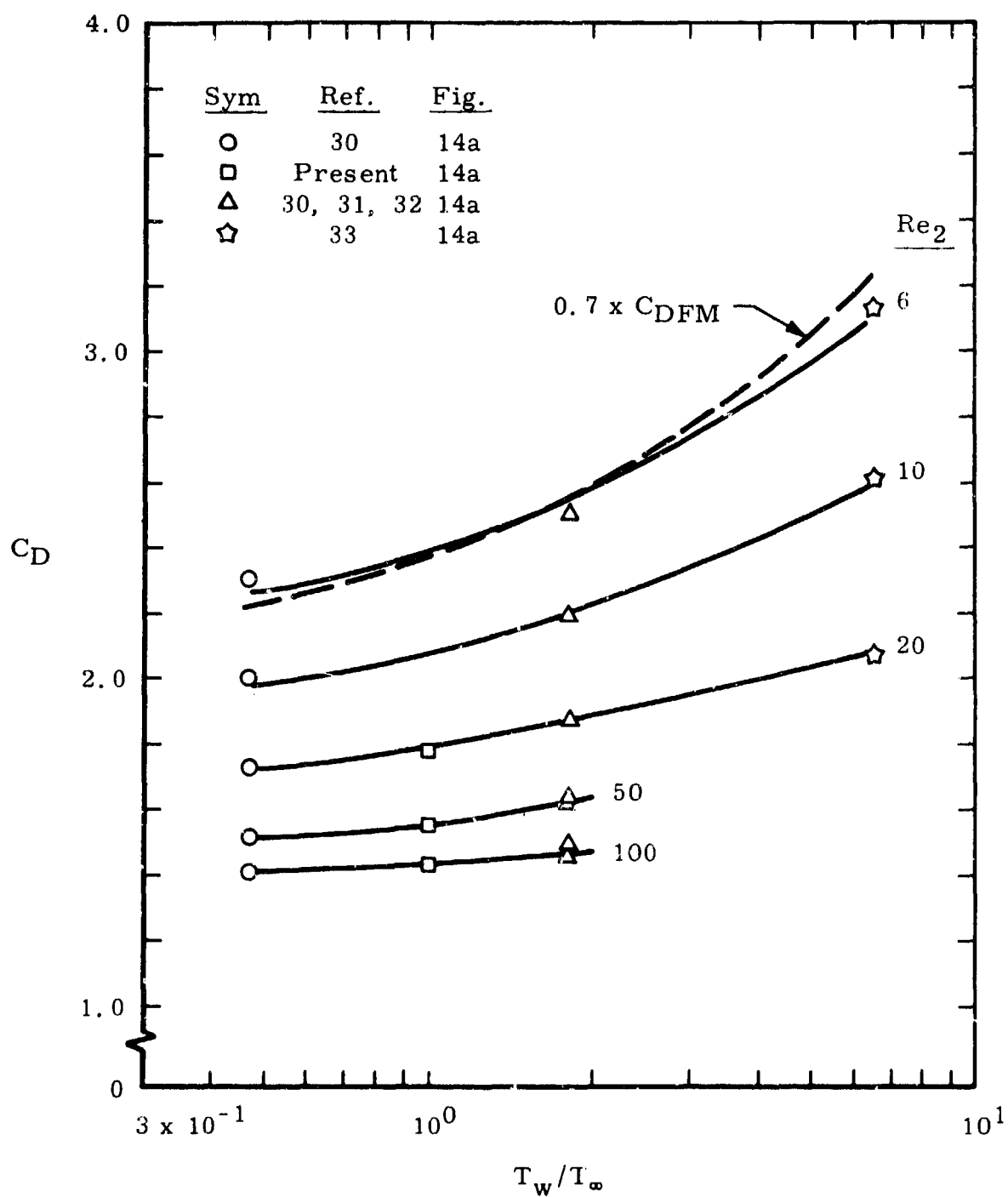
a. $M_\infty \approx 2.0$

Fig. 17 Variation of Sphere Drag Coefficient with Wall Temperature

67
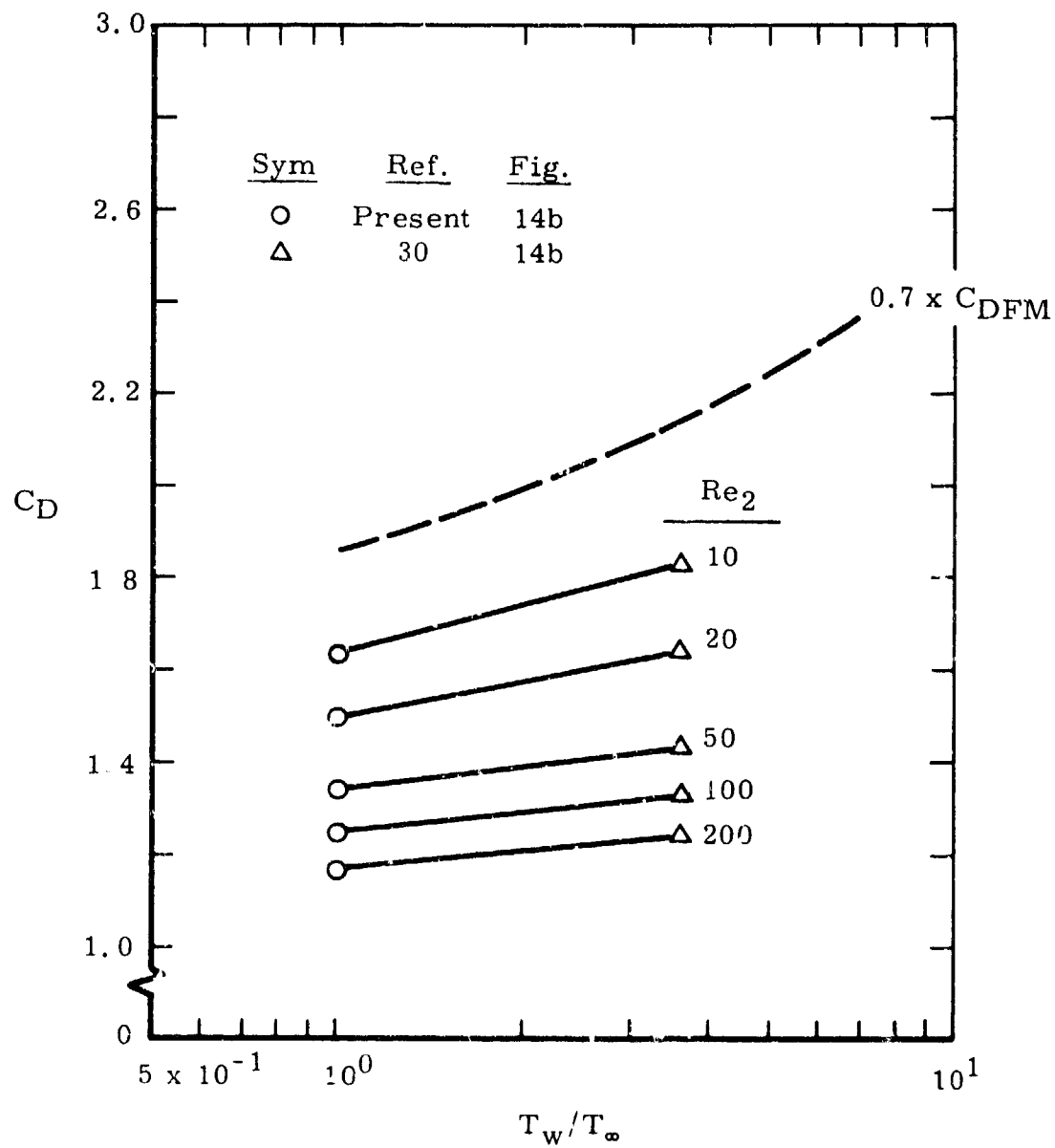
b. $M_\infty \approx 3.5$

Fig. 17 Continued

68
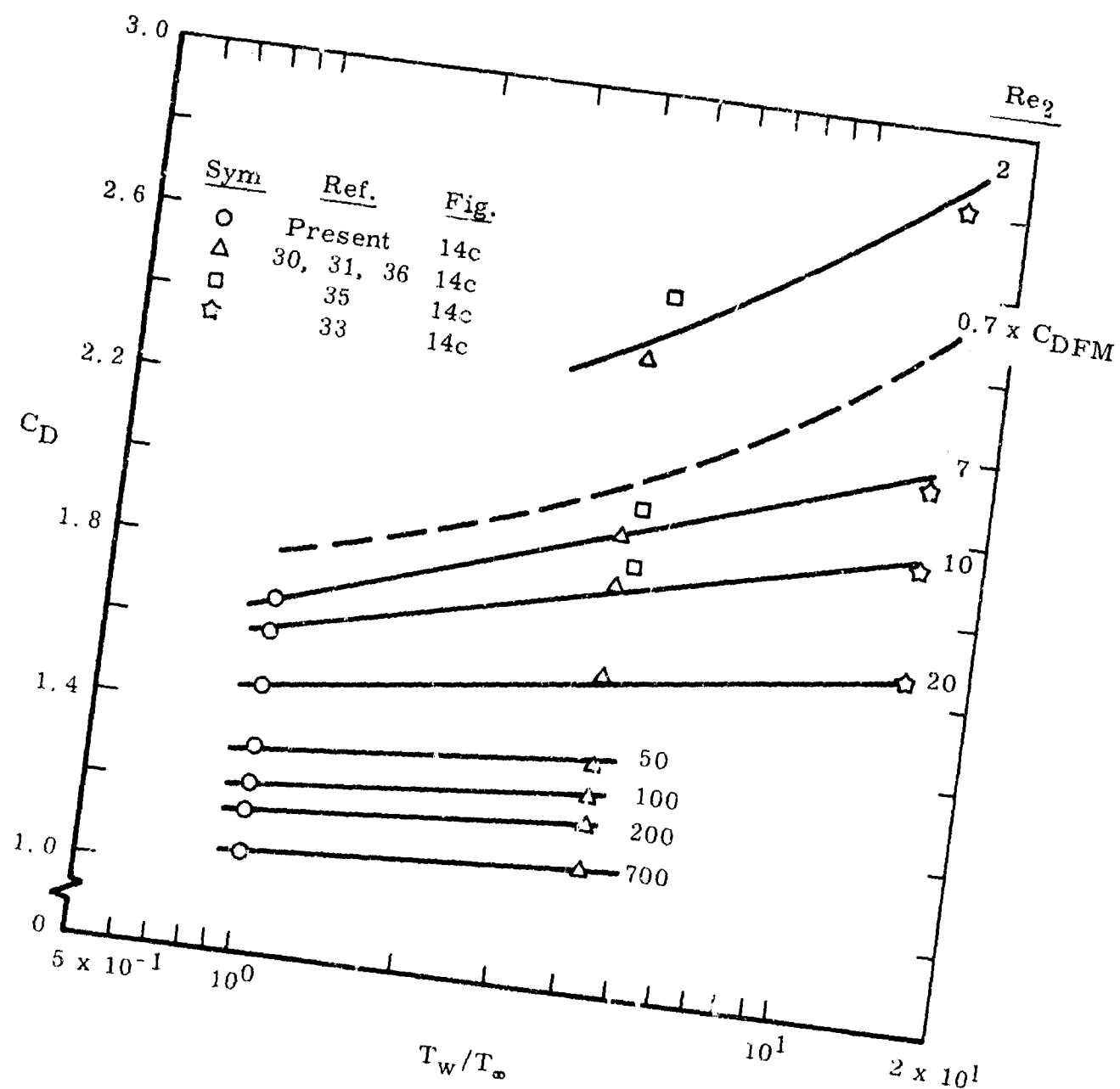
c. $M_\infty \approx 4.0$
Fig. 17 Continued

69
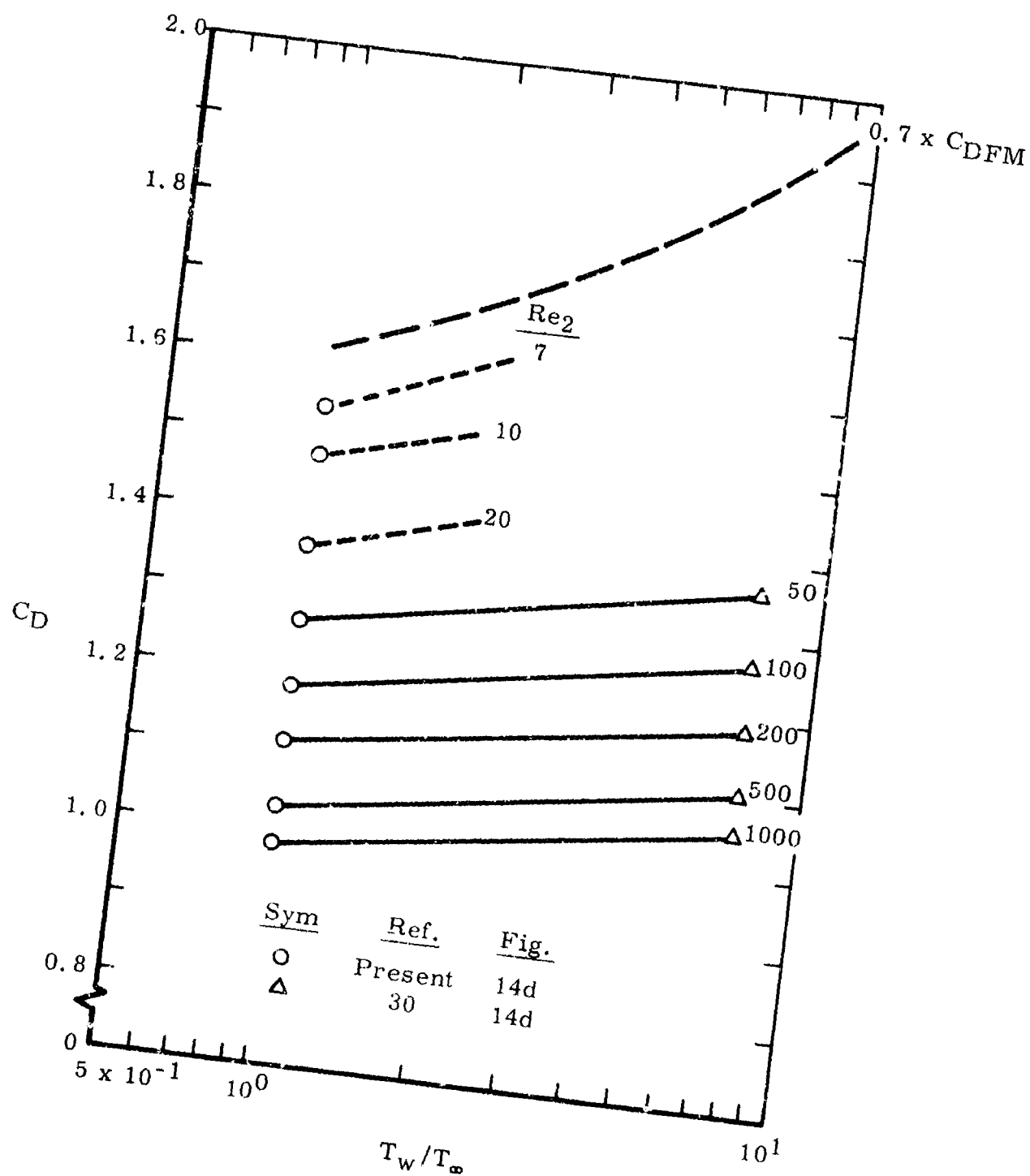
d. $M_\infty \approx 6.0$
Fig. 17 Continued
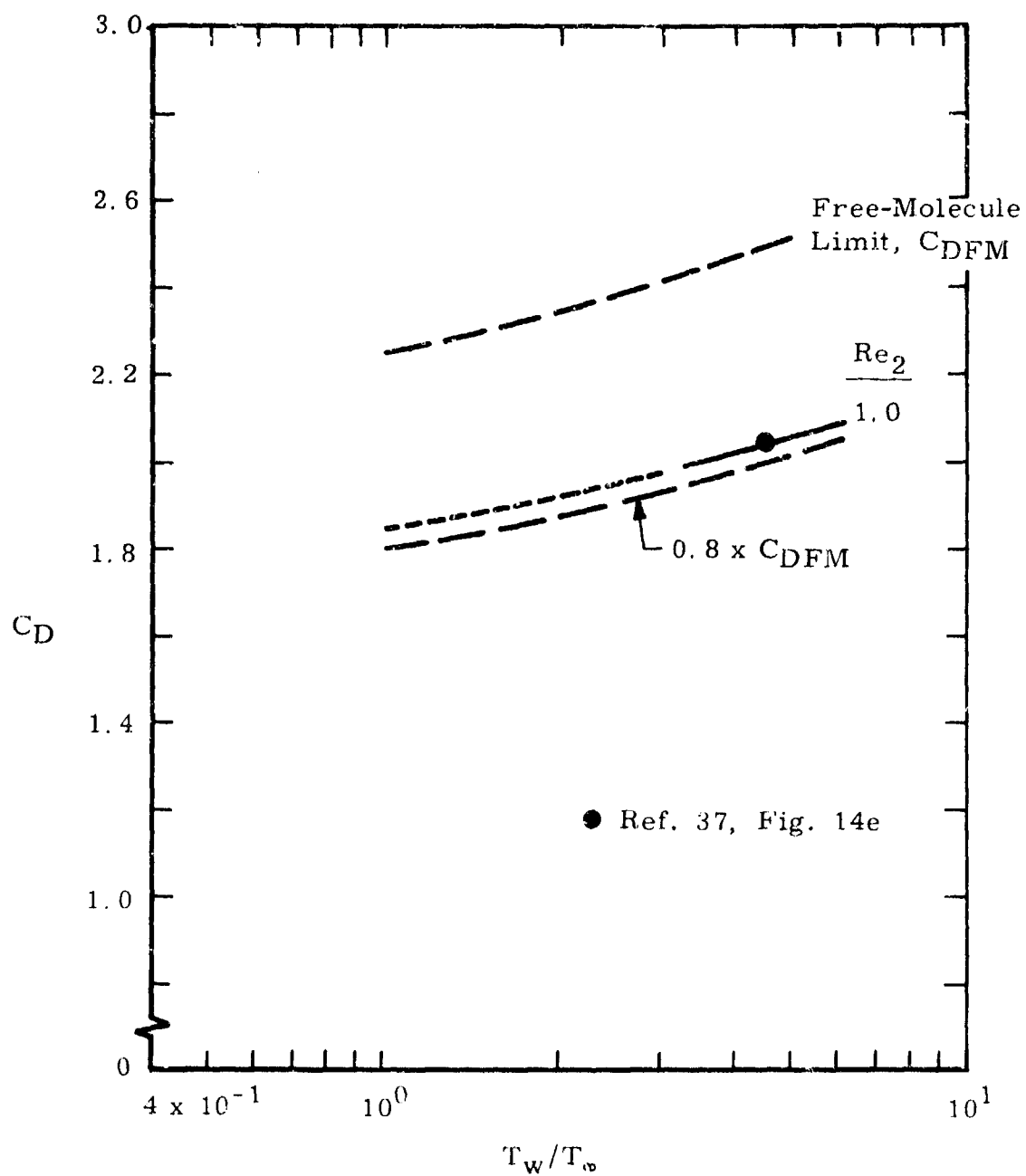
e. $M_\infty \approx 7.35$
Fig. 17 Continued

71
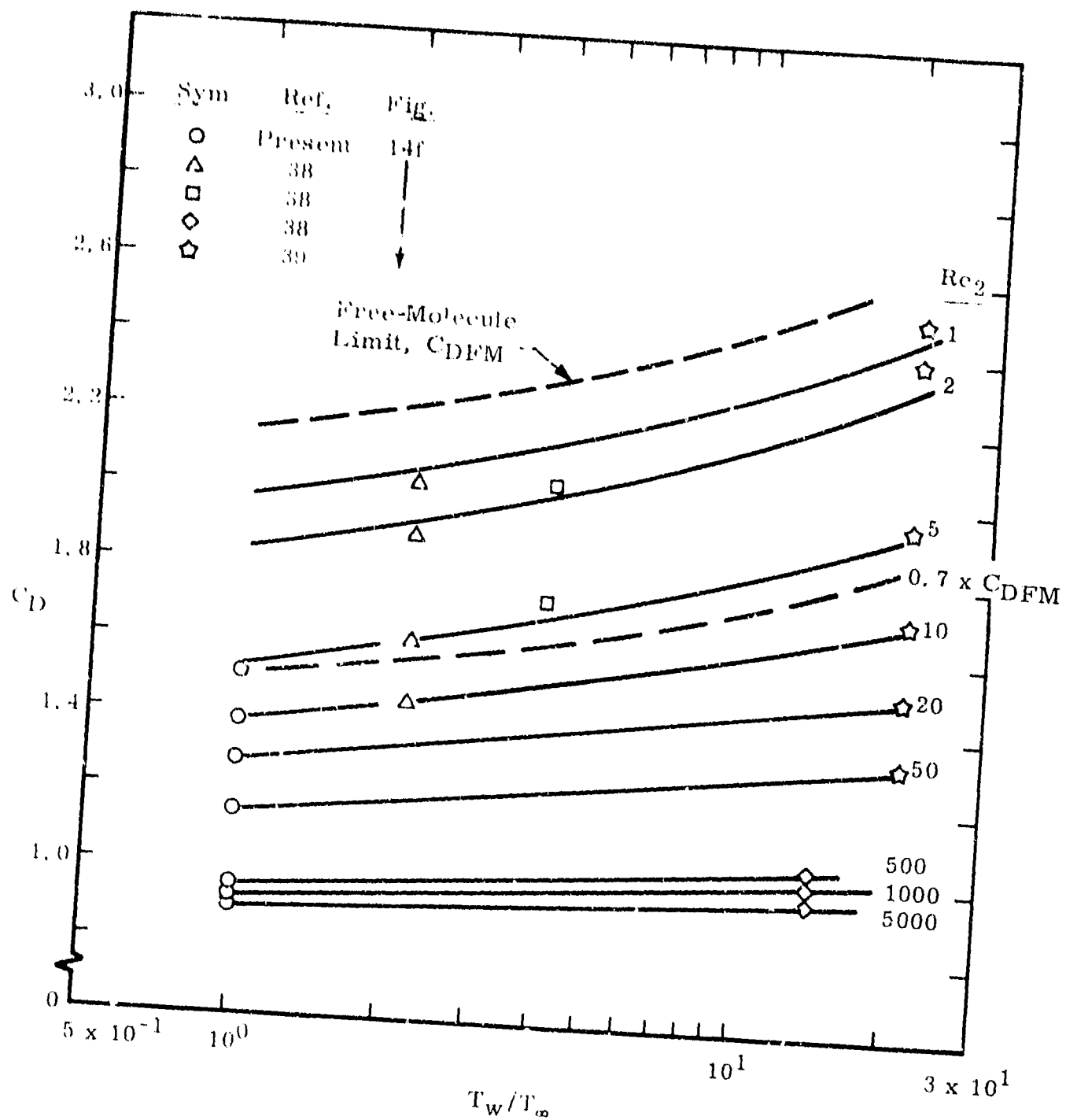
f. $M_\infty \approx 10.4$
Fig. 17 Concluded
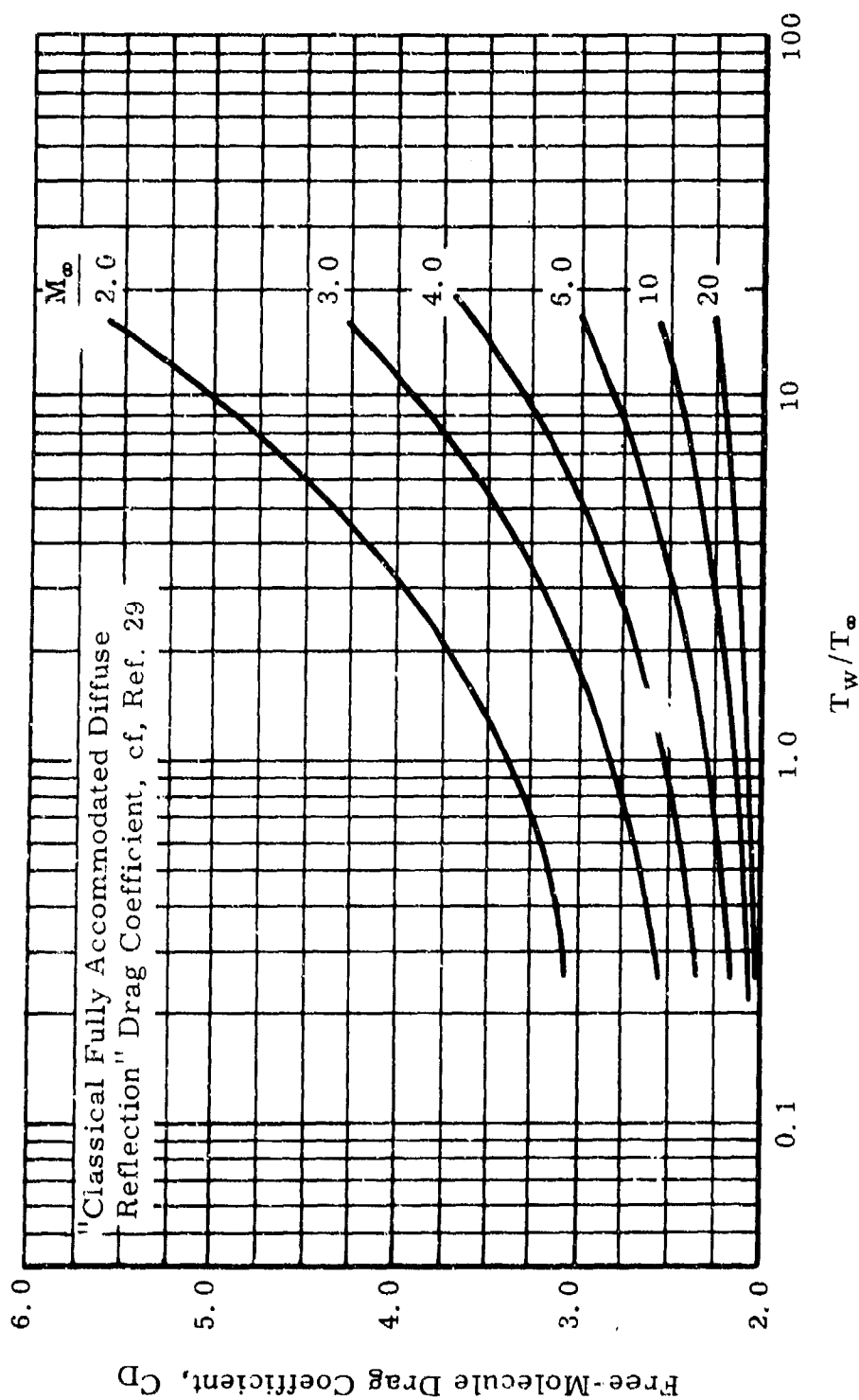
Fig. 18 Variation of Sphere Drag Coefficient with Wall Temperature and Mach Number in the Free-Molecule Flow Regime
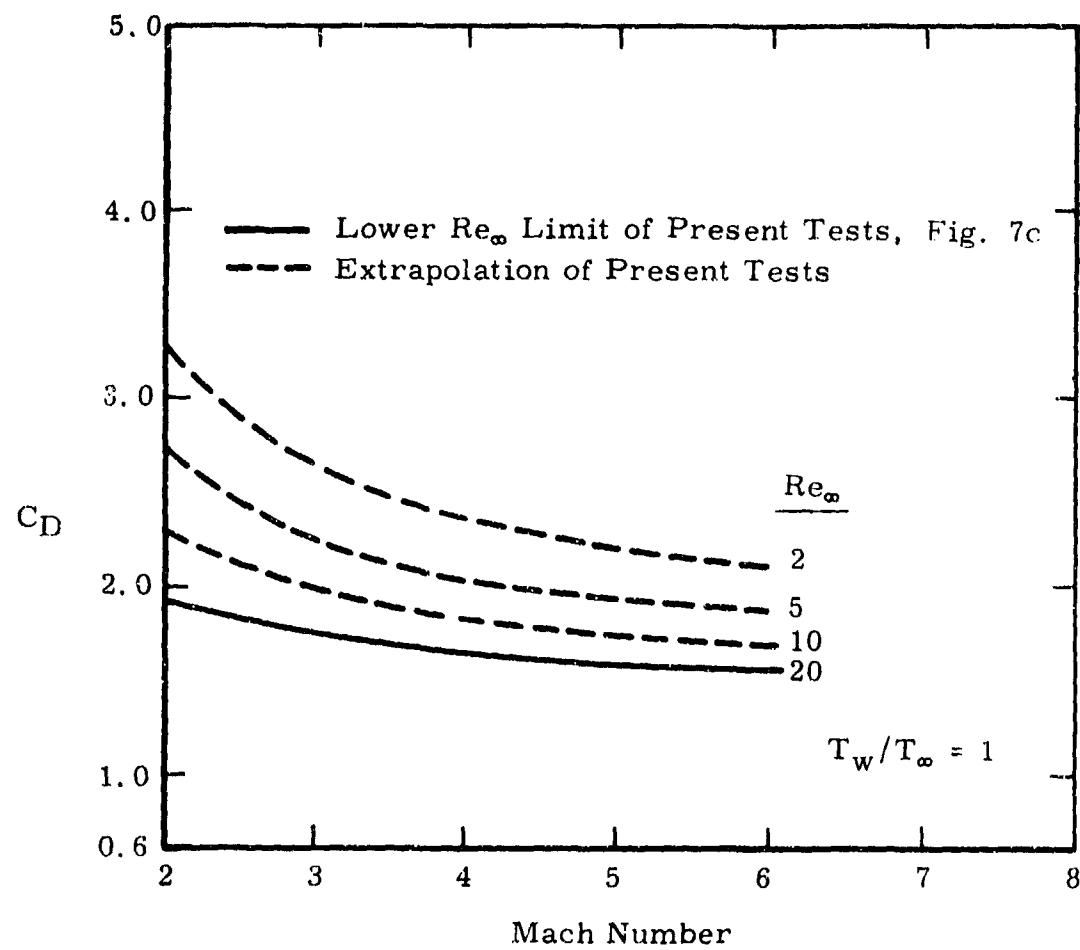
Fig. 19 Variation of Sphere Drag Coefficient with Mach Number - An Extrapolation to Re$_\infty$ = 2.0

74

TABLE I
SPHERE MATERIALS AND SIZES USED IN THE RANGE TEST

	Diameter, in.						
	3/32	1/8	1/4	3/8	7/16	1/2	1
Copper			✓	✓		✓	
Beryllium-Copper			✓				
Steel		✓	✓	✓			
Aluminum		✓	✓				
Nylon	✓	✓	✓	✓		✓	✓
Lexan®*		✓					
Dylite® **		✓	✓		✓		

*Lexan, a registered trademark of the General Electric Company, is of density slightly greater than nylon.

**Dylite, a registered trademark of Sinclair Koppers Company, is an expandable styrofoam.

TABLE II
PRESENT EXPERIMENTAL SPHERE DRAG DATA

M_∞	Re_∞	C_D
$0.12 \leq M_\infty \leq 0.18$		
0.159	16,327	0.425
0.156	15,924	0.418
0.143	14,634	0.415
0.149	2,337	0.388
0.129	2,027	0.409
0.126	4,873	0.378
0.132	5,122	0.379
0.158	2,501	0.391
0.136	20,565	0.427
0.134	20,342	0.424
0.166	12,711	0.413
0.140	10,763	0.40?
0.138	10,641	0.405
0.141	10,939	0.396
$0.19 \leq M_\infty \leq 0.27$		
0.244	48,593	0.459
0.244	48,473	0.464
0.249	49,528	0.462
0.246	48,971	0.461
0.243	47,854	0.463
0.249	19,765	0.431
0.251	19,955	0.431
0.249	19,899	0.433
0.248	19,959	0.434
0.267	2,118	0.409
0.266	2,070	0.410
0.263	2,058	0.410
0.212	4,244	0.380
0.237	4,749	0.385
0.253	5,069	0.391
0.250	5,026	0.389
0.246	9,884	0.420
0.246	9,871	0.419
0.273	10,835	0.415
0.268	10,695	0.412
0.263	10,386	0.411
0.261	10,353	0.412
0.254	10,113	0.420
0.253	10,121	0.419
0.253	10,088	0.420
0.253	10,081	0.416

M_∞	Re_∞	C_D
$0.28 \leq M_\infty \leq 0.42$		
0.283	2,230	0.410
0.284	11,224	0.416
0.393	48,561	0.474
0.390	48,365	0.473
0.392	48,631	0.472
0.392	48,687	0.474
0.405	19,767	0.445
0.404	20,239	0.448
0.404	20,414	0.446
0.403	20,065	0.445
0.417	10,277	0.429
0.415	10,247	0.431
0.423	5,307	0.412
0.419	5,270	0.408
0.399	5,038	0.405
0.409	2,015	0.424
0.411	2,043	0.421
0.408	2,058	0.420
0.423	1,060	0.480
0.409	1,024	0.482
0.340	19,826	0.438
0.350	20,335	0.441
$0.43 \leq M_\infty \leq 0.55$		
0.535	17,680	0.455
0.446	10,890	0.441
0.501	1,273	0.478
0.468	1,161	0.478
0.431	1,097	0.479
0.428	10,440	0.428
0.432	10,611	0.427
0.510	50,940	0.494
0.430	17,193	0.440
0.550	1,125	0.489

M_∞	Re_∞	C_D
$0.57 \leq M_\infty \leq 0.63$		
0.595	49,436	0.506
0.593	50,230	0.507
0.594	49,111	0.504
0.588	48,827	0.501
0.592	49,216	0.503
0.570	18,894	0.465
0.620	20,301	0.479
0.607	20,060	0.478
0.570	4,762	0.434
0.590	4,945	0.441
0.615	5,270	0.453
0.627	2,077	0.467
0.584	1,936	0.466
0.617	2,131	0.463
0.594	2,048	0.461
0.598	999	0.523
0.578	991	0.518
0.582	962	0.525
0.599	1,016	0.517
0.623	10,309	0.463
0.590	23,888	0.477
$0.70 \leq M_\infty \leq 0.7$		
0.712	2,016	0.499
0.701	1,998	0.492
0.704	1,985	0.497
0.707	1,009	0.547
0.708	1,013	0.543
0.709	1,015	0.550
0.735	4,523	0.477

TABLE II (Continued)

M_∞	Re_∞	C_D
$0.79 \le M_\infty \le 0.83$		
0.826	2049	0.554
0.826	3041	0.557
0.833	2953	0.561
0.809	988	0.610
0.916	1019	0.623
0.794	1004	0.602
0.736	4890	0.504
0.805	5022	0.514
0.820	162	1.026
$0.88 \le M_\infty \le 0.95$		
0.918	2038	0.637
0.917	2036	0.643
0.925	2051	0.649
0.936	1047	0.723
0.919	1024	0.708
0.928	1035	0.711
0.900	998	0.712
0.895	993	0.707
0.900	997	0.716
0.879	4849	0.559
0.911	5063	0.591
0.923	471	0.821
0.952	487	0.874
0.918	465	0.824
0.951	474	0.884
0.918	184	1.006
0.927	82.4	1.518
0.882	4888	0.555
0.894	4952	0.554
0.950	1899	0.673
$0.96 \le M_\infty \le 0.97$		
0.967	2041	0.733
0.963	1050	0.735
0.968	1034	0.850
0.957	4925	0.643
0.955	468	0.886
0.860	476	0.915
0.973	201	1.050
0.973	194	1.041
0.967	191	1.068
0.959	191	1.093

M_∞	Re_∞	C_D
$0.98 \le M_\infty \le 0.998$		
0.998	1074	0.935
0.985	1966	0.812
0.983	5042	0.697
0.992	488	0.993
0.993	198	1.265
0.989	196	1.294
0.986	197	1.144
0.997	506	1.034
$1.003 \le M_\infty \le 1.07$		
1.017	2006	0.863
1.030	2076	0.858
1.019	2060	0.859
1.013	1103	0.865
1.028	1022	0.925
1.055	1055	0.912
1.028	1088	0.949
1.014	1006	0.950
1.003	998	0.962
1.023	5097	0.7
1.012	5035	0.752
1.045	4746	0.760
1.058	527	1.001
1.038	206	1.252
1.072	47.7	1.964
1.037	92.1	1.650
1.043	92.8	1.640
1.004	5043	0.751
1.067	4842	0.770

M_∞	Re_∞	C_D
$1.08 \le M_\infty \le 1.19$		
1.103	1843	0.898
1.100	917	0.924
1.136	1061	0.994
1.087	1954	0.893
1.148	5194	0.827
1.130	5117	0.817
1.139	5179	0.832
1.187	927	0.914
1.132	463	1.062
1.177	478	1.071
1.113	222	1.302
1.108	199	1.289
1.105	550	1.042
1.077	488	1.034
1.116	507	1.059
1.165	47.7	1.907
1.145	46.9	1.908
1.181	97.8	1.628
1.164	95.7	1.623
1.094	48.8	1.916
1.104	98.5	1.613
1.106	5027	0.796
1.140	5101	0.937
1.164	18.6	2.381
$1.2 \le M_\infty \le 1.3$		
1.197	1985	0.948
1.256	2086	0.961
1.195	1988	0.939
1.214	5070	0.872
1.208	5019	0.863
1.211	504	1.109
1.209	199	1.344
1.213	203	1.331
1.219	200	1.336
1.294	183	1.376
1.300	479	1.162
1.250	1676	0.896
1.289	42.2	1.823
1.275	95.7	1.635
1.195	19.4	2.303

TABLE II (Continued)

M_∞	Re_∞	C_D
1.3 ≤ M_∞ ≤ 1.45		
1.356	1929	0.997
1.394	1990	0.995
1.358	1958	0.992
1.398	4667	0.930
1.341	47	1.158
1.357	485	1.151
1.402	202	1.345
1.431	201	1.326
1.360	4535	0.939
1.384	1851	1.017
1.383	187	1.427
1.304	42.8	1.850
1.442	47.6	1.627
1.388	186	1.442
1.371	48.1	1.798
1.530	46.6	1.787
1.449	102	1.555
1.440	101	1.631
1.380	51.9	1.831
1.326	50.1	1.809
1.334	50.5	1.868
1.396	98.0	1.650
1.322	54.7	1.842
1.365	35.8	2.063
1.383	18.2	2.241
1.335	10.6	2.591
1.376	22.3	2.166
1.383	22.3	2.127

M_∞	Re_∞	C_D
1.45 ≤ M_∞ ≤ 1.65		
1.494	1,362	1.041
1.572	1,955	1.016
1.576	1,948	1.011
1.590	1,989	1.006
1.506	1,644	1.025
1.527	5,056	0.947
1.521	5,089	0.939
1.548	478	1.210
1.529	472	1.202
1.636	200	1.367
1.586	194	1.346
1.604	198	1.320
1.479	9,894	0.910
1.513	10,091	0.917
1.486	493	1.218
1.477	98.5	1.633
1.621	107	1.582
1.573	103	1.590
1.509	98.4	1.588
1.517	49.5	1.790
1.631	94.2	1.586
1.594	97.4	1.539
1.569	95.7	1.529
1.568	52.1	1.806
1.553	38.6	1.860
1.513	20.0	2.157
1.545	21.8	2.019
1.598	25.5	2.007
1.630	26.3	1.975
1.474	24.2	2.067
1.539	7,755	0.945
1.582	77,380	0.934

M_∞	Re_∞	C_D
1.65 ≤ M_∞ ≤ 1.85		
1.654	1,404	1.070
1.682	1,703	1.018
1.792	1,944	1.017
1.756	1,962	1.007
1.747	1,754	1.050
1.835	1,847	1.041
1.780	4,590	0.961
1.814	5,060	0.952
1.802	5,030	0.966
1.657	516	1.197
1.723	472	1.225
1.810	498	1.217
1.737	470	1.223
1.851	4,554	0.996
1.722	656	1.131
1.693	11,279	0.937
1.656	1,096	1.090
1.675	224	1.385
1.658	95.6	1.538
1.814	18.7	2.051
1.850	24.6	1.920
1.800	50.8	1.705
1.763	49.7	1.735

78

TABLE II (Continued)

M_∞	Re_∞	C_D
$1.9 \leq M_\infty \leq 2.2$		
2.128	516	1.223
2.146	524	1.197
1.990	4,947	0.993
1.947	1,925	1.056
2.052	2,047	1.043
2.171	1,089	1.104
2.076	205	1.369
2.100	526	1.252
2.150	1,081	1.124
1.972	961	1.130
2.111	1,042	1.124
2.052	512	1.245
2.128	104	1.484
2.067	104	1.440
2.109	214	1.371
2.105	105	1.462
2.031	1,347	1.098
2.052	204	1.380
2.137	529	1.232
2.177	216	1.332
2.204	110	1.467
2.013	49.7	1.583
2.035	50.3	1.611
2.114	42.0	1.687
2.190	21.6	1.884
1.940	21.9	1.919
2.053	27.1	1.825
1.896	30.2	1.797
1.341	4.88	2.185
2.010	3,441	1.022
$2.4 \leq M_\infty \leq 2.7$		
2.514	201	1.313
2.539	8,429	0.971
2.460	1,236	1.086
2.408	16,011	0.955
2.528	1,001	1.139
2.584	506	1.197
2.649	1,059	1.125
2.543	504	1.226
2.419	192	1.357
2.447	197	1.353
2.535	99.9	1.396
2.743	46.2	1.574
2.704	54.2	1.549
2.659	21.0	1.819
2.477	19.3	1.860
2.604	52.3	1.557
2.541	51.0	1.570
2.649	20.9	1.820

M_∞	Re_∞	C_D
$2.8 \leq M_\infty \leq 3.2$		
2.924	4,833	1.008
2.871	4,767	1.005
2.989	1,964	1.045
2.940	1,938	1.045
3.063	507	1.195
3.072	506	1.192
3.042	509	1.189
3.044	509	1.179
2.999	992	1.129
2.991	989	1.125
2.991	196	1.308
3.090	202	1.300
3.086	201	1.346
2.859	189	1.356
2.998	994	1.126
2.970	197	1.192
2.888	4,812	1.012
2.907	961	1.135
3.171	21,104	0.944
2.817	186	1.332
3.155	207	1.282
2.929	197	1.298
3.062	99.8	1.431
2.764	91.8	1.445
3.135	51.7	1.490
2.912	55.3	1.423
3.030	50.0	1.536
2.944	19.8	1.825
2.895	47.6	1.597
3.141	21.4	1.708
2.986	50.4	1.482
3.063	50.8	1.500
3.074	20.5	1.673
2.940	19.0	1.795
3.036	20.0	1.760
2.945	19.8	1.696

M_∞	Re_∞	C_D
$3.8 \leq M_\infty \leq 4.2$		
3.926	4,845	0.966
4.135	10,255	0.945
4.017	4,964	0.967
4.176	2,069	1.038
3.808	1,908	1.040
4.004	1,978	1.030
3.956	978	1.091
4.030	1,006	1.064
3.892	4,897	0.987
4.243	522	1.110
3.958	487	1.146
4.104	202	1.269
4.081	16.2	1.573
3.867	488	1.143
4.099	509	1.150
4.062	50.0	1.473
4.063	20.4	1.657
3.978	19.5	1.516
3.993	50.5	1.407
4.006	50.0	1.407
4.070	20.7	1.574
4.085	20.8	1.538
4.060	201	1.246
3.091	103	1.327
3.924	97.2	1.320
3.960	49.8	1.486
4.250	105	1.331
4.153	50.2	1.485

TABLE II (Concluded)

M_∞	Re_∞	C_D
$4.8 \leq M_\infty \leq 5.2$		
4.822	4784	0.973
4.781	9453	0.955
4.849	9592	0.944
5.023	4991	0.948
5.193	2057	1.015
5.193	2057	1.032
5.206	2062	1.037
5.235	1040	1.057
5.071	671	1.072
5.097	1004	1.084
4.835	81.1	1.377
5.100	1013	1.062
4.984	655	1.127
5.075	195	1.196
5.073	493	1.152
5.044	498	1.146
5.014	97.9	1.280
5.139	508	1.148
5.126	507	1.144
5.091	202	1.196
5.062	491	1.154
5.135	21.1	1.575
4.999	20.4	1.606
4.904	50.2	1.431
5.110	52.3	1.473
4.956	196	1.264
5.055	2016	1.039
4.984	996	1.077
5.056	51.0	1.494
5.047	20.0	1.623
5.023	19.0	1.686
4.918	9874	0.951
5.082	5076	0.973
4.966	97.5	1.333
4.946	49.9	1.407
5.096	20.5	1.544
5.038	99.0	1.377
4.957	96.2	1.401
4.919	4907	0.975
5.127	2547	1.004

M_∞	Re_∞	C_D
$5.8 \leq M_\infty \leq 6.2$		
5.929	9934	0.940
5.782	1987	1.025
5.800	9552	0.948
5.784	9290	0.947
5.836	4871	0.950
6.028	4971	0.936
5.881	5036	0.945
5.790	1898	1.010
6.203	2049	1.015
6.217	2054	1.014
6.247	511	1.141
5.859	477	1.154
5.914	486	1.165
5.969	260	1.266
5.963	999	1.063
5.966	999	1.063
5.967	261	1.168
5.969	194	1.244
5.944	484	1.153
5.915	194	1.252
5.911	194	1.217
5.899	484	1.162
5.895	483	1.147
5.915	194	1.228
5.763	49.5	1.464
5.803	48.0	1.490
5.900	49.0	1.409
5.764	47.0	1.390
5.884	24.0	1.472
6.110	103	1.289
5.816	19.4	1.568
5.853	97.3	1.277
5.909	4901	0.961

M_∞	Re_∞	C_D
Odd M_∞		
0.648	22,041	0.489
0.691	5,736	0.477
0.874	4,841	0.542
1.860	1,865	1.053
1.892	4,670	0.992
1.871	15.3	1.992
2.254	22.8	1.869
1.890	286	0.988
1.884	109	1.502
1.877	25.9	1.890
1.862	24.8	1.797
2.394	47.3	1.538
4.421	10,965	0.942
4.271	10,538	0.947
4.261	1,055	1.056
4.481	8,839	0.964
4.254	524	1.114
4.388	110	1.356
5.599	9,153	0.944
5.723	1,862	1.025
5.592	182	1.252
5.597	183	1.267
6.338	1,041	1.040
6.385	1,072	1.036
6.774	194	1.150
6.832	96.7	1.165
6.955	494	1.126

APPENDIX III
DEVELOPMENT OF SHOCK PATTERNS AT TRANSONIC SPEEDS

The following schlieren photographs are included in this report as an item of general interest. These pictures show the development of bow and wake shock patterns for a 0.25-in.-diam nylon sphere traveling at speeds near $M_\infty = 1$. For these conditions, $1050 < Re_\infty < 1250$.

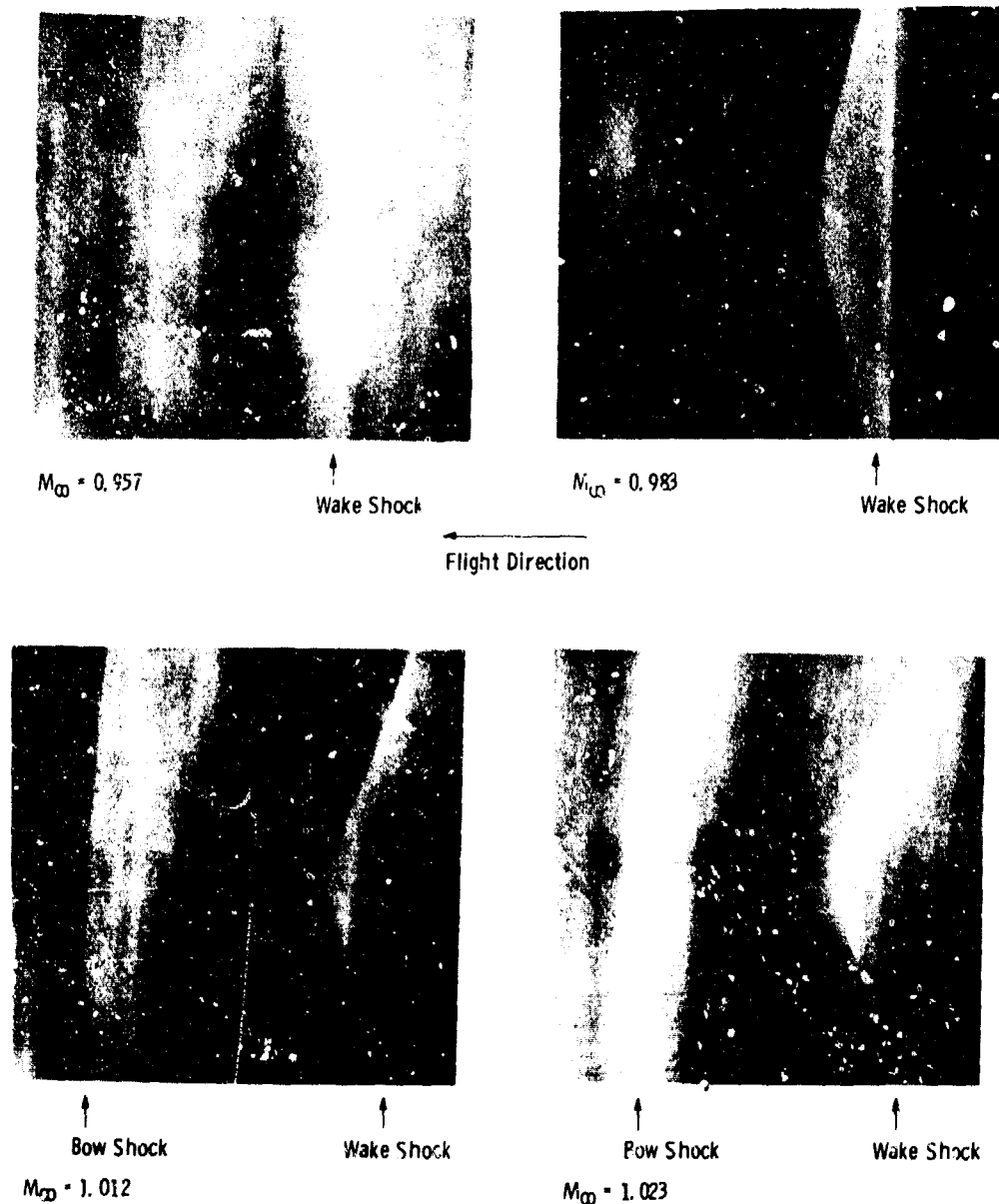$M_\infty = 0.957$ ↑ Wake Shock $M_\infty = 0.983$ ↑ Wake Shock

← Flight Direction

↑ Bow Shock   ↑ Wake Shock   ↑ Bow Shock   ↑ Wake Shock

$M_\infty = 1.012$ $M_\infty = 1.023$

Fig. III-1 Development of Shock Patterns at Transonic Speeds

81

| Bow Shock | Wake Shock | | Bow Shock | Wake Shock |

$M_\infty = 1.045$ $M_\infty = 1.130$
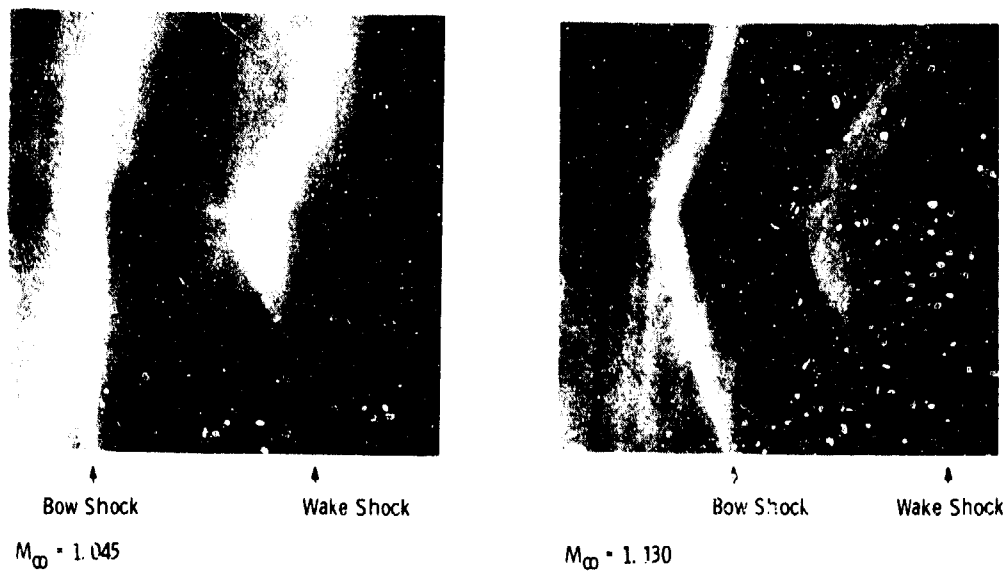
Fig. IIi-1 Concluded
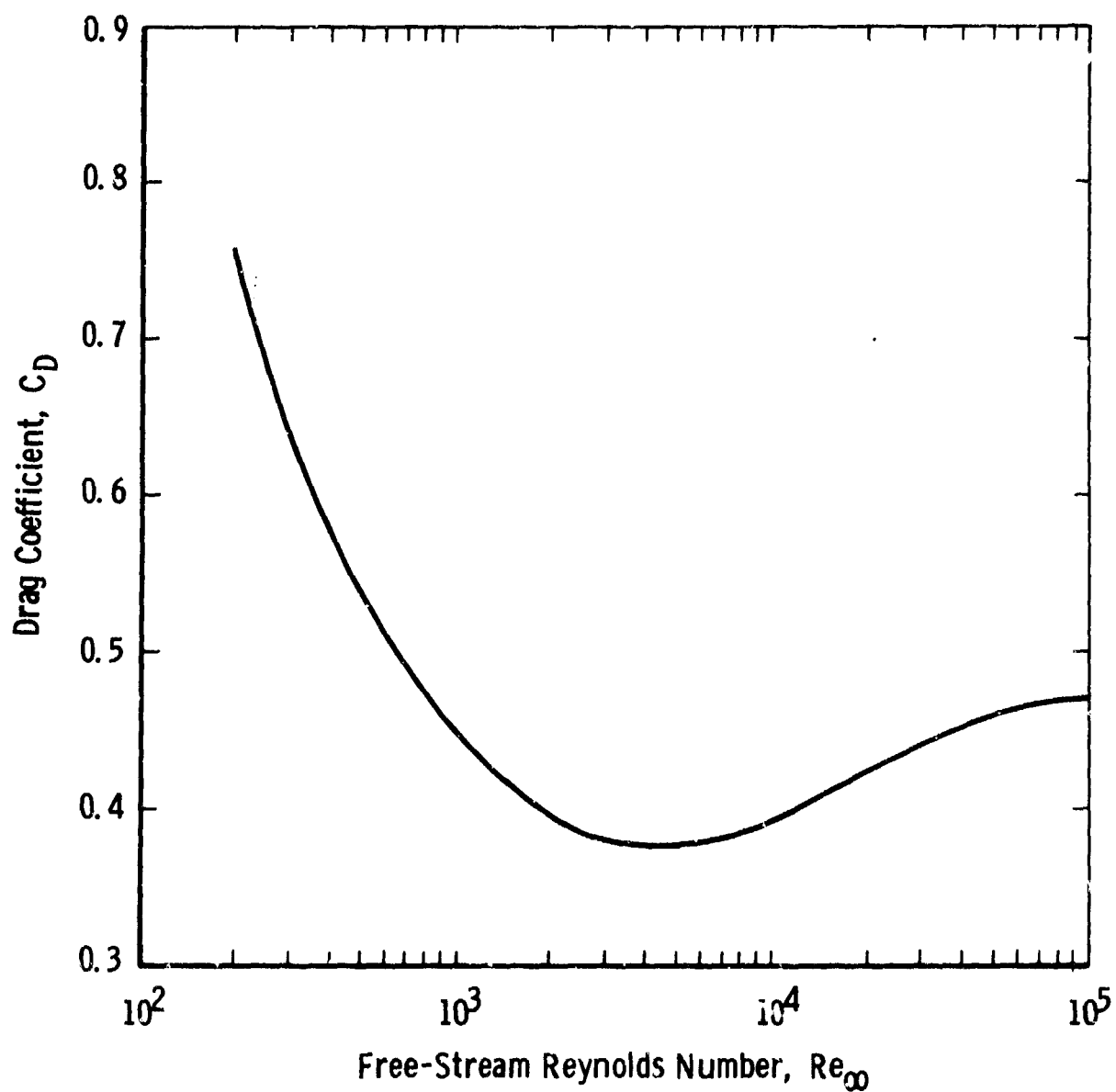
Fig. IV-1 Extrapolation of Ballistic Range Data from $M_\infty = 0.15$
to $M_\infty = 0$

83

DOCUMENT CONTROL DATA · R & D

(Security classification of title, body of abstract and indexing annotation must be entered when the overall report is classified)

1. ORIGINATING ACTIVITY *(Corporate author)*	2a. REPORT SECURITY CLASSIFICATION
Arnold Engineering Development Center ARO, Inc., Operating Contractor Arnold Air Force Station, Tennessee 37389	UNCLASSIFIED
	2b. GROUP N/A

3. REPORT TITLE

FREE-FLIGHT MEASUREMENTS OF SPHERE DRAG AT SUBSONIC, TRANSONIC, SUPERSONIC, AND HYPERSONIC SPEEDS FOR CON'T'NUUM, TRANSITION, AND NEAR-FREE-MOLECULAR FLOW CONDITIONS

4. DESCRIPTIVE NOTES *(Type of report and inclusive dates)*
Final Report, November 13, 1969, through June 19, 1970

5. AUTHOR(S) *(First name, middle initial, last name)*

A. B. Bailey and J. Hiatt, ARO. Inc.

6. REPORT DATE	7a. TOTAL NO. OF PAGES	7b. NO. OF REFS
March 1971	90	41

8a. CONTRACT OR GRANT NO.	9a. ORIGINATOR'S REPORT NUMBER(S)
F40600-71-C-0002	
b. PROJECT NO. 6682	AEDC-TR-70-291
c. Program Element 65701F	9b. OTHER REPORT NO(S) *(Any other numbers that may be assigned this report)*
d.	ARO-VKF-TR-70-281

10. DISTRIBUTION STATEMENT
This document has been approved for public release and sale; its distribution is unlimited.

11. SUPPLEMENTARY NOTES	12. SPONSORING MILITARY ACTIVITY
Available in DDC.	Air Force Cambridge Research Laboratories (CRER), L. G. Hanscom Field, Bedford, Massachusetts 01730

13. ABSTRACT

A comprehensive set of measurements has been made in a ballistic range which permits the sphere drag coefficient to be derived with an uncertainty of approximately ± 2 percent in the flight regime $0.1 < M_\infty < 6.0$ and $2 \times 10^1 < Re_\infty < 10^5$ for $T_W/T_\infty \approx 1.0$. Sufficient information is also presented to predict the effect of wall temperature on sphere drag coefficient when $T_W/T_\infty \neq 1.0$ for $2 < M_\infty < 6$. This investigation represents the most comprehensive experimental program to date to define sphere drag in the velocity-altitude regime applicable to the falling sphere technique for defining upper air density.

DD FORM 1 NOV 65 1473

14. KEY WORDS	LINK A		LINK B		LINK C	
	ROLE	WT	ROLE	WT	ROLE	WT
atmospheric density						
rarefied gas dynamics						
spheres						
drag						
transonic flow						
hypersonic flow						
ballistic ranges						

AFSC
Arnold AFS Tenn